ISBN 978-82-326-3328-9 (printed ver.)
ISBN 978-82-326-3329-6 (electronic ver.)
ISSN 1503-8181

NTNU
Norwegian University of
Science and Technology

Shengwen Tu

Doctoral thesis

Doctoral theses at NTNU, 2018:269

NTNU
Norwegian University of Science and Technology
Thesis for the Degree of
Philosophiae Doctor
Faculty of Engineering
Department of Structural Engineering

NTNU

Doctoral theses at NTNU, 2018:269

Shengwen Tu

Determining the tensile properties of Arctic materials and modelling their effects on fracture

NTNU
Norwegian University of
Science and Technology

Shengwen Tu

Determining the tensile properties of Arctic materials and modelling their effects on fracture

Thesis for the Degree of Philosophiae Doctor

Trondheim, September 2018

Norwegian University of Science and Technology
Faculty of Engineering
Department of Structural Engineering

NTNU
Norwegian University of
Science and Technology

NTNU
Norwegian University of Science and Technology

Thesis for the Degree of Philosophiae Doctor

Faculty of Engineering
Department of Structural Engineering

ISBN 978-82-326-3328-9 (printed ver.)
ISBN 978-82-326-3329-6 (electronic ver.)
ISSN 1503-8181

Doctoral theses at NTNU, 2018:269

Printed by NTNU Grafisk senter

Preface

This dissertation is submitted to the Norwegian University of Science and Technology (NTNU) for partial fulfillment of the degree of philosophiae doctor.

The thesis comprises an introductory section, and 5 papers (three published and two submitted).

The work presented herein was performed in the period between August 2015 and September 2018 at the Department of Structural Engineering in Trondheim, under the supervision of *Prof.* Zhiliang Zhang, Dr. Xiaobo Ren and *Prof.* Jianying He. The numerical work was carried out at Nanomechanical Lab, Department of Structural Engineering (KT), Faculty of Engineering (IV), Norwegian University of Science and Technology(NTNU), Trondheim, Norway. The experimental work was mainly conducted by Engineer Tore Andre Kristensen at the Materials testing Lab in SINTEF, Trondheim.

The thesis was funded by the Chinese Scholarship Council and the research council of Norway through the Petromaks 2 Programme, contract no.228513/E30.

Abstract

The fracture behavior of metallic materials at low temperatures arise great attention among the petroleum industries, due to the potential considerable amount of petroleum and gas resources to be found there. Deep understanding of the mechanical behavior of steels at low temperatures will facilitate and provide solutions for safe and cost-effective application of materials for hydrocarbon exploration and production in arctic regions. In this thesis the low temperature effect on mechanical behavior of steels in several aspects has been studied and the results from five papers are presented.

The equivalent stress-strain curve is crucial for the structural integrity assessment with finite element method. Conventional methods for measuring equivalent stress-strain curves documented in testing codes are only suitable for homogeneous materials. Furthermore, the stress-strain curve derived with those methods need to be corrected after diffuse necking. In this thesis two methods have been developed to determine equivalent stress-strain curves of metallic materials. By introducing an axisymmetric notch on the smooth round bar specimen, the deformation is constrained in the notch region during the loading process. By performing the numerical study of true stress-strain curve from notched specimens, a corresponding procedure has been proposed to convert the true stress-strain curve from any notched specimens to material's equivalent stress-strain. Meanwhile, we identified a 'magic' notch geometry, with a single correction factor true stress-strain curve from this 'magic' notched specimen can be corrected back to material's equivalent stress-strain curve. These two methods can be applied to inhomogeneous materials by locating the notch in the target material zone, once the geometry requirements are fulfilled.

It is well understood that the fracture ductility of metallic materials depends on the stress state which constructs the ductility diagram (ductility vs. stress triaxiality). Most of the reported studies investigate the ductility diagram at room temperature. The low temperature effect on the evolution of ductility diagram is still missing. In this thesis we performed a series of tensile tests (45 tests in total) with axisymmetric notched and smooth round bar specimens with testing temperatures down to $-60\,^{\circ}\mathrm{C}$. The specimens were machined from a 420 MPa structural steel. A newly developed edge tracing method was used to monitor the specimen deformation and to evaluate the fracture ductility. It has been found that for this 420 MPa structural steel, the strength and strain hardening characterized by the strain at the maximum load increase with the decrease of testing temperature down to $-60\,^{\circ}\mathrm{C}$. While, the low temperature effect on the ductility diagram is insignificant.

For metallic materials presenting Lüders plateau in tensile test, the plateau length increases with the decrease of testing temperature. In the state of the art design codes, knowledge about the effect of Lüders plateau on the fracture behavior of metallic material is very limited. In this thesis, the effect of Lüders plateau on ductile crack growth has been investigated with Gurson damage model and single edge notched tensile (SENT) specimens. It has been found that the existence of Lüders plateau does not influence the initiation toughness but alters material's ductile fracture resistance. The Lüders plateau effect on ductile crack resistance curve depends on the crack depth. It has been found that the Lüders plateau effect is controlled by the stress triaxiality ahead of the crack tip. For materials with smaller initial void volume fraction, the Lüders plateau effect was also observed and was more pronounced. In addition, for materials exhibiting Lüders plateau, both the effects of crack depth and strain hardening on crack resistance curve were reduced. The longer the Lüders plateau, the larger reduction.

Acknowledgement

It is not easy to arrive at this point. When I look back to the past years, I strongly feel that I am so fortunate to meet all of you: family, teachers, friends, classmates, colleagues ....

I am so fortunate to have met *Prof.* Zhiliang Zhang, my respected supervisor. Without his guidance, encouragement and help, it would be impossible for me to finish my PhD study in Norway so smoothly. Without his suggestions, it would be impossible for me to attend so many international academic activities. Without his help, it would be impossible for me to experience life outside of China for such a long time. At present any words can not express my gratitude to him for his invaluable help in the past three years. I am so fortunate to have met *Prof.* Jianying He and Dr. Xiaobo Ren. The advice from them accelerated my PhD work. Thanks so much.

I am so fortunate to have met *Prof.* Jian Shuai and my respected teacher Kui Xu. The knowledge and experience I gained from them will benefit me for life. Thanks from the bottom of my heart.

I am so fortunate to have met Dr. Egil Fagerholt and Tore Andre Kristensen. Without them, the experimental work in my PhD study would not be performed so smoothly. I am so fortunate to have met the administration staff in the Department of Structural engineering (NTNU). They are always enthusiastic to provide advice and solutions when I am in trouble. I am so fortunate to have met all the friends, classmates and colleagues during the past years. Without you life would not be so wonderful. Thanks for your accompany, competition and encouragement. Wish all of you all the best. Fishing trips in Norway will also last forever in my memory. I am so fortunate to have met all the members in Nanomechanical lab (NTNU). Thanks for creating such a harmony working group.

At the end, I would like to appreciate my family for their understanding, support and endless love.

List of Papers

The thesis is organized based on the following papers, which have been published or submitted by the candidate:

1. Shengwen Tu; Xiaobo Ren; Bård Nyhus; Odd Magne Akselsen; Jianying He; Zhiliang Zhang. A special notched tensile specimen to determine the flow stress-strain curve of hardening materials without applying the Bridgman correction. *Engineering Fracture Mechanics. 179 (2017), 225-239.*

   Zhiliang provided the idea to identify the 'magic' notch. I performed the numerical analyses and formulated the manuscript. All the authors contributed to the revision and discussion of the paper.

2. Shengwen Tu; Xiaobo Ren; Jianying He; Zhiliang Zhang. A method for determining material's equivalent stress-strain curve with any axisymmetric notched tensile specimens without Bridgman correction. *International Journal of Mechanical Sciences. 135 (2018), 656-667.*

   I was inspired by the studies of inverse method and normalization method. I did the numerical work and formulated the method. I wrote the draft. All the authors contributed to the revision and discussion of the paper.

3. Shengwen Tu; Xiaobo Ren; Jianying He; Zhiliang Zhang. Experimental measurement of temperature-dependent equivalent stress-strain curve of a 420 MPa structural steel with axisymmetric notched tensile specimens. *submitted.*

   After the method in paper II has been proposed. We arranged experimental tests to verify this method. I did the numerical work and wrote the draft. All the authors contributed to the revision and discussion of the paper.

4. Shengwen Tu; Xiaobo Ren; Tore Andre Kristensen; Jianying He; Zhiliang Zhang. Study of low-temperature effect on the fracture locus of a 420-MPa structural steel with the edge tracing method. *Fatigue & Fracture of Engineering Materials & Structures. vol. 41 (8).*

Zhiliang and Xiaobo provided the idea to study the low temperature effect on the ductility diagram. Tore performed the tests. I did the numerical work and wrote the draft. All the authors contributed to the revision and discussion of the paper.

5. Shengwen Tu; Xiaobo Ren; Jianying He; Zhiliang Zhang. Numerical study on the effect of Lüders plateau on the ductile crack growth resistance of SENT specimens. *Submitted to Internationa Journal of Frature*.

   I was inspired by an excellent work on Lüders plateau effect on crack driving force. I did the numerical work and wrote the draft. All the authors contributed to the revision and discussion of the paper.

In addition to the journal publications presented above, I have also presented work relevant to this thesis in the following international conferences/symposiums:

1. Shengwen Tu, Jian Shuai, Xiaobo Ren, Jianying He and Zhiliang Zhang,"CTOA Measurement From EL Curves With DWTT Specimen". ECF 21, June 20-24, 2016, Catania, Italy. *Oral Presentation*.
2. Shengwen Tu, Xiaobo Ren, Jianying He, Odd Magne Akselsen, Bård Nyhus and Zhiliang Zhang. "A ‘magic’ notched tensile specimen that avoids the Bridaman’s correction". International Symposium on Notch Fracture, March 29-31, 2017 , Santander, Spain. *Oral Presentation*.
3. Shengwen Tu, Xiaobo Ren, Jianying He, Odd Magne Akselsen, Bård Nyhus and Zhiliang Zhang. "A New Correction Method To Measure Equivalent Stress-Strain Curve With Notched Tensile Specimen".30th Nordic Seminar on Computational Mechanics, October 25-27, 2017, Copenhagen, Denmark. *Oral Presentation*.
4. Shengwen Tu, Xiaobo Ren, Jianying He, and Zhiliang Zhang. "Study on the effect of Lüders plateau on crack resistance curve with SENT specimens".ESIS Technical Meeting on Numerical Methods (TC8), January 15-16, 2018, Paris, France. *Oral Presentation*.
5. Shengwen Tu, Xiaobo Ren, Jianying He, and Zhiliang Zhang. "A notched cross-weld tensile testing method for determining the equivalent stress-strain curves of weldment". Workshop on “Damage and Damage Tolerance of

Welded Structures”, ESIS TC1 Spring Meeting, April 12-13, 2018, Prague, Czech Republic. *Oral Presentation*.

6. Shengwen Tu, Xiaobo Ren, Jianying He, and Zhiliang Zhang."Determining material’s equivalent stress-strain curve with axisymmetric notched tensile specimen". ECF 22, August 26-31, 2018. Belgrade, Serbia. *Oral Presentation*.

Contents

Chapter 1

Introduction

In this chapter, the motivation of the project and the aims of the PhD study will be introduced. In the following the structure of the thesis will be presented.

1.1 Motivation

The Arctic becomes a hot region to petroleum companies, considering its abundant undiscovered oil and gas resource. The assessment conducted by the United States Geological Survey indicates that about 30% of the world's undiscovered gas and 13% of the world's undiscovered oil may be found there [1]. However, many factors may affect the exploitation activities, including harsh environment, heavy drilling and shipping cost, as well as climate considerations [2] [3]. The exploration of hydrocarbon in these remote areas sets more strict requirements for the structural materials due to the harsh climate conditions. The overall objective of the project ARCTIC MATERIAL is to establish criteria and solutions for safe and cost-effective application of materials for hydrocarbon exploration and production in the Arctic regions. The aim of this PhD study is to characterize the tensile properties of Arctic materials and to model their effects on fracture.

From the viewpoint of fracture mechanics, low temperature is a strong challenges for the application of structural steels and pipeline steels in the Arctic region. The material's equivalent stress-strain curve may be influenced, for temperature dependent metallic materials. Measurement of equivalent stress-strain curves with smooth round bar or smooth specimens with rectangular cross-section is the general practice in engineering application. The limitation is that only the data before diffuse necking can be used directly. After diffuse necking, true stress-strain curve from tensile tests should be corrected. Performing the well-known Bridgman correction is difficult, since the minimum cross-section radius and the necking profile radius should be measured in the test. The Bridgman correction is not that accurate for some materials, due to its assumption that the equivalent stress is constant at the specimen minimum cross-secion after necking [4]. For weldments, determining the tensile properties becomes more difficult due to its inhomogeneity in nature. Requirements for measuring tensile properties at low temperatures are more strict, especially for the extensometer. Hence, a convenient and accurate method for determining tensile properties at low temperatures is necessary to conquer these problems mentioned above.

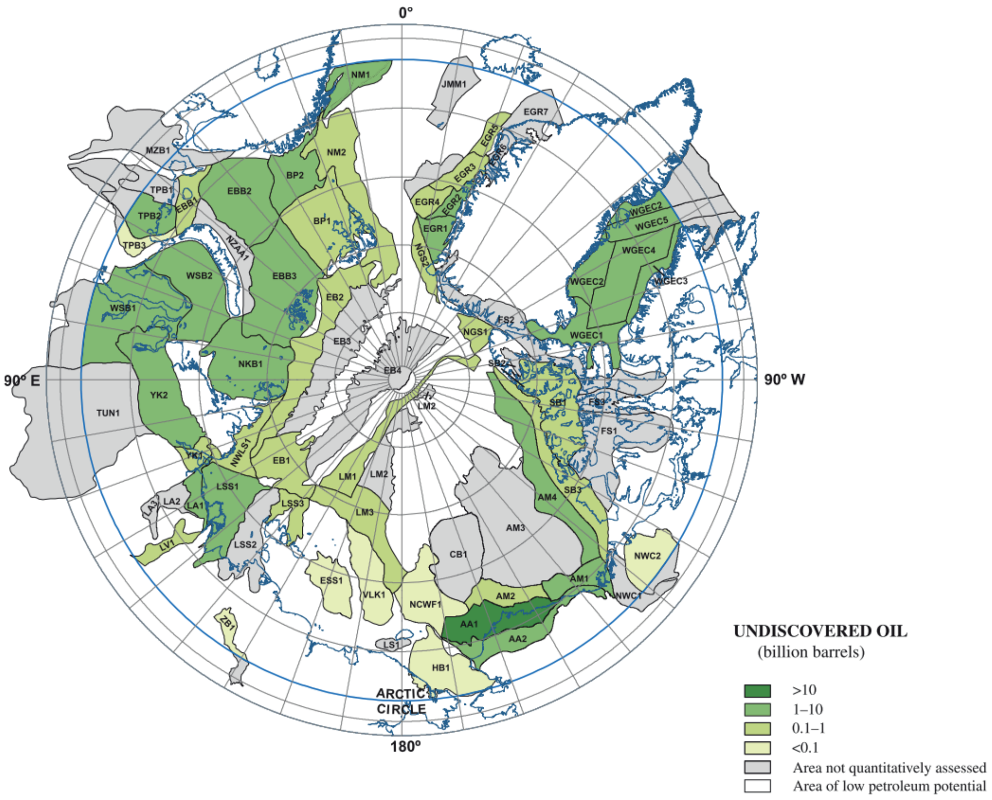

Figure 1.1: Distributions of undiscovered oil in arctic region predicted by the United States Geological Survey [1].

Fracture ductility depends signigicantly on the stress state which is usually characterized by stress triaxiality. For most experimental studies on ductility diagram, they were performed at room temperature. More work should be conducted to obtain a better understanding on low temperatures effect on fracture ductility. For temperature sensitive materials, low temperatures will influence the yield strength, strain hardening, ductility, as well as the Lüders plateau. It has been reported that increasing the yield stress or the Lüders plateau length will intensify the crack driving force [5]. However, research work on the effect of low temperature induced Lüders plateau on crack growth resistance is vary rare. Since the competition between the crack driving force and crack growth resistance determines the crack initiation and growth, more research work on the effect of the Lüders plateau on crack growth resistance is necessary to reduce the failure accidents which may result in unpredictable economic cost and environment pollution for petroleum industries.

1.2 Aim & Scope

The thesis is dedicated to develop novel and accurate methods for determining tensile properties of the Arctic materials and to study their effects on fracture response, towards a better understanding on the fracture behavior of metallic materials, as a result of the Arctic temperatures. Specifically, the dependence of low temperature on ductility diagram and the effect of Lüders plateau on crack growth are investigated. The research work are mainly focused on the following aspects:

- Methods for determining Equivalent stress-strain curves of materials and weldments at low temperatures.
- The effect of low temperatures on fracture ductility of materials at different stress states.
- The effect of low temperature induced Lüders plateau on ductile crack growth resistance.

1.3 Thesis outline

This thesis consists of an introductory section of five chapters and a collection of five separate research papers as appendix. A brief description of each chapter is introduced as follows:

Chapter 1

This chapter includes motivation, aim and scope and outline of the thesis.

Chapter 2

In this chapter, the state-of-art of methods on determining equivalent stress-strain curve of metallic materials, fracture locus are reviewed. Research work on Lüders Plateau is also introduced briefly.

Chapter 3

In this chapter the numerical models and experimental layout on axisymmetric tensile tests are introduced firstly. Numerical models with SENT specimens and the Gurson damage model are presented in the following.

Chapter 4

In this chapter a summary of the main results in this PhD study is presented.

Chapter 5

In this chapter some recommendations for future studies are briefly introduced.

Chapter 2

Literature Review

2.1 Equivalent stress-strain curve

For elastoplastic materials, the equivalent stress-strain curve, which governs materials' mechanical behavior, is vital to scientists and engineers for understanding and utilizing materials. Normally, the equivalent stress-strain curves are measured with smooth round bar specimens or rectangular cross-section specimens, according to testing standards, such as ASTM E8/E8M-13, ISO 6892-1, ISO 6892-2 and JIS Z2241. Usually, the engineering strain measured directly from the specimen is obtained by extensometer. The limitation for measuring strain with extensometer is that only data before diffuse necking is valid. However, it is necessary to derive the equivalent-strain curve in full range for numerical analyses in some situations, such as plastic forming or stress (or strain) filed under complex gradient. For this consideration, smooth round bar specimen is used and the true strain is calculated by the specimen minimum cross-section contraction. The radius in the specimen minimum cross-section can be measured by a linear variable displacement transducer or video-based Radial Extensometry [6]. With the development of high-speed camera and computer science, optical non-contact method has been proposed for two or three dimensional strain measurement [6, 7, 8, 9]. The so-called digital image correlation (DIC) method becomes very popular and is widely used for large strain measurement. However, it should be noticed that the true stress calculated by dividing the load by the specimen minimum cross-section area can not represent the equivalent stress after diffuse necking and should be corrected, see Fig. 2.1.

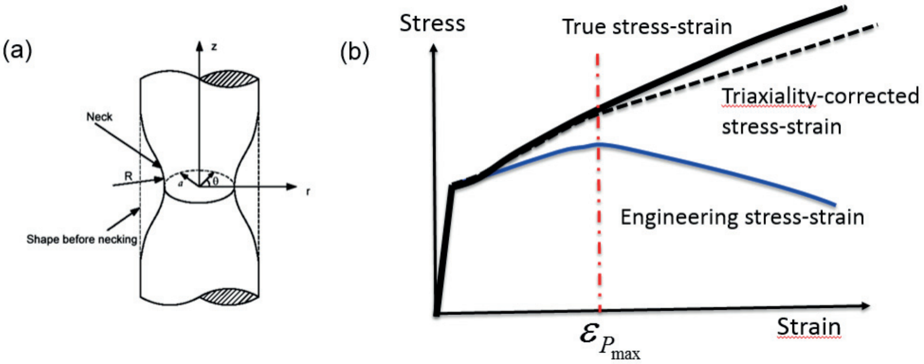

Figure 2.1: (a) Geometry of a necked tension sample; (b) Stress-strain curves from tensile tests.

2.1.1 Correction methods with smooth specimens

For tensile tests with smooth specimens, after diffuse necking, the deformation will be localized and stress state in the necking region will be triaxial. In the following, several methods in literature will be introduced for converting true stress to the equivalent stress.

Smooth round bar specimen

The correction methods with smooth round bar specimens have a very long history. The most popular correction formula was proposed by Brdigman [10]. Fig. 2.2 shows a necking geometry of a tension sample schematically. There are two assumptions for the derivation of the Brdigman correction function.

- In a certain surrounding of the neck the value of the equivalent stress, σ_{eq}, is constant (this region is shown in the Fig. 2.2a):
- In the surrounding of the minimal section, the shape of the transverse trajectories of the principal stress are arcs which are orthogonal to the longitudinal trajectories, see in Fig. 2.2b.

Due to the axial symmetry of the specimen, the equilibrium equation in the minimum cross section can be written as:

$$\frac{\partial \sigma_{rr}}{\partial r} + \frac{\partial \tau_{rz}}{\partial z} + \frac{\sigma_{rr} - \sigma_{\theta\theta}}{r} = 0 \tag{2.1}$$

where σ_{rr} and $\sigma_{\theta\theta}$ are stresses in r and θ direction. τ_{rz} is the shear stress. Ac-

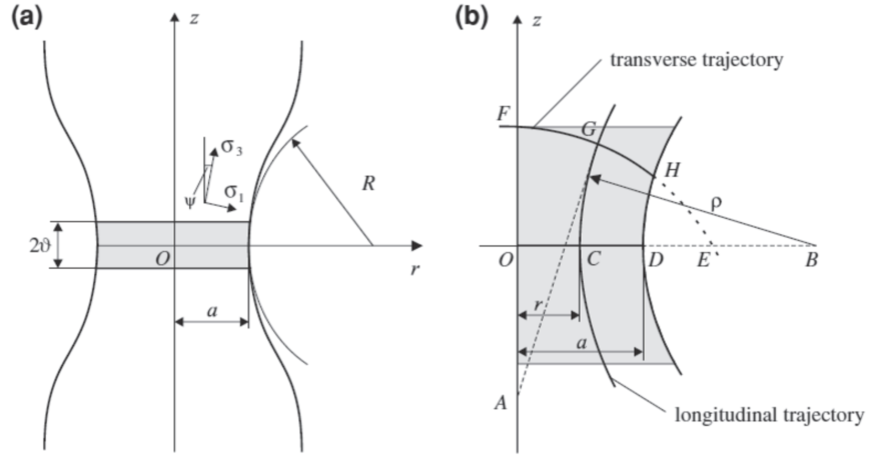

Figure 2.2: (a) Neck geometry in a tension sample; (b) principal stress trajectories in the meridian surface [11].

cording to the condition of volume conservation in plastic regime, in the minimal section the circumferential strain is equal to the radial strain. Then the third term in Eq. (2.1) vanish. According to the von Mises criteria, we have:

$$\sigma_{eq} = \sigma_{zz} - \sigma_{rr} \tag{2.2}$$

Taking into consideration of the relation Eq. (2.2) and the first assumption, Eq. (2.1) takes the following form:

$$\frac{\partial \sigma_{zz}}{\partial r} + \frac{\partial \tau_{rz}}{\partial z} = 0 \quad when \quad z = 0, 0 < r < a \tag{2.3}$$

σ_{zz} is the stress in tensile direction. In Fig. 2.2 (a), ψ is very small, τ_{rz} can be expressed as:

$$\sigma_{rr} \approx \sigma_1 \quad \sigma_{zz} \approx \sigma_3, \quad \tau_{rz} = (\sigma_3 - \sigma_1)\psi = \sigma_{eq}\psi \tag{2.4}$$

where σ_1 and σ_3 are the principle stresses. The second term in Eq. (2.3) can be written as:

$$\left(\frac{\partial \tau_{rz}}{\partial z}\right)_{z=0} = \left(\frac{\partial (\sigma_{eq}\psi)}{\partial z}\right)_{z=0} = \sigma_{eq}\left(\frac{\partial \psi}{\partial z}\right)_{z=0} + \psi \underset{0}{\left(\frac{\partial \sigma_{eq}}{\partial z}\right)_{z=0}} = \sigma_{eq}\left(\frac{\partial \psi}{\partial z}\right)_{z=0} \tag{2.5}$$

Since the angle ψ is very small, we obtain:

$$\psi(r, z) \approx tan\psi(r, z) = f_C^{'}(z) \tag{2.6}$$

where $f_C(z)$ is the appropriate longitudinal trajectory passing through point C on the OB axis (Fig. 2.2b). Calculating the derivative from Eq. (2.6):

$$\left(\frac{\partial\psi}{\partial z}\right) = f^{''}(z) \tag{2.7}$$

The curvature of the principal stress trajectory σ_3 can be calculated as:

$$\frac{1}{\rho} = \frac{\left|f^{''}(z)\right|}{(1 + f^{'}(z)^2)^{(3/2)}} \tag{2.8}$$

Inserting Eq. (2.6)-(2.8) into Eq. (2.5), in the plane $z = 0$, $\psi = 0$, we obtain:

$$\sigma_{eq}\left(\frac{\partial\psi}{\partial z}\right)_{z=0} = \sigma_{eq}\left[\frac{(1 + \psi^2(r, z))^{3/2}}{\rho}\right] = \frac{\sigma_{eq}}{\rho} \tag{2.9}$$

In Fig. 2.2(b) from the geometric relationship we have:

$$\rho^2 = BG^2 = AB^2 - AE^2 = OB^2 - OE^2 = (r + \rho)^2 - OE^2 \tag{2.10}$$

Eq. (2.10) is valid for any point G on the circle FGH, including the point H. Then we have:

$$r^2 + 2r\rho = a^2 + 2aR = OE^2 \tag{2.11}$$

$$\rho = \frac{a^2 + 2aR - r^2}{2r} \tag{2.12}$$

Inserting Eq. (2.9) and (2.12) to Eq. (2.3) and solve the equation we obtain:

$$\begin{aligned} \sigma_{zz} &= \sigma_{eq}\left[1 + ln(1 + \frac{a^2 - r^2}{2aR})\right] \\ \sigma_{rr} &= \sigma_{\theta\theta} = \sigma_{eq} \cdot ln(1 + \frac{a^2 - r^2}{2aR}) \end{aligned} \tag{2.13}$$

where R and a are the necking curvature radius and the minimum cross-section radius, respectively, as can be seen in Fig. 2.1 (a). The true stress σ_{tr} from tensile test with smooth round bar specimen is expressed as:

$$\sigma_{tr} = \int_0^a 2\pi r \sigma_{zz} dr / \pi r^2 = \sigma_{eq}[(1 + 2R/a) \cdot \ln(1 + a/2R)] \tag{2.14}$$

Now, the Bridgman correction factor $\zeta_{Bridgman}$ can be written as:

$$\zeta_{Bridgman} = \frac{1}{(1 + 2R/a) \cdot \ln(1 + a/2R)} \tag{2.15}$$

Davidenkov and Spiridonova [12] assumed that ρ is inverse proportional to r and can be expressed by the following formula:

$$\rho = \frac{Ra}{r} \tag{2.16}$$

The correction factor ζ_{D-S} obtained by Davidenkov and Spiridonova has the form:

$$\zeta_{D-S} = \frac{1}{1 + a/4R} \tag{2.17}$$

Indeed, the first correction was proposed by Siebel shortly after the Second World War [13]. Siebel's correction formula is not widely known, since it was published in German. By assuming that:

$$\rho = R\left(\frac{a}{r}\right)^n \tag{2.18}$$

At the free surface the necking curvature radius is linearly linked with the longitudinal trajectory radius and Siebel assumed $n = 0$. The correction factor can be written as:

$$\zeta_{Siebel} = \frac{1}{1 + a/3R} \tag{2.19}$$

As can be seen, the main difference for the three correction formulas is due to the different definitions of the longitudinal trajectory radius. For these three methods, it is not easy to measure the necking curvature radius, R. Le Roy [14] has presented an empirical relation with a/R and the true strain ε :

$$a/R = 1.1 \cdot (\varepsilon - \varepsilon_{p_{max}}) \tag{2.20}$$

where $\varepsilon_{p_{max}}$ is the strain corresponding to the maximum tensile load. Gromada et al. [11] performed numerical analyses with the perfectly plastic material, linear hardening material and nonlinear hardening material. Their results shows that the mostly used Bridgman correction yields the worst results, compared with the other two methods. In addition, these three methods are not accurate with the perfectly plastic material. Bao [15] performed numerical simulation with notched bar specimen and found that the stress distribution at the notch region differed significantly with the Bridgman solution. La Rosa and Risitano [4] applied the Bridgman correction to different steels, C40, FE36, AISI304, D98, etc., and found that with the increase of strain the error between the material equivalent stress and the Bridgman method corrected stress for steel D98 would be as large as 10.6% at the strain $\varepsilon = 1.35$.

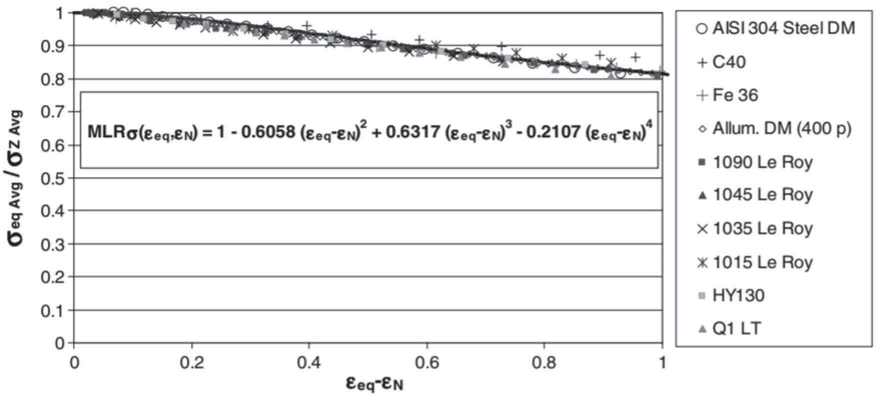

Figure 2.3: Ratio σ_{eq}/σ_{tr} vs.$(\varepsilon - \varepsilon_{p_{max}})$ for different materials [16].

Based on experimental and numerical observations, see Fig. 2.3, Mirone [16, 17] proposed an empirical correction function:

$$\sigma_{eq} = \sigma_{tr} \cdot [1 - 0.6058(\varepsilon - \varepsilon_{p_{max}})^2 + 0.6317(\varepsilon - \varepsilon_{p_{max}})^3 - 0.2107(\varepsilon - \varepsilon_{p_{max}})^4] \tag{2.21}$$

This method is very easy to practice, since the information needed are the true stress, true strain and the strain corresponding to diffuse necking. This method is based on fitting and special attention should be paid for its application.

There are also several methods to obtain equivalent stress-strain curves with hybrid experimental-numerical modeling method [18, 19, 20]. These methods work in this way: by comparing the engineering stress-strain curve or load-displacement curve from experiments and numerical analyses and adjusting the true stress-strain curves iteratively, until the convergence criteria is satisfied. These methods can provide accurate results. However, the limitation is that they are time consuming for iteration.

Rectangular cross-section specimen

For very thin plates, it is difficult to machine round bar specimens and smooth specimens with rectangular cross-section specimen become more practical. Due to the two types of flow instability (diffuse necking and localized necking), determination of the instantaneous minimum cross-section becomes considerably difficult. Most of the alternative methods for determining equivalent stress-strain curve or the equivalent stress-strain curve with rectangular cross-section specimen are based on inverse numerical analysis [21, 22, 23, 24, 25, 26] .

Ling [21] proposed a so-called *weighted average method* to measure the true stress-strain curve from rectangular cross-section specimen, by setting the power law hardening as lower bound and the linear hardening as the upper bound for the equivalent stress. The correction proposed by Ling is a kind of hybrid experimental-numerical modeling method and the determination of the weight constant is time consuming. Zhang [22] proposed a relation between the area reduction of the minimum cross-section and the measured thickness reduction of rectangular cross-section specimen. The area reduction can be normalized by the uniaxial strain at maximum load and the section aspect ratio. This method was furthur developed for anisotropic materials [23, 24]. It should be noted that Zhang's methods yield the true stress-strain curve as from a smooth round bar specimen and should be corrected to derive the equivalent stress-strain curve. Scheider [27] ran a serial of numerical simulations with different hardening exponents. A correction formula was proposed which depended on width reduction and strain. The aspect ratio effect on the true stress-strain curve was not considerd in the derivaton of the correction fucntion in [27]. Choung [25, 26] proposed a method to derive the equivalent stress for specimens with rectangular cross-section. The correction factor was a function of the equivalent plastic strain. However, the area reduction in the specimen minimum cross-section should be measured from specimens or pictures taken from the tests. The limitation of this method was that the shape of the minimum cross-section was simplified as rectangular.

2.1.2 Axisymmetrical notched specimens

As introduced above, the equivalent stress-strain curves of homogeneous materials can be measured from smooth round bar specimens or rectangular cross-section specimens (should be corrected after diffuse necking). However, it is a strong challenge to measure the equivalent stress-strain curve of inhomogenous materials, like weldments. The mechanical properties of base material, weld metal and heat affect zone are different to each other. The load versus elongation curve derived from cross weld tension specimen can not be used in the assessment of failure behavior of weldments. Since the curve is strongly dependent on the strength match, sample machining, locations of necking and fracture. For this consideration, Zhang [28] proposed to measure the true stress-strain curve of inhomogenous materials with axisymmetrical notched specimen. The geometry of a notched specimen is presented in Fig. 2.4 schematically. By introducing a notch in the specimen center, the deformation is restrained in the notch region. A G factor which depends on the notch curvature radius R_0, the minimum cross-section diameter D_0 and the strain at the maximum tensile load $\varepsilon_{p_{max}}$ was proposed:

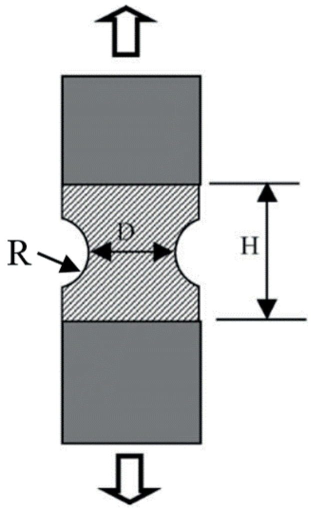

Figure 2.4: Axisymmetrical notched cross weld tensile specimen

$$G = \left[1.077 + 0.18777\left(\frac{D_0}{R_0}\right) - 0.01313\left(\frac{D_0}{R_0}\right)^2\right] \cdot (1.053 - \varepsilon_{p_{max}}) \tag{2.22}$$

With this G factor, the true stress calculated by dividing the load with respect to the minimum cross-section area from this notched specimen, $\sigma_{tr,notch}$, can be converted to the true stress from a smooth round bar specimen, $\sigma_{tr,smooth}$:

$$\sigma_{tr,smooth} = \sigma_{tr,notch}/G \tag{2.23}$$

Zhang [28] also presented that the notched can be located in a target material zone for inhomogeneous material when the geometry condition $D_0 \leq H$ is satisfied. H is the height of the target material zone. It should be noted that the true stress-strain curves derived with this method need to be corrected. Methods introduced in section 2.1.1 can be used.

2.2 Fracture dependence on stress state

For damage model considering void nucleation, growth and coalescence, it has been reported that fracture of ductile metals is strongly depends on hydrostatic stress [29, 30, 31, 32, 33, 34, 35]. Recent studies indicate that fracture ductility also depends on the loading history. In this section, the dependence of fracture strain on stress state will be briefly reviewed.

2.2.1 Ductility Diagram

Bridgman [10] reported that the fracture surface area of tensile specimen decreased significantly with the increase of hydrostatic pressure. Kao [36] performed tensile tests of 1045 spheroidized steel under hydrostatic pressure and found the same result as Bridgman. Pictures of fractured tensile bars under applied pressure can be seen in Fig. 2.5. By quantitative metallography and fractography study, Kao demonstrated that the influence of superimposed hydrostatic pressure on tensile fracture of 1045 spheroidized steel was such that void nucleation is suppressed, leading to larger post-uniform strains under pressure and a transition of the fracture surface from the cup-cone mode under atmospheric pressure to a slant structure under high pressure, see Fig. 2.5.

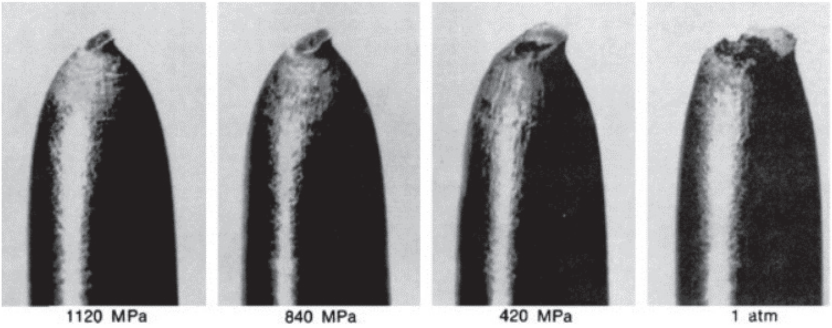

Figure 2.5: The appearance of the fractured tensile bars under applied pressure [36].

Stress triaxiality T, which is defined by the ratio of the mean stress, σ_m ($\sigma_m = (\sigma_{11} + \sigma_{22} + \sigma_{33})/3$), and the von Mises equivalent stress, σ_{eq}, ($T = \sigma_m/\sigma_{eq}$), is widely used to characterize the hydrostatic pressure effect [37, 38, 39, 40] and the crack tip constraint [41, 42, 43]. According to Bridgman's analytical solution, the stress triaxiality in necked tensile specimen minimum cross-section center can be written as:

$$T = 1/3 + ln(1 + \frac{a}{2R}) \tag{2.24}$$

where R is the neck curvature radius and a is the radius from the minimum cross-section center to the free surface. Inspired by Eq. (2.24), stress triaxiality at differ-

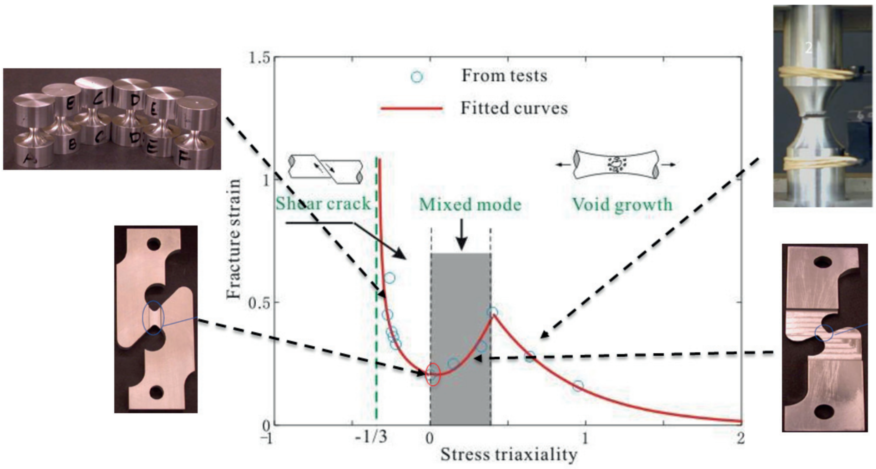

Figure 2.6: Dependence of the equivalent strain to fracture on the stress triaxiality [48].

ent levels can be obtained by varying the ratio of a and R of axisymmetric notched specimens [37, 44, 45, 46, 47].

Bao et al. [48] performed a series of tests including upsetting tests, shear tests and tensile tests on 2024-T351 aluminum alloy, including a wide range of the stress triaxiality. Meanwhile, parallel numerical analyses were performed to capture the stress and strain evolution. A strain-weighted stress triaxiality was used to characterize the stress state at fracture initiation point:

$$T_{av} = \int_0^{\varepsilon_f} T d\varepsilon_f \tag{2.25}$$

where ε_f is the equivalent strain at fracture.

ε_f was then plotted with respect to the strain-weighted stress triaxiality, see Fig. 2.6. The curve consists of three branches:

- For $-\frac{1}{3} \leq T_{av} < 0$, ε_f decreases with the increase of T_{av}.
- For $0 \leq T_{av} < 0.4$, ε_f increases with the increase of T_{av}.
- For $0.4 \leq T_{av} < 0.95$, ε_f decreases with the increase of T_{av}.

When the stress triaxiality is relatively high ($T_{av} \geq 0.4$ in Fig. 2.6), the fracture mechanism is widely acknowledged due to the void nucleation, growth and coalescence. The Gurson damage model can be used to simulate the fracture process [49, 50]. When the stress triaxiality is relatively low ($T_{av} \leq 0.4$ in Fig. 2.6), shear stress plays an important role on the fracture ductility. Wierzbicki [51] compared results from the constant equivalent strain criterion, the Xue–Wierzbicki (X–W) fracture criterion [52, 53], the Wilkins (W) [54], the Johnson–Cook (J–C) [37, 55], the CrachFEM fracture models, the maximum shear (MS) stress model [56], and the fracture forming limit diagram (FFLD) [57, 58] with experimental data and found out that the maximum shear stress model can well predict the experimental results, except those for axisymmetric round bar specimens. The partial success of the maximum shear stress should not be surprising because the maximum shear stress criteria carries information on the second and third stress invariants [53].

Recent studies show that the the fracture ductility also depends on the relationship between the principle stresses, which is characterized by the Lode parameter L [59, 60, 61, 62, 63] or the Lode angle parameter $\overline{\theta}$ [64, 65]:

$$L = \frac{2\sigma_{22} - \sigma_{11} - \sigma_{33}}{\sigma_{11} - \sigma_{33}} \tag{2.26}$$

$$\overline{\theta} = 1 - \frac{6\theta}{\pi} \tag{2.27}$$

θ is the Lode angle and has the range of $0 \leq \theta \leq \pi/3$. Apparently, the value of the Lode parameter and the Lode angle parameter have the same range of $\{-1, 1\}$. Typically, for generalized axisymmetric tension, $L = -1, \overline{\theta} = 1$; for generalized shear, $L = \overline{\theta} = 0$. Wierzbicki and Xue [53] presented that the condition $\sigma_{33} = 0$ uniquely related the parameters T and $\overline{\theta}$ or L

$$cos[\frac{\pi}{2}(1 - \overline{\theta})] = -\frac{27}{2}T(T^2 - \frac{1}{3}) \tag{2.28}$$

A plot of Eq. (2.28) is shown in Fig. 2.7. Typical stress state from test specimens in Fig. 2.6 are also marked. By taking the Lode parameter into consideration, a general 3D fracture locus was postulated by Bai and Wierzbicki [65], Fig. 2.8. It can be seen that both the stress triaxiality and the Lode angle parameter will affect the fracture ductility.

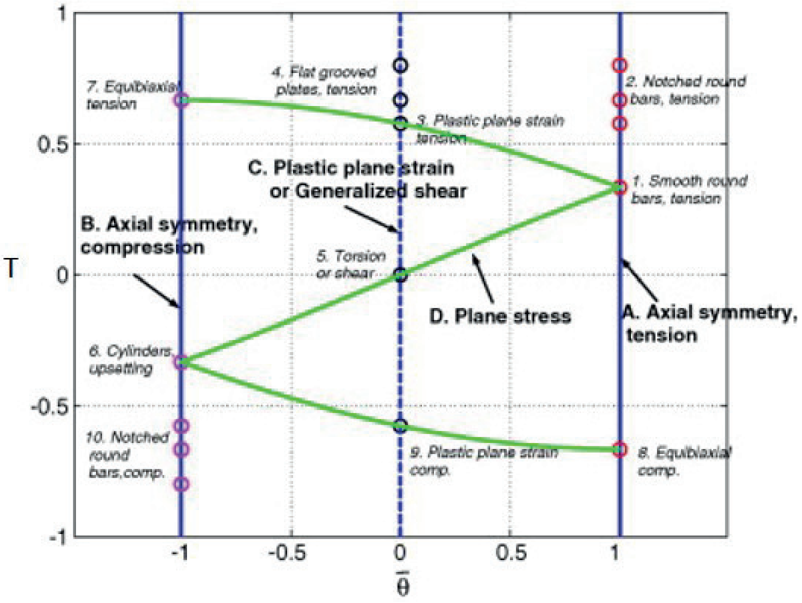

Figure 2.7: Conceptual representation of the initial stress states on the plane of T and $\overline{\theta}$ [64].

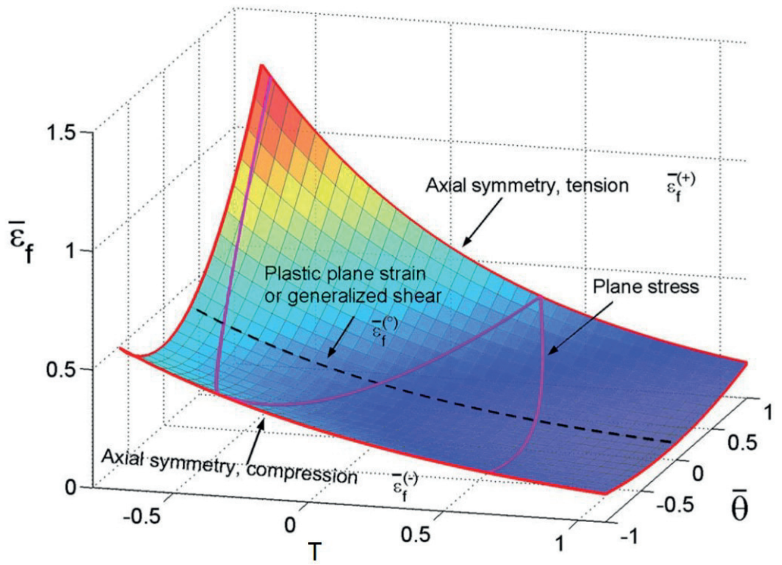

Figure 2.8: A general 3D fracture locus postulated by Bai and Wierzbicki [65].

2.2.2 Loading path, Loading rate and temperature

The fracture ductility may also be influenced by the loading path [66, 67, 68, 69] [70], loading rate [37, 71, 45, 46] and the temperature [71]. For most studies about the loading path effect on the fracture locus, the axisymmetric tensile bars were widely used experimentally and the unit cell model were used numerically. Due to the geometry symmetry of notched specimens, the Lode angle parameter and the Lode parameter for a given material point on the specimen minimum cross-section is constant and the fracture locus was usually constructed with respect to stress triaxiality.

Benzerga et al. [67] investigated the effect of loading path on the fracture locus with symmetric round bars. By prestraining the large plate specimen up to incipient necking first and then cutting round bar specimens out to perform tensile test till rupture, a step-jump in stress triaxiality was fulfilled. Comparison of the fracture locus with and without path change showed that the loading path also affected the fracture ductility. Numerical results from unit cell model also showed the importance of non-proportional loading paths on the predicted fracture ductility [67, 68, 70].

The influence of loading rate on fracture ductility were investigated via torsion tests [37, 72] or Hopkinson bar tests [71, 45, 46]. Johnson and Cook [37, 72, 73] performed torsion tests of OFHC copper, Armco iron and 4340 steel over a range of strain rates. They reported that the fracture ductility dependence on the loading rate was insignificant. Børvik and Hopperstad [71, 45] [46] conducted Hopkinson tensile bar tests at various loading rates with symmetric tensile bars machined from Weldox 460E steel. They found out that the fracture ductility was less sensitive to the loading rate.

For most of the experimental tests for deriving the fracture locus, they were performed at room temperatures. To study the temperature effect on fracture locus, Børvik et al. [71] performed Hopkinson tensile bar tests with temperatures ranges from 100°C to 500°C. Their test results indicated that for the temperatures in the range of {100°C , 500°C}, the temperature effect on fracture ductility of the Weldox 460 E steel was not obvious. Michael and Richard [74] performed quasi-static tensile test with Al-Cu-Mg-Ag alloy from 25°C to 150°C. They found that the temperature effect on fracture ductility for axisymmetric notched specimens can be neglected.

It should be noted that the studies on effects of loading path, loading rate and temperature were in relatively high stress triaxiality regime (unit cell model or axisymmetric notched bar specimens). The investigation for small or negative stress triaxiality is very limited in literature. Meanwhile, the temperature effect were investigated at temperatures higher than room temperatures. The studies at low temperatures are almost blank.

2.3 Lüders Plateau effect on ductile fracture

2.3.1 Lüders Plateau

For some metallic materials, common to low-carbon steels and certain Al-Mg alloys, the so-called Lüders plateau which is influenced by loading rate, ferrite grain size, yield stress, et al. [75, 76, 77, 78, 79, 80, 5, 81] may occur in uniaxial tension test. The mechanism that stimulates the appearance of the Lüders plateau is known as *dynamic strain aging* or the inhibition of dislocation motion by interstitial atoms (in steels, typically carbon and nitrogen), around which *atmospheres* or *zones* naturally congregate. Tsuchida et al. [81] reported that the Lüders plateau elongation (length) decreased with the increases of temperature and the ferrite grain size. Meanwhile, it increased with the increase of the lower yield stress. In the Arctic region, the temperature is considerably low. For materials with Lüders plateau, the plateau length is expected to increase. The influence of Lüders plateau on fracture behavior should be taken into consideration.

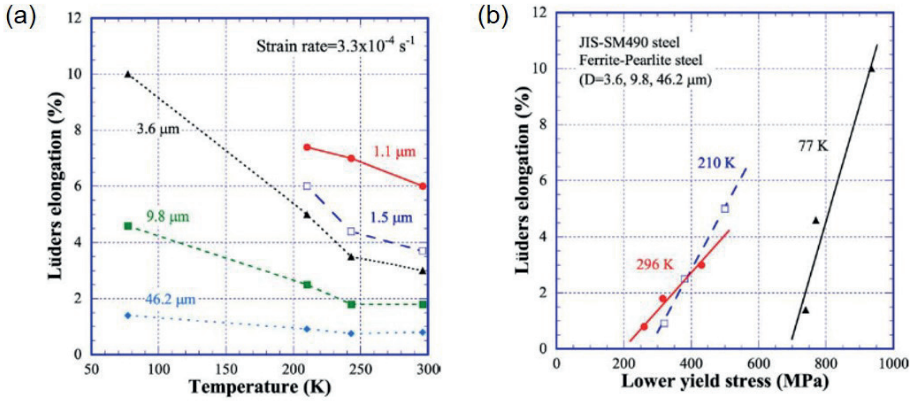

Figure 2.9: The effects of temperature, ferrite grain size and lower yield stress on the Lüders plateau length [81].

2.3.2 The effect of the Lüders plateau on crack driving force and crack initiation

In fracture mechanics, the competition between the crack driving force and materials' resistance curve (R-curve) determines crack initiation and growth. The crack driving force can be defined as the force that opens the crack, while R-curve is utilized to characterize materials' ability to resist crack initiation and growth. Studies on the the effect of Lüders plateau on crack driving force and crack initiation are very limited. In the guidelines for fracture assessment of pipelines, such as DNV-F101 (2013) and Electric Power Research Institute (EPRI) method (1981), the Lüders plateau is not considered.

Dahl et al. [5] has investigated the effect of the Lüders plateau on crack driving force with single edge notched tensile (SENT) specimen. In Dahl's work, the Lüders plateau was simplified by keeping the stress as a constant and equaling to the yield stress. The crack tip opening displacement was used to characterize the crack driving force. By varying the plateau length from 0 to infinite, they found out that the crack driving force was intensified with the increase of Lüders plateau length, see Fig. 2.10.

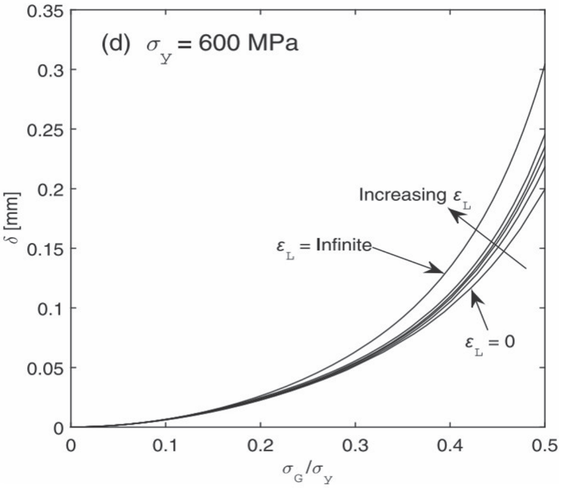

Figure 2.10: The effects of the Lüders plateau on crack driving force [5].

Nourpanah and Taheri [82] investigated the effect of the Lüders plateau on fracture response of pipeline under bending. Same simplication of the Lüders plateau in Dahl's work [5] wad applied. They concluded that the constraint ahead of the tip was reduced due to the existance of the Lüders plateau and longer plateau yielded larger reduction. They further investigated the effect of Lüders plateau on the equiavlent plastic strain distribution ahead of the crack tip with modified boundary layer model and found out that the equivalent plastic strain was noticeably higher for mateirals with Lüders plateau. Main resutls from ref. [82] can be seen in Fig. 2.11.

Studies on the effect of the Lüders plateau on crack growth resistance is almost

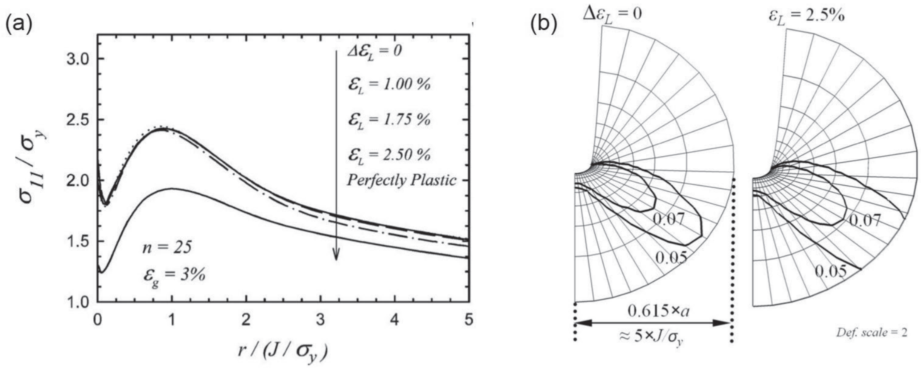

Figure 2.11: The effects of the Lüders plateau on crack tip opening stress and equivalent plastic strain distribution [82].

empty at present. For materials exhibiting the Lüders plateau, as presented in above, the plateau length will increase with the low temperature in the Arctic. Regarding to the safe service of metallic facilities, deep understanding of the fracture response is very important. More research work on the effect of the Lüders plateau on fracture of metallic materials is necessary.

Chapter 3

Methods and models utilized in the PhD study

In this chapter, the experimental layout and numerical analyses utilized in this dissertation will be introduced briefly.

3.1 Determining equivalent stress-strain curve with notched specimens

As reviewed in section 2.1, Zhang proposed to utilize axisymmetric notched tensile specimens to measure true stress-strain curves of weldment [28]. Drawbacks of Zhang's method are that when the strain is large, the error between the true stress-strain curves from notched specimens and from smooth round bar specimen occurs; on the other hand, the obtained true stress-strain curves should be converted to the equivalent stress-strain curve. Considering these issues, we did some further research to solve these two problems. The detailed information can be referred to *Paper-I-III* .

3.1.1 Axisymmetric specimen with 'magic' notch

Consider the results in ref. [28], we tried to identify a 'magic' notch geometry, with which true stress-strain curves from notched specimens can be converted to the equivalent stress-strain curves directly. We ran numerical modelling to search the special notch geometry. The geometry of notched specimens we used can be referred to Fig. 2.4. The flow stress-strain curves input for numerical analyses obeying the following power-law:

$$\sigma_f = \sigma_0(1 + \frac{\overline{\varepsilon_p}}{\varepsilon_0})^n \tag{3.1}$$

where σ_f, σ_0 are the flow stress and yield stress. $\overline{\varepsilon_p}$ and ε_0 are the equivalent plastic strain and yield strain. n is the hardening exponent. In this work, we varied n from 0.05 to 0.2, representing most engineering steels. Notch geometry is characterized by the ratio of initial specimen minimum cross-section radius a_0 and notch curvature radius R_0, a_0/R_0. In this work, a_0/R_0 varied from 1 to 3 were considered. Typical mesh can be seen in Fig. 3.1.

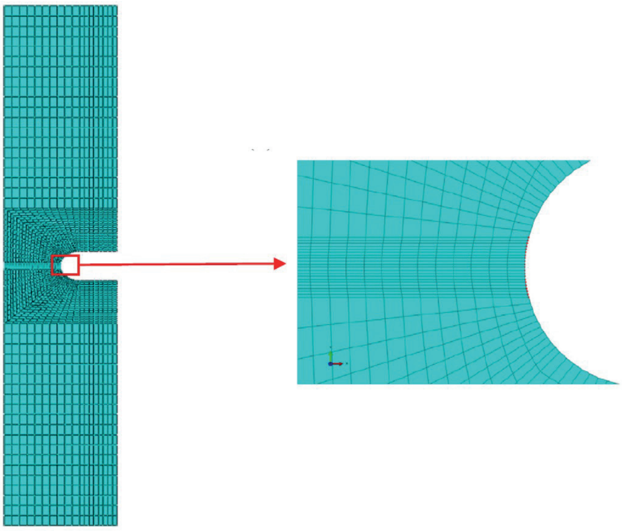

Figure 3.1: Typical mesh of the notched tensile specimen.

True stress-strain curves from notched specimens were converted by a G^m factor, which was defined by the ratio of true stress from notched specimen and the equivalent stress at the strain equal to n:

$$G^m = \frac{\sigma_{tr,notch}}{\sigma_{eq}} |_{\varepsilon=n} \tag{3.2}$$

After the identification of the 'magic' notch with $a_0/R_0 = 2$, we tried to establish the relationship between G^m and n, see Fig. 3.2. We further applied this 'magic' notch for materials with Lüders plateau. The geometry requirements for its application to determine equivalent stress-strain curves of weldment were studied. Information about this 'magic' notch method can be referred to paper-I.

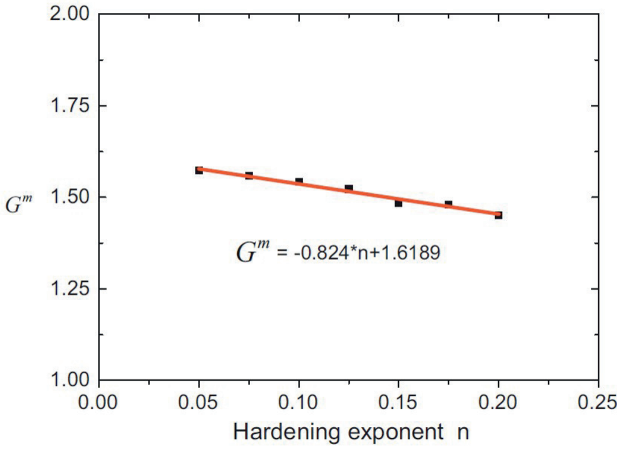

Figure 3.2: G^m vs. n for the magic notch.

3.1.2 Axisymmetric specimens with 'any' notch

From the section 2.2, we know that symmetric tensile bars with sharper notch fails at smaller fracture strain. For the 'magic' notch, the fracture strain obtained maybe much smaller than that from a smooth round bar specimen. Considering this, we tried to find a way to convert the true stress-strain curves from symmetric tensile bar specimens with 'any' notch geometries to equivalent stress-strain curves. The layout of this work is shown in Fig. 3.3.

This work was performed numerically. The flow stress-strain curves for this study is defined as Eq. (3.1). Due to the symmetry of the specimen, only one quarter of the specimen was modeled and symmetric boundary conditions were applied. The notch geometry was characterized by a_0/R_0. In this study, a_0/R_0 varied from 0.25 to 3 were considered. True stress-strain curves from the notched specimens for the perfectly plastic material is shown in Fig. 3.4. The trend of the true stress-strain curves from different notched specimens were utilized. Similar to the method in section 3.1, the ratio between the true stress and the equivalent stress at several strain levels were calculated:

$$\xi = \frac{\sigma_{tr,notch}}{\sigma_{eq}} |_{\varepsilon} \tag{3.3}$$

The idea in this work was to link the ratio ξ as a function the notch geometry and material's strain hardening. ξ vs. ε for the symmetric notched specimens with $a_0/R_0 = 3$ is presented in Fig. 3.5 (a). Curves from different hardening

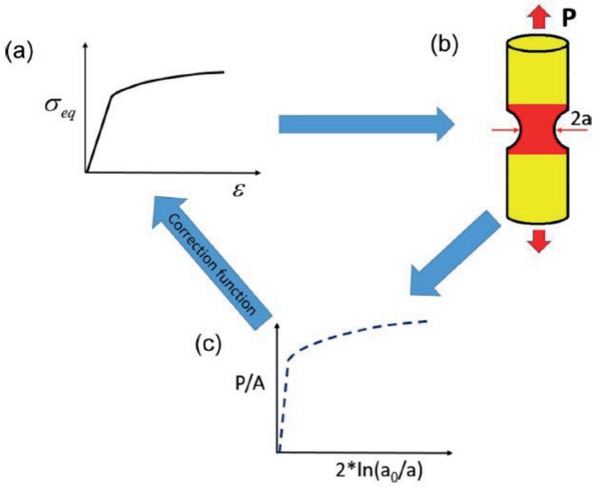

Figure 3.3: Layout of the present study: (a) Assumed material's equivalent stress-strain curve; (b) Numerical tensile tests with axisymmetric notched tensile specimens, material in red can be undermatched, overmatched or evenmatched with the base material in yellow; (c) True stress-strain curve for the notched specimen obtained from (b). With the proposed correction function, true stress-strain curve in Fig. 3.3 (c) can be corrected back to Fig. 3.3 (a).

show similar trend and are the normalized, by taking the value of ξ at $\varepsilon = 0.8$ as reference. After the normalization, curves in Fig. 3.5 (a) collapse into one, which can be linearly fitted. This applies for all the notched specimens with different a_0/R_0.

$$\xi/\xi_{\varepsilon=0.8} = [b_1 \cdot \varepsilon + b_2]_{a_0/R_0} \tag{3.4}$$

All the reference values of $\xi_{\varepsilon=0.8}$ are plotted with respect to the hardening exponent n. Curves for different a_0/R_0 in Fig. 3.6 (a) looks similar to each other and are then normalized by $\xi_{\varepsilon=0.8,n=0}$. After the normalization, all the curves in Fig. 3.6 (a) overlap to each other and can be fitted as a function of n.

$$f(n) = -0.22942 \cdot n^2 - 0.36902 \cdot n + 1 \tag{3.5}$$

By combining Eq. (3.4) and Eq. (3.5), the ratio ξ can be expressed as Eq. (3.6).

$$\xi = f(n) \cdot \xi_{\varepsilon=0.8,n=0} \cdot [b_1 \cdot \varepsilon + b_2]_{a_0/R_0} \tag{3.6}$$

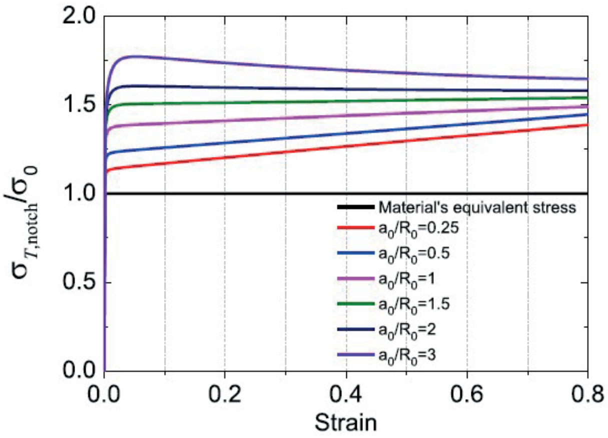

Figure 3.4: Normalized true stress-strain curves for the perfectly-plastic materials from different specimens with different notch geometries. The material's equivalent stress-strain curve is denoted as black.

Recall that in Fig. 3.5, the product of the second and the third term in Eq. (3.7) is the linear fitting curve for the curve corresponding to $n = 0$. Then, Eq. (3.7) can be rewritten as:

$$\xi = f(n) \cdot [b_{1,n=0} \cdot \varepsilon + b_{2,n=0}]_{a_0/R_0} \tag{3.7}$$

Now, we need to calculate the slope $b_{1,n=0}$ and interception $b_{2,n=0}$ for different a_0/R_0 with $n = 0$. The values of $b_{1,n=0}$ and $b_{2,n=0}$ are plotted against a_0/R_0. The curves in Eq. (3.7) are then fitted by second order polynomial functions:

$$b_{1,n=0} = 0.03232 \cdot (a_0/R_0)^2 - 0.27 \cdot (a_0/R_0) + 0.3866 \tag{3.8}$$

$$b_{2,n=0} = -0.04084 \cdot (a_0/R_0)^2 + 0.3557 \cdot (a_0/R_0) + 1.0577 \tag{3.9}$$

With Eq. (3.7)-(3.9), ξ is expressed as a function of n (representing material property) and a_0/R_0 (representing notch geometry effect). Now, we can utilize Eq. (3.7) to convert true stress-strain curves from any notched specimens to materials' equivalent stress-strain curves. We verified this method numerically and experimentally and very good results were obtained. More detailed information about this method can be referred to paper-II and paper-III.

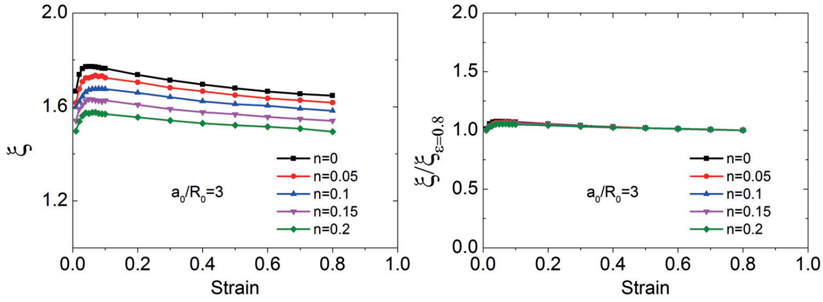

(a) (b)

Figure 3.5: (a). ξ vs. ε for the symmetric notched specimens with $a_0/R_0 = 3$; (b) Normalized curves of Fig. 3.5 by $\xi_{\varepsilon=0.8}$.

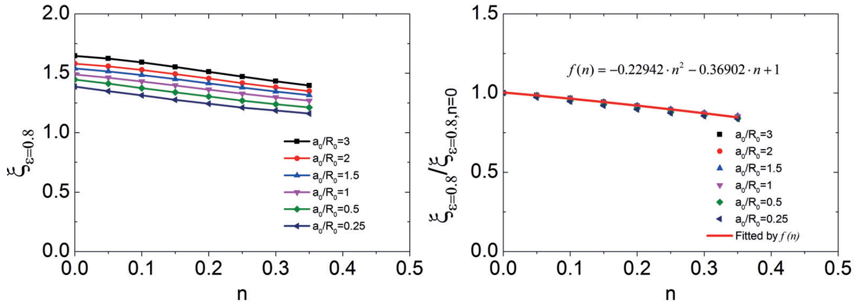

(a) (b)

Figure 3.6: (a). $\xi_{\varepsilon=0.8}$ vs. n for the symmetric notched specimens with different a_0/R_0; (b) Normalized curves of Fig. 3.6 by $\xi_{\varepsilon=0.8,n=0}$.

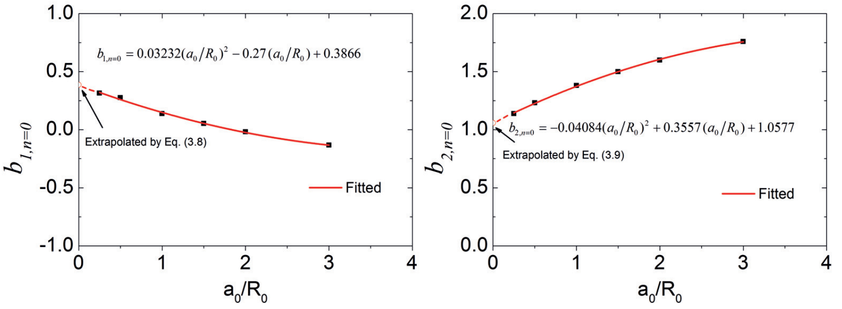

(a) (b)

Figure 3.7: (a). $b_{1,n=0}$ plotted as a function of a_0/R_0; (b) $b_{2,n=0}$ plotted as a function of a_0/R_0.

3.2 Experimental study on low temperature effect on fracture locus

As reviewed in section 2.2, studies on the low temperature effect on ductility diagram is very limited, if available. For this consideration, we did a series of tensile tests (45 tests in total) with axiasymmetric notched tensile specimens and smooth round bar specimens, see Fig. 3.8. Details about this study are presented in Paper-IV.

3.2.1 Experimental layout

The tests were performed at room temperature, -30°C and -60°C with an universal test machine Instron 5985, with the loading cell of 250 KN. a_0/R_0 varied from 0.5 to 3, covering a wide range of initial stress triaxiality. A liquid nitrogen-cooled temperature chamber was used to create low temperature environment. The air inside of the temperature chamber was replaced with nitrogen gas first, in order to avoid ice formation on the specimen surface. On one side of the temperature chamber, there is a window, through which the inside of the temperature chamber can be observed clearly. A digital high-speed CCD camera with the resolution of 2448×2050 pixels was located besides the window to take pictures of the specimen during the test, with the framing rate of 1 frame per second. All the tests were performed in displacement control manner with the cross-head speed of 0.3 mm/minute. During the tests, the force was recorded with the same camera framing frequency. The test system is shown in Fig. 3.9.

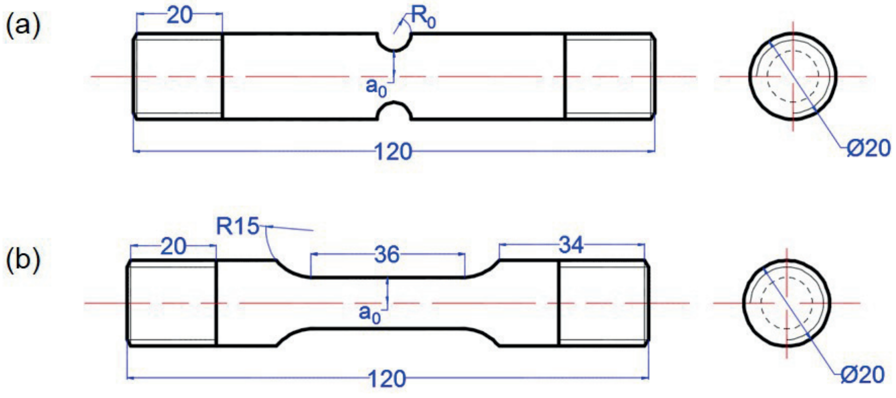

Figure 3.8: Sketches of tensile specimens: (a) Axisymmetric notched specimens; (b) Smooth round bar specimens.

Inside the temperature chamber, there were two LED lights and a two-plane mirrors system, see Fig. 3.10 (a). The two-plane mirrors system consisted of 2 plane

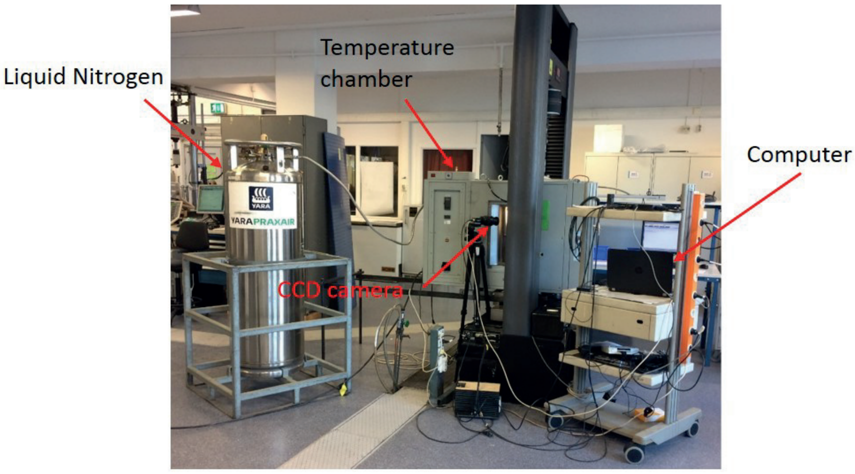

Figure 3.9: Test system in this study.

mirrors with the angle of 135°, as illustrated in Fig. 3.10 (b). The specimen and the camera were located on the angle bisector of the two-plane mirrors system. Therefore, the deformation of the specimen can be observed in two perpendicular directions during the test, according to the plane image formation principle. The consideration of using the two-plane mirrors system is that, due to the localized deformation on necked smooth and axisymmetric notched specimens, it is more accurate to use the average value of minimum cross-section diameter in two orthogonal directions to calculate the current minimum cross-section area, instead of only one direction. By adjusting the position of the LED lights, the specimen images can be located in the LED light images center. The camera was set in mono mode in the test. A very strong grey-value gradient can be formed between the specimen images and the picture background, for the purpose to use the edge tracing method to measure the specimen deformation. Fig. 3.10 (c) shows a picture of a smooth specimen taken with the camera in the beginning of the test.

3.2.2 Edge tracing method

Digital pictures consist of numbers of pixels which depends on the resolution of the digital camera. Each pixel in the picture represents a grey-value. From black to white, the grey-value ranges from 0 to 255. Digital pictures can be read by Matlab and grey-value of each pixel can be output and stored in a matrix for analysis. For one arbitrary row in the digital pictures, peak values of the derivative (absolute value) of grey-value can be found, due to the strong contrast between the specimen images and the background, as shown in Fig. 3.11 (a). There were several peak values in Fig. 3.11 (a), however, only the two maximum peak values were regarded

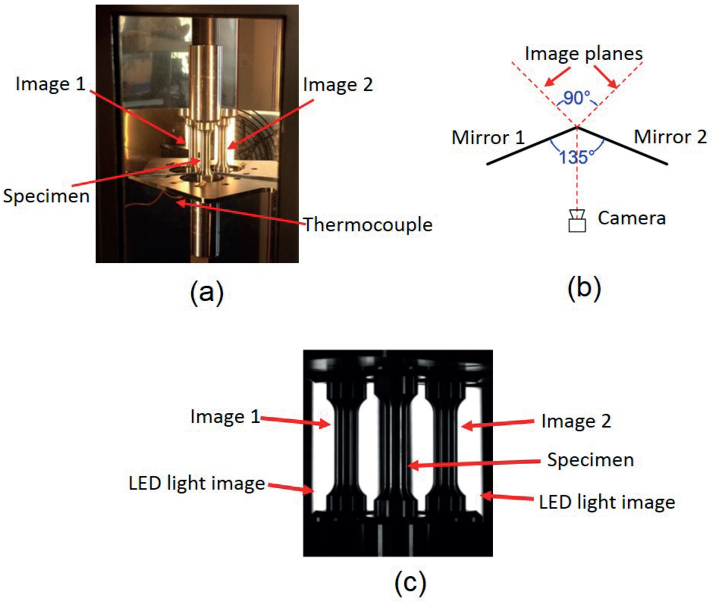

Figure 3.10: (a) Layout of the inside of the temperature chamber; (b) Illustration of the two-plane mirrors system; (c) Picture of smooth round bar specimen taken at the beginning of the test.

as the boundaries between the specimen image and the background. The small peak values were caused by the white color on the specimen image, formed due to light reflection. The pixel numbers between the two boundaries represent the corresponding cross-section diameter. By scanning each row of the picture, the edges of the specimen image can be captured, together with the minimum cross-section diameter, shown as red curves in Fig. 3.11 (b). Due to the existence of necking or notch, the deformation was localized in the necking /notch region. The edge tracing method was therefore mainly focused on the necking/notch region to save calculation cost.

With the edging tracing method, we ran numerical analysis in parallel to capture the stress triaxiality evolution during the test. The numerical simulation was similar to those in section 3.1. The fracture initiation point was defined by the strain corresponding to the sudden drop of load on the load-strain curve. Results show that both the strength and strain hardening characterized by the strain at the maximum load increase with temperature decrease down to -60°C. Somewhat unexpected, the fracture strains (ductility) of both smooth and notched specimens at temperatures down to -60°C do not deteriorate, compared with those at room tem-

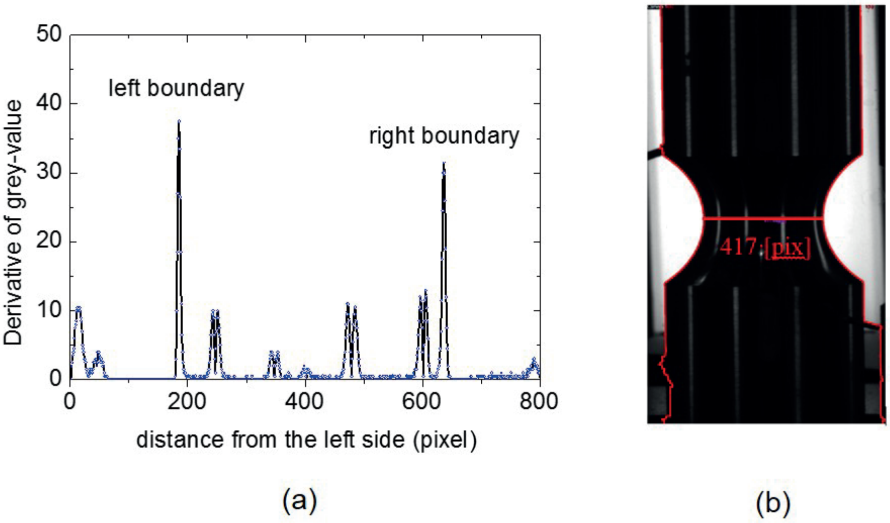

Figure 3.11: Illustration of the edge tracing method: (a) Absolute value of derivative of the grey-value; (b) Minimum cross-section measurement with the application of the edge tracing method.

perature. Combined with numerical analyses, it shows that the effect of low temperatures (down to -60°C) on fracture locus is insignificant. The tests results were summarized in Paper-IV.

3.3 Damage models used to study the Lüders Plateau effect on ductile crack growth resistance

As mentioned in section 2.3, for materials exhibiting Lüders Plateau, low temperature in the Arctic will amplify the plateau length. Studies on the low temperature induced Lüders Plateau effect on fracture response is very limited. In this section, we utilized the Gurson damage model to investigate the effect of Lüders Plateau on ductile crack growth resistance ($CTOD - \Delta a$ curve) with SENT specimens. Main findings in this study are presented in Paper V.

3.3.1 Gurson damage model

The mechanism of ductile fracture failure in metallic materials is widely acknowledged as the micro void nucleation, growth and coalescence. Gurson [83] proposed a constitutive model for ductile materials incorporating voids, considering the hydrostatic stress effect on plastic yielding and void growth. The original Gurson damage model was further modified by Tvergaard and Needleman [84, 85, 86].

Finally the yield surface has the following form and known as Gurson-Tvergaard-Needleman model:

$$\phi(q, \sigma_f, f, \sigma_m) = \frac{q^2}{\sigma_f^2} + 2q_1 f \cosh\left(\frac{3q_2\sigma_m}{2\sigma_f}\right)^2 - 1 - (q_1 f)^2 = 0 \qquad (3.10)$$

where q is von Mises stress, σ_f is the flow stress of the matrix material and is a function of equivalent plastic strain. σ_m is the mean stress; q_1 and q_2 are the parameters introduced by Tvergaard [84]; f is the void volume fraction. In this study, $q_1 = 1.5$ and $q_2 = 1$ are used for all the numerical analyses.

In this study, the increase of the void volume fraction is solely contributed by the void growth and no void nucleation is considered during loading. Due to the incompressible nature of the matrix material, the void volume increment can be expressed as:

$$df_{growth} = (1 - f)d\varepsilon^p : \mathbf{I} \qquad (3.11)$$

where ε^p is the plastic strain tensor and **I** is the second-order unit tensor. When the void volume fraction reaches to the critical value f_c, void coalescence occurs. In this study, an arbitrary value, $f_c = 0.02$, is used for all the analyses. Tvergaard and Needleman introduced a function to simulate void coalescence:

$$f^* = \begin{cases} f & for \quad f \leq f_c \\ f_c + \frac{f_u^* - f_c}{f_F - f_c}(f - f_c) & for \quad f > f_c \end{cases} \qquad (3.12)$$

where $f^* = 1/q_1$. When the condition $f > f_c$ is satisfied, f^* replaces f in Eq. (3.12). As the void volume fraction increases to f_F, the element is assumed to lose load carrying capacity and cracks are expected to propagate. An empirical equation, $f_F = 0.2 + 2f_0$ [42], is considered in this study.

3.3.2 Simplification of the Lüders Plateau

In this study, a simplified version of Lüders Plateau in [5, 82] is utilized, by keeping the flow stress as a constant and equaling to the yield stress, see Fig. 3.12. Flow stress-strain curve of the matrix material is described by the following rule:

$$\sigma_f = \begin{cases} \sigma_0 & for \quad \overline{\varepsilon^p} \leq \varepsilon_L \\ \sigma_0(1 + \frac{\overline{\varepsilon^p} - \varepsilon_L}{\varepsilon_0})^n & for \quad \overline{\varepsilon^p} > \varepsilon_L \end{cases} \qquad (3.13)$$

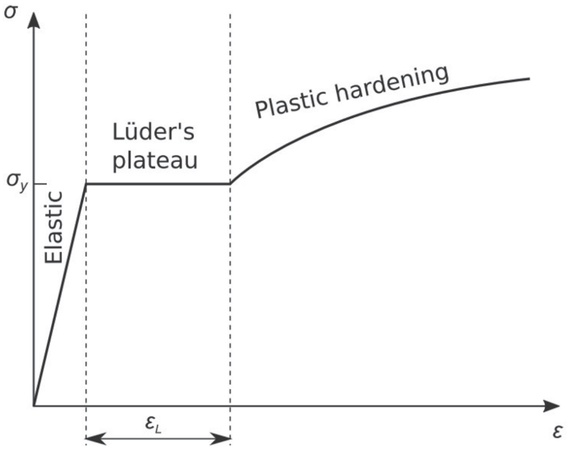

Figure 3.12: Illustration of the simplification of the Lüders Plateau.

where ε_L is the Lüders strain. When $\varepsilon_L = 0$, the matrix material returns to follow the power-law hardening rule. In this study, ε_L varied from 0 to infinite, considering two limiting cases: (1) materials without Lüders Plateau ($\varepsilon_L = 0$); (2) the perfectly plastic material $\varepsilon_L = infinite$.

3.3.3 Finite element model with SENT specimen

SENT specimens were chosen to study the effect of the Lüders plateau on ductile crack growth with *ABAQUS 6.12*. The geometry of the SENT specimen is schematically shown in Fig. 3.13. A fixed specimen width, $W = 50mm$, was used for all the analyses. Xu [87] and Østby [88, 88] found that the crack resistance curve depends significantly on the specimen width (Østby et al., 2007a, b; Xu et al., 2009). However, the specimen size effect was out of the scope of this study and will not be focused. The specimen length L is 10 times of the specimen width. a is the initial crack length. The crack depth effect is investigated by varying the ratio of the initial crack length to the specimen width, a/W.

Considering the symmetry of the problem, only one half of the specimen was modeled. 4-node reduced integration plane strain elements (CPE4R) were applied. Large deformation was accounted for all the analyses. A remote homogeneous displacement boundary condition was applied to induce crack propagation. The region with uniform mesh size, see Fig. 3.13 (b) and (c), was extended to 3.0 mm above the symmetric plane with mesh size of 0.1×0.1 mm, except two rows of elements with mesh size of 0.1×0.05 mm at the symmetric plane where the crack was supposed to propagate. The remaining part of the specimen was meshed with

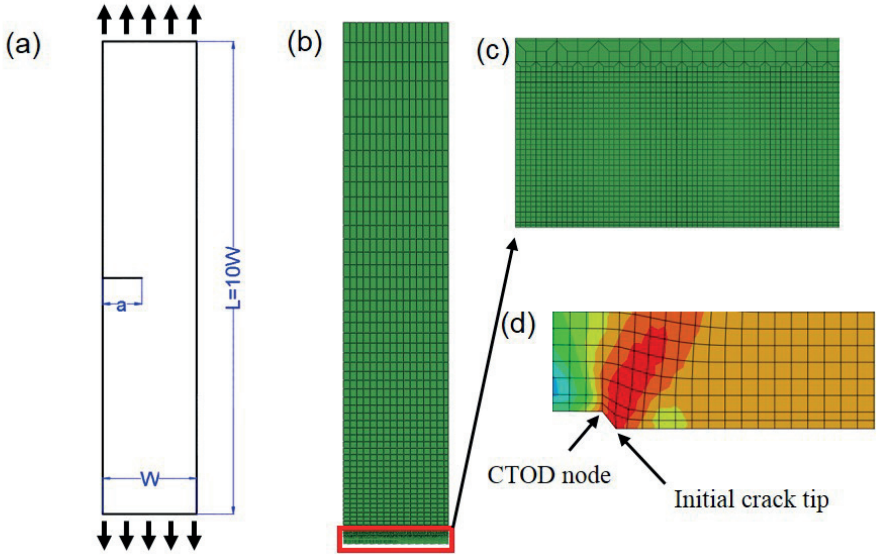

Figure 3.13: (a) SENT specimen; (b) Global mesh; (c) Local mesh; (d) Definition of CTOD node.

relative coarse elements, see Fig. 3.13 (b). When the void volume fraction reached f_F, the element failed and the crack extension was measured by multiplying the original element length (0.1 mm) with the failed element numbers. Corresponding CTOD was measured as 2 times of the displacement of the node neighbor to the initial crack tip, see Fig. 3.13 (d).

In this study, the effects of crack depth, strain hardening, initial void volume fraction coupled with the effect of Lüders plateau on the ductile crack growth resistance with SENT specimens were also discussed. The results were summarized and presented in Paper-V.

Chapter 4

Main findings of the PhD study

The main results about determining equivalent stress-strain curves with notched specimens, experimental investigation of low temperature effect on the ductility diagram, numerical study on the Lüders Plateau effect on ductile crack growth resistance derived from Chapter 3 are summarized briefly in this chapter.

4.1 Determining equivalent stress-strain curves with notched specimens

In this study, we identified a 'magic' notched tensile specimen. With a single correction factor, true stress-strain curves from this 'magic' notched specimen can be converted to material's equivalent stress-strain curve accurately. The correction factor was expressed as a function the strain corresponding to the maximum tensile load. However, this method is less accurate for the perfectly plastic material. Numerical analysis shows that the outer diameter should be 3.5 times larger than initial radius of the minimum cross section in order to use the special notched tensile specimen. For weldments, the initial radius of the minimum cross section is recommended to be smaller than material zone length in notch region. Meanwhile, we also proposed a correction function by performing a series of numerical analyses with axisymmetric notched tensile specimens. With the proposed correction function, the true stress-strain curve from 'any' axisymmetric notched tensile specimen can be converted to the material's equivalent stress-strain curve and no Bridgman correction is needed. Accordingly, a recommended procedure to determine the material's equivalent stress-strain curve with the axisymmetric notched tensile specimens was proposed. The proposed procedure can be applied to hardening materials, as well as the perfectly plastic material. It is worth noting that, the 'magic' notch and the proposed procedure can be used to both homogeneous material and inhomogeneous materials (such as the weldment), by locating the notch in the target material zone, under the geometric requirements ($d_0 \geq 3.5a_0, a_0 < H$).The proposed procedure is inexpensive and accurate, since the only information needed during the tensile test is the true stress-strain curve from the axisymmetric notched tensile specimen and the material's hardening exponent.

4.2 Low temperature effect on the ductility diagram

In this study, quasi-static tensile tests with smooth round bar and axisymmetric notched tensile specimens were performed to study the low temperature effect on the fracture locus of a 420 MPa structural steel (45 tests in total). Combined with a digital high-speed camera and a two-plane mirrors system, specimen deformation was recorded in two orthogonal planes. Pictures taken were then analyzed with the edge tracing method to calculate the minimum cross-section diameter reduction of the necked/notched specimen. Obvious temperature effect was observed on the load-strain curves for smooth and notched specimens. Both the strength and strain hardening characterized by the strain at maximum load increase with temperature decrease down to -60°C. Somewhat unexpected, the fracture strains (ductility) of both smooth and notched specimens at temperatures down to -60°C do not deteriorate, compared with those at room temperature. Combined with numerical analyses, it shows that the effect of low temperatures (down to -60°C) on fracture locus is insignificant.

4.3 Lüders Plateau effect on ductile crack growth resistance

In this study, we investigated the Lüders plateau effect on ductile crack growth with two-dimensional SENT specimens in plane strain condition. The Gurson damage model was used to simulate the crack growth. A family of Lüders plateau length has been studied. It has been observed that the existence of Lüders plateau does not influence the initiation toughness but alters material's ductile fracture resistance. The Lüders plateau effect on ductile crack resistance curve depends on the crack depth. It has also been found that the Lüders plateau effect is controlled by the stress triaxiality ahead of the crack tip. The Lüders plateau effect was also observed for material with smaller initial void volume fraction and the effect was more pronounced. For materials with Lüders plateau, both the effects of crack depth and strain hardening on crack resistance curve were reduced. The larger the Lüders plateau, the larger reduction.

Investigation on the Lüders plateau effect on crack driving force by Dahl have demonstrated that the existence of Lüders plateau intensified the crack driving force. Larger Lüders plateau corresponds to higher crack driving force [5]. Ductile crack growth lies in the competition of crack driving force and crack resistance. When the crack driving force is larger than material's crack resistance, ductile fracture proceeds; otherwise, fracture will be suppressed. Combining the results in [5] and in this study, the Lüders plateau on one side increases the crack driving force; on the other side it may reduce material's ductile crack resistance, depending on the plateau length, crack depth, material's toughness and strain hardening. Attention should be paid for the application of materials with Lüders plateau, especially in the Arctic region.

Chapter 5

Recommendations for Future Studies

5.1 Low temperature effect on the ductility diagram

For most studies on the temperature effect on the ductility diagram, axisymmetrical notched tensile bars were utilized. Correspondingly, the stress triaxility was relatively high. In the range of medium and negative stress triaxialities, the studies were rare. If any, they were performed at room temperature. In section 3.2, we studied the low temperature effect on ductility diagram with temperatures down to -60°C. However, much work can be done in this research topic:

1. Investigation of low temperature effect on ductility diagram with temperatures down to ductile-brittle transition temperatures.

2. Studies on the low temperature effect on the ductility diagram in the range of medium and negative stress triaxialities.

3. Investigation on the fracture mechanism in medium and negative stress triaxialities.

5.2 Lüders Plateau effect on fracture response

Low temperature induced Lüders Plateau may play an important role on crack driving force and crack growth resistance. In section 3.3, the Gurson damage model and the SENT specimen were used to investigate the effect of Lüders Plateau on ductile crack growth resistance. Here are some suggestions for the future studies:

1. Investigation on the effect of Lüders Plateau on fracture response for metallic materials with a more physically based model for the description of the plateau.
2. Investigation on the effect of Lüders Plateau on ductile and cleavage fracture with cohesive zone model.
3. Investigation on the effect of Lüders Plateau on crack driving force and crack growth resistance with pipelines subject to different stress states, such as tension, bending, with or without inner pressure.
4. Investigation on the effect of Lüders Plateau on ductile crack growth resistance with specimens under different constraint levels.

Bibliography

[1] D. L. Gautier, K. J. Bird, R. R. Charpentier, A. Grantz, D. W. Houseknecht, T. R. Klett, T. E. Moore, J. K. Pitman, C. J. Schenk, J. H. Schuenemeyer, *et al.*, “Assessment of undiscovered oil and gas in the arctic,” *Science*, vol. 324, no. 5931, pp. 1175–1179, 2009.

[2] Ø. Harsem, A. Eide, and K. Heen, “Factors influencing future oil and gas prospects in the arctic,” *Energy policy*, vol. 39, no. 12, pp. 8037–8045, 2011.

[3] G. Ermida, “Strategic decisions of international oil companies: Arctic versus other regions,” *Energy Strategy Reviews*, vol. 2, no. 3-4, pp. 265–272, 2014.

[4] G. La Rosa, A. Risitano, and G. Mirone, “Postnecking elastoplastic characterization: Degree of approximation in the bridgman method and properties of the flow-stress/true-stress ratio,” *Metallurgical and Materials Transactions A*, vol. 34, pp. 615–624, Mar 2003.

[5] B. Dahl, X. Ren, O. Akselsen, B. Nyhus, and Z. Zhang, “Effect of low temperature tensile properties on crack driving force for arctic applications,” *Theoretical and Applied Fracture Mechanics*, vol. 93, pp. 88–96, 2018.

[6] X. Poulain, L. Kohlman, W. Binienda, G. Roberts, R. Goldberg, and A. Benzerga, “Determination of the intrinsic behavior of polymers using digital image correlation combined with video-monitored testing,” *International Journal of Solids and Structures*, vol. 50, no. 11-12, pp. 1869–1878, 2013.

[7] M. Jerabek, Z. Major, and R. Lang, “Strain determination of polymeric materials using digital image correlation,” *Polymer Testing*, vol. 29, no. 3, pp. 407–416, 2010.

[8] F. Grytten, H. Daiyan, M. Polanco-Loria, and S. Dumoulin, “Use of digital image correlation to measure large-strain tensile properties of ductile thermoplastics,” *Polymer Testing*, vol. 28, no. 6, pp. 653–660, 2009.

[9] P. Knysh and Y. P. Korkolis, “Identification of the post-necking hardening response of rate-and temperature-dependent metals,” *International Journal of Solids and Structures*, vol. 115, pp. 149–160, 2017.

[10] P. W. Bridgman, *Studies in large plastic flow and fracture*, vol. 177. McGraw-Hill New York, 1952.

[11] M. Gromada, G. Mishuris, and A. Öchsner, *Correction formulae for the stress distribution in round tensile specimens at neck presence*. Springer Science & Business Media, 2011.

[12] W. Davidenkov, “Mechanical methods of testing analysis of the state of stress in the neck of a tension specimen,” in *Proc. ASTM*, 1946.

[13] E. Siebel and S. Schwaigere, “Mechanics of tensile test,” *Arch Eisenhuttenwes*, vol. 19, pp. 145–152, 1948.

[14] G. Le Roy, J. Embury, G. Edwards, and M. Ashby, “A model of ductile fracture based on the nucleation and growth of voids,” *Acta Metallurgica*, vol. 29, no. 8, pp. 1509–1522, 1981.

[15] Y. Bao, “Dependence of ductile crack formation in tensile tests on stress triaxiality, stress and strain ratios,” *Engineering fracture mechanics*, vol. 72, no. 4, pp. 505–522, 2005.

[16] G. Mirone, “A new model for the elastoplastic characterization and the stress–strain determination on the necking section of a tensile specimen,” *International Journal of Solids and Structures*, vol. 41, no. 13, pp. 3545 – 3564, 2004.

[17] G. Mirone and D. Corallo, “A local viewpoint for evaluating the influence of stress triaxiality and lode angle on ductile failure and hardening,” *International Journal of Plasticity*, vol. 26, no. 3, pp. 348 – 371, 2010.

[18] K. Zhano and Z. Li, “Numerical analysis of the stress-strain curve and fracture initiation for ductile material,” *Engineering fracture mechanics*, vol. 49, no. 2, pp. 235–241, 1994.

[19] J. Peirs, P. Verleysen, W. Van Paepegem, and J. Degrieck, “Determining the stress–strain behaviour at large strains from high strain rate tensile and shear

experiments," *International Journal of Impact Engineering*, vol. 38, no. 5, pp. 406–415, 2011.

[20] J. Kajberg and G. Lindkvist, "Characterisation of materials subjected to large strains by inverse modelling based on in-plane displacement fields," *International Journal of Solids and Structures*, vol. 41, no. 13, pp. 3439–3459, 2004.

[21] Y. Ling, "Uniaxial true stress-strain after necking," *AMP Journal of Technology*, vol. 5, no. June, pp. 37–48, 1996.

[22] Z. Zhang, M. Hauge, J. Ødegård, and C. Thaulow, "Determining material true stress–strain curve from tensile specimens with rectangular cross-section," *International Journal of Solids and Structures*, vol. 36, no. 23, pp. 3497–3516, 1999.

[23] Z. Zhang, J. Ødegård, O. Søvik, and C. Thaulow, "A study on determining true stress–strain curve for anisotropic materials with rectangular tensile bars," *International Journal of Solids and Structures*, vol. 38, no. 26-27, pp. 4489–4505, 2001.

[24] Z. Zhang, J. Ødegård, and O. Søvik, "Determining true stress–strain curve for isotropic and anisotropic materials with rectangular tensile bars: method and verifications," *Computational materials science*, vol. 20, no. 1, pp. 77–85, 2001.

[25] J. Choung and S. Cho, "Study on true stress correction from tensile tests," *Journal of Mechanical Science and Technology*, vol. 22, no. 6, pp. 1039–1051, 2008.

[26] J. Choung, "Comparative studies of fracture models for marine structural steels," *Ocean Engineering*, vol. 36, no. 15-16, pp. 1164–1174, 2009.

[27] I. Scheider, W. Brocks, and A. Cornec, "Procedure for the determination of true stress-strain curves from tensile tests with rectangular cross-section specimens," *Journal of engineering materials and technology*, vol. 126, no. 1, pp. 70–76, 2004.

[28] Z. Zhang, M. Hauge, C. Thaulow, and J. Ødegård, "A notched cross weld tensile testing method for determining true stress–strain curves for weldments," *Engineering fracture mechanics*, vol. 69, no. 3, pp. 353–366, 2002.

[29] F. A. McClintock, "A criterion for ductile fracture by the growth of holes," *Journal of applied mechanics*, vol. 35, no. 2, pp. 363–371, 1968.

[30] J. Rice and D. Tracey, "On the ductile enlargement of voids in triaxial stress fields," *Journal of the Mechanics and Physics of Solids*, vol. 17, no. 3, pp. 201 – 217, 1969.

[31] J. Sun, Z.-J. Deng, and M.-J. Tu, "Effect of stress triaxiality levels in crack tip regions on the characteristics of void growth and fracture criteria," *Engineering fracture mechanics*, vol. 39, no. 6, pp. 1051–1060, 1991.

[32] M. Oyane, T. Sato, K. Okimoto, and S. Shima, "Criteria for ductile fracture and their applications," *Journal of Mechanical Working Technology*, vol. 4, no. 1, pp. 65 – 81, 1980.

[33] G. L. Roy, J. Embury, G. Edwards, and M. Ashby, "A model of ductile fracture based on the nucleation and growth of voids," *Acta Metallurgica*, vol. 29, no. 8, pp. 1509 – 1522, 1981.

[34] J. Sun, Z.-J. Deng, and M.-J. Tu, "Effect of stress triaxiality levels in crack tip regions on the characteristics of void growth and fracture criteria," *Engineering Fracture Mechanics*, vol. 39, no. 6, pp. 1051 – 1060, 1991.

[35] G. L. Rosa, G. Mirone, and A. Risitano, "Effect of stress triaxiality corrected plastic flow on ductile damage evolution in the framework of continuum damage mechanics," *Engineering Fracture Mechanics*, vol. 68, no. 4, pp. 417 – 434, 2001.

[36] A. S. Kao, H. A. Kuhn, O. Richmond, and W. A. Spitzig, "Tensile fracture and fractographic analysis of 1045 spheroidized steel under hydrostatic pressure," *Journal of Materials Research*, vol. 5, no. 1, p. 83–91, 1990.

[37] G. R. Johnson and W. H. Cook, "Fracture characteristics of three metals subjected to various strains, strain rates, temperatures and pressures," *Engineering fracture mechanics*, vol. 21, no. 1, pp. 31–48, 1985.

[38] J. Peng, P. Wu, Y. Huang, X. Chen, D. Lloyd, J. Embury, and K. Neale, "Effects of superimposed hydrostatic pressure on fracture in round bars under tension," *International Journal of Solids and Structures*, vol. 46, no. 20, pp. 3741–3749, 2009.

[39] P. Wu, X. Chen, D. Lloyd, and J. Embury, "Effects of superimposed hydrostatic pressure on fracture in sheet metals under tension," *International Journal of Mechanical Sciences*, vol. 52, no. 2, pp. 236–244, 2010.

[40] M. Alves and N. Jones, "Influence of hydrostatic stress on failure of axisymmetric notched specimens," *Journal of the Mechanics and Physics of Solids*, vol. 47, no. 3, pp. 643–667, 1999.

[41] K. Han, J. Shuai, X. Deng, L. Kong, X. Zhao, and M. Sutton, “The effect of constraint on ctod fracture toughness of api x65 steel,” *Engineering Fracture Mechanics*, vol. 124, pp. 167–181, 2014.

[42] J. Xu, Z. Zhang, E. Østby, B. Nyhus, and D. Sun, “Constraint effect on the ductile crack growth resistance of circumferentially cracked pipes,” *Engineering Fracture Mechanics*, vol. 77, no. 4, pp. 671–684, 2010.

[43] Z. Zhang and E. Niemi, “Studies on the ductility predictions by different local failure criteria,” *Engineering Fracture Mechanics*, vol. 48, no. 4, pp. 529–540, 1994.

[44] G. Mirone, “Role of stress triaxiality in elastoplastic characterization and ductile failure prediction,” *Engineering Fracture Mechanics*, vol. 74, no. 8, pp. 1203–1221, 2007.

[45] T. Børvik, O. Hopperstad, and T. Berstad, “On the influence of stress triaxiality and strain rate on the behaviour of a structural steel. part ii. numerical study,” *European Journal of Mechanics-A/Solids*, vol. 22, no. 1, pp. 15–32, 2003.

[46] O. Hopperstad, T. Børvik, M. Langseth, K. Labibes, and C. Albertini, “On the influence of stress triaxiality and strain rate on the behaviour of a structural steel. part i. experiments,” *European Journal of Mechanics-A/Solids*, vol. 22, no. 1, pp. 1–13, 2003.

[47] G. Mirone and D. Corallo, “A local viewpoint for evaluating the influence of stress triaxiality and lode angle on ductile failure and hardening,” *International Journal of Plasticity*, vol. 26, no. 3, pp. 348–371, 2010.

[48] Y. Bao and T. Wierzbicki, “On fracture locus in the equivalent strain and stress triaxiality space,” *International Journal of Mechanical Sciences*, vol. 46, no. 1, pp. 81–98, 2004.

[49] Z. Zhang, J. édegAard, and C. Thaulow, “Characterization of material ductility by microvoid nucleation parameters,” in *Proceeding of the 19th Risù International Symposium on material science: Modelling of structure and mechnaics of materials from microscale to product, Risù, Denmark*, 1998.

[50] Z. Zhang and M. Hauge, “On the gurson micro-mechanical parameters,” in *Fatigue and Fracture Mechanics: 29th Volume*, ASTM International, 1999.

[51] T. Wierzbicki, Y. Bao, Y.-W. Lee, and Y. Bai, “Calibration and evaluation of seven fracture models,” *International Journal of Mechanical Sciences*, vol. 47, no. 4-5, pp. 719–743, 2005.

[52] L. Xue, “Damage accumulation and fracture initiation in uncracked ductile solids subject to triaxial loading,” *International journal of solids and structures*, vol. 44, no. 16, pp. 5163–5181, 2007.

[53] T. Wierzbicki and L. Xue, “On the effect of the third invariant of the stress deviator on ductile fracture,” *Impact and Crashworthiness Laboratory, Technical Report*, vol. 136, 2005.

[54] M. Wilkins, R. Streit, and J. Reaugh, “Cumulative-strain-damage model of ductile fracture: simulation and prediction of engineering fracture tests,” tech. rep., Lawrence Livermore National Lab., CA (USA); Science Applications, Inc., San Leandro, CA (USA), 1980.

[55] F. McClintock, “A criterion for ductile fracture by growth of holes,” *Applied Mech*, pp. 363–371.

[56] J. Bardet, “Lode dependences for isotropic pressure-sensitive elastoplastic materials,” *Journal of applied mechanics*, vol. 57, no. 3, pp. 498–506, 1990.

[57] Y. Lou, H. Huh, S. Lim, and K. Pack, “New ductile fracture criterion for prediction of fracture forming limit diagrams of sheet metals,” *International Journal of Solids and Structures*, vol. 49, no. 25, pp. 3605–3615, 2012.

[58] Z. Marciniak, K. Kuczyński, and T. Pokora, “Influence of the plastic properties of a material on the forming limit diagram for sheet metal in tension,” *International Journal of Mechanical Sciences*, vol. 15, no. 10, pp. 789–800, 1973.

[59] M. Brünig, S. Gerke, and V. Hagenbrock, “Micro-mechanical studies on the effect of the stress triaxiality and the lode parameter on ductile damage,” *International Journal of Plasticity*, vol. 50, pp. 49–65, 2013.

[60] I. Barsoum and J. Faleskog, “Micromechanical analysis on the influence of the lode parameter on void growth and coalescence,” *International Journal of Solids and Structures*, vol. 48, no. 6, pp. 925–938, 2011.

[61] Y. Lou and H. Huh, “Extension of a shear-controlled ductile fracture model considering the stress triaxiality and the lode parameter,” *International Journal of Solids and Structures*, vol. 50, no. 2, pp. 447–455, 2013.

[62] M. Dunand and D. Mohr, “Effect of lode parameter on plastic flow localization after proportional loading at low stress triaxialities,” *Journal of the Mechanics and Physics of Solids*, vol. 66, pp. 133–153, 2014.

[63] Y. Lou and H. Huh, “Evaluation of ductile fracture criteria in a general three-dimensional stress state considering the stress triaxiality and the lode parameter,” *Acta Mechanica Solida Sinica*, vol. 26, no. 6, pp. 642–658, 2013.

[64] Y. Bai and T. Wierzbicki, “A new model of metal plasticity and fracture with pressure and lode dependence,” *International journal of plasticity*, vol. 24, no. 6, pp. 1071–1096, 2008.

[65] Y. Bai, X. Teng, and T. Wierzbicki, “On the application of stress triaxiality formula for plane strain fracture testing,” *Journal of Engineering Materials and technology*, vol. 131, no. 2, p. 021002, 2009.

[66] S. Basu and A. A. Benzerga, “On the path-dependence of the fracture locus in ductile materials: Experiments,” *International Journal of Solids and Structures*, vol. 71, pp. 79–90, 2015.

[67] A. Benzerga, D. Surovik, and S. Keralavarma, “On the path-dependence of the fracture locus in ductile materials–analysis,” *International Journal of Plasticity*, vol. 37, pp. 157–170, 2012.

[68] L. E. B. Dæhli, T. Børvik, and O. S. Hopperstad, “Influence of loading path on ductile fracture of tensile specimens made from aluminium alloys,” *International Journal of Solids and Structures*, vol. 88, pp. 17–34, 2016.

[69] N. Thomas, S. Basu, and A. A. Benzerga, “On fracture loci of ductile materials under non-proportional loading,” *International Journal of Mechanical Sciences*, vol. 117, pp. 135–151, 2016.

[70] H. Yu, J. S. Olsen, J. He, and Z. Zhang, “Effects of loading path on the fracture loci in a 3d space,” *Engineering Fracture Mechanics*, vol. 151, pp. 22–36, 2016.

[71] T. Børvik, O. Hopperstad, S. Dey, E. Pizzinato, M. Langseth, and C. Albertini, “Strength and ductility of weldox 460 e steel at high strain rates, elevated temperatures and various stress triaxialities,” *Engineering fracture mechanics*, vol. 72, no. 7, pp. 1071–1087, 2005.

[72] U. Lindholm, A. Nagy, G. Johnson, and J. Hoegfeldt, “Large strain, high strain rate testing of copper,” *Journal of engineering materials and technology*, vol. 102, no. 4, pp. 376–381, 1980.

[73] G. Johnson, “Dynamic analysis of a torsion test specimen including heat conduction and plastic flow,” *Journal of engineering materials and technology*, vol. 103, no. 3, pp. 201–206, 1981.

[74] M. J. Haynes and R. P. Gangloff, "Elevated temperature fracture toughness of al-cu-mg-ag sheet: Characterization and modeling," *Metallurgical and Materials Transactions A*, vol. 28, no. 9, pp. 1815–1829, 1997.

[75] Y. Liu, S. Kyriakides, and J. F. Hallai, "Reeling of pipe with lüders bands," *International Journal of Solids and Structures*, vol. 72, pp. 11–25, 2015.

[76] J. F. Hallai and S. Kyriakides, "Underlying material response for lüders-like instabilities," *International Journal of Plasticity*, vol. 47, pp. 1–12, 2013.

[77] M. Mazière, C. Luis, A. Marais, S. Forest, and M. Gaspérini, "Experimental and numerical analysis of the lüders phenomenon in simple shear," *International Journal of Solids and Structures*, vol. 106, pp. 305–314, 2017.

[78] D. Beardsmore, J. Q. da Fonseca, J. Romero, C. English, S. Ortner, J. Sharples, A. Sherry, and M. Wilkes, "Study of lüders phenomena in reactor pressure vessel steels," *Materials Science and Engineering: A*, vol. 588, pp. 151–166, 2013.

[79] J. Han, C. Lu, B. Wu, J. Li, H. Li, Y. Lu, and Q. Gao, "Innovative analysis of luders band behaviour in x80 pipeline steel," *Materials Science and Engineering: A*, vol. 683, pp. 123–128, 2017.

[80] X. Ren, H. O. Nordhagen, Z. Zhang, O. M. Akselsen, *et al.*, "Tensile properties of 420 mpa steel at low temperature," in *The Twenty-fifth International Ocean and Polar Engineering Conference*, International Society of Offshore and Polar Engineers, 2015.

[81] N. Tsuchida, Y. Tomota, K. Nagai, and K. Fukaura, "A simple relationship between lüders elongation and work-hardening rate at lower yield stress," *Scripta Materialia*, vol. 54, no. 1, pp. 57–60, 2006.

[82] N. Nourpanah and F. Taheri, "Effect of lüders plateau on fracture response and toughness of pipelines subject to extreme plastic bending," *Journal of Pressure Vessel Technology*, vol. 133, no. 5, p. 051701, 2011.

[83] A. L. Gurson, "Continuum theory of ductile rupture by void nucleation and growth: Part i—yield criteria and flow rules for porous ductile media," *Journal of engineering materials and technology*, vol. 99, no. 1, pp. 2–15, 1977.

[84] V. Tvergaard, "Influence of voids on shear band instabilities under plane strain conditions," *International Journal of fracture*, vol. 17, no. 4, pp. 389–407, 1981.

[85] V. Tvergaard, “On localization in ductile materials containing spherical voids,” *International Journal of fracture*, vol. 18, no. 4, pp. 237–252, 1982.

[86] V. Tvergaard and A. Needleman, “Analysis of the cup-cone fracture in a round tensile bar,” *Acta metallurgica*, vol. 32, no. 1, pp. 157–169, 1984.

[87] J. Xu, Z. Zhang, E. Østby, B. Nyhus, and D. Sun, “Effects of crack depth and specimen size on ductile crack growth of sent and senb specimens for fracture mechanics evaluation of pipeline steels,” *International Journal of Pressure Vessels and Piping*, vol. 86, no. 12, pp. 787–797, 2009.

[88] E. Østby, C. Thaulow, and Z. Zhang, “Numerical simulations of specimen size and mismatch effects in ductile crack growth–part i: Tearing resistance and crack growth paths,” *Engineering fracture mechanics*, vol. 74, no. 11, pp. 1770–1792, 2007.

Appendix A

Appended papers

A.1

A special notched tensile specimen to determine the flow stress-strain curve of hardening materials without applying the Bridgman correction

Authors: Shengwen Tu; Xiaobo Ren; Bård Nyhus; Odd Magne Akselsen; Jianying He; Zhiliang Zhang

Engineering Fracture Mechanics. 179 (2017), 225-239

Engineering Fracture Mechanics 179 (2017) 225–239

Contents lists available at ScienceDirect

Engineering Fracture Mechanics

journal homepage: www.elsevier.com/locate/engfracmech

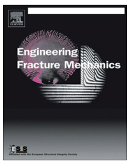

A special notched tensile specimen to determine the flow stress-strain curve of hardening materials without applying the Bridgman correction

Shengwen Tu [a], Xiaobo Ren [b], Bård Nyhus [b], Odd Magne Akselsen [b], Jianying He [a], Zhiliang Zhang [a,*]

[a] Department of Structural Engineering, Norwegian University of Science and Technology, Trondheim 7491, Norway
[b] SINTEF Materials and Chemistry, Trondheim 7456, Norway

ARTICLE INFO

Article history:
Received 12 March 2017
Received in revised form 19 April 2017
Accepted 23 April 2017
Available online 25 April 2017

Keywords:
Flow stress-stain curve
Notched tensile specimen
True stress-strain curve
Weldment
Bridgman correction

ABSTRACT

Structural integrity assessment of weldments requires the input of flow stress-strain curve of each individual material zone. To cope with these challenges, a cylindrical cross weld tensile specimen with a notch located either in the weld metal, base metal or possibly heat affected zone has been previously developed by the authors to determine the true stress-strain curve for the material zone of interest. The disadvantage of this notched tensile testing method as well as the standard tensile testing method using a smooth specimen, is that the well-known Bridgman correction still has to be applied in order to obtain material's equivalent or flow stress-strain curves. In this study, tensile specimens with various notch geometries have been scrutinized and a 'magic' specimen with a special notch geometry has been identified. By using this special notched tensile specimen, material's flow stress-strain curve can be directly calculated from the recorded load versus diameter reduction curve and no Bridgman correction is needed. The method is very accurate for power-law hardening materials and becomes less accurate for materials with significant Lüders plateau in the initial yield region.

1. Introduction

Material's flow stress-strain curve governs the plastic behaviour, and structural integrity assessment of weldments using finite element method requires the input of flow stress-strain curve of each individual material zone. Smooth specimens with circular or rectangular cross section are widely used for determining the true stress-strain curves of base material, weld metal or heat affected zone, and materials' flow stress-strain curves can be derived from the true stress-strain curves. For standard smooth tensile specimens, necking happens along with localized deformation on the specimen, accompanied by the occurrence of tri-axial stress state in the localized region. The true stress calculated from the load divided by current area of the minimum cross section would be inaccurate to represent the material's equivalent stress due to the existence of tri-axial stress state in the localized region. Based on a stress state analysis in the localized region, Bridgman [1] proposed a correction method that links to the ratio of a/R, a is the current radius of the minimum cross section and R is the current notch radius. Simple finite element analysis of smooth tensile specimens [2] shows that with the Bridgman correction, the

---

[*] Corresponding author.
E-mail address: zhiliang.zhang@ntnu.no (Z. Zhang).

http://dx.doi.org/10.1016/j.engfracmech.2017.04.039
0013-7944/

Nomenclature

a	current minimum cross section radius
a_0	initial minimum cross section radius
$D = 2a_0$	initial minimum cross section diameter
d_0	initial outer diameter of notched tensile specimen
E	Young's modulus
G	notch geometry correction factor
G^m	magic notch correction factor
H	weld zone length in the notched region
L	specimen length
n	material hardening exponent
P	global load
R_0	initial notch radius
R	current notch radius
v	Poisson's ratio
ε_0	yield strain
ε	average true strain
ε_L	Lüders plateau strain
$\overline{\varepsilon^p}$	equivalent plastic strain
$\Delta\sigma$	absolute stress error
σ_0	yield stress
$\overline{\sigma}$	material's flow stress
$\sigma_{e,notch}$	engineering stress of a notched tensile specimen
σ_{eq}	Mises equivalent stress
σ_T	true stress of a smooth tensile specimen
$\sigma_{T,notch}$	true stress of a notched tensile specimen
σ_T^G	G corrected true stress for notched tensile specimen

Bridgman corrected stress-strain curve differs to material's equivalent stress-strain curve input for the numerical analysis when strain is large. La Rosa and Risitano [2] applied the Bridgman correction to different steels, C40, FE36, AISI304, D98, etc., and found that with the increase of strain the error $\Delta\sigma$ between the material equivalent stress and the Bridgman corrected stress for steel D98 would be as large as 10.6% at the strain $\varepsilon = 1.35$ (Fig. 1). The assumption used in the Bridgman correction method is that the distribution of equivalent strain and equivalent stress is uniform over the minimum cross section [1]. However, previous finite element analyses [3–7] indicate that this may not be true. In practice, the application of the Bridgman correction is also not trivial because one has to measure the current radius of the minimum cross section and the current notch radius simultaneously. Le Roy [8] proposed a function for estimating the a/R without paying attention to the material properties. Correction methods have also been proposed for rectangular cross section specimens [9–12]. Ling [13] proposed a method based on extrapolation of the true stress-strain curve before necking. However, this approximation is not suitable for the case when the strain is large.

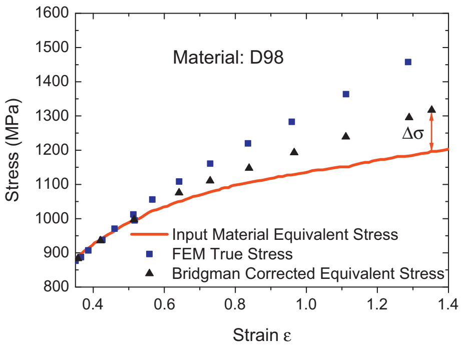

Fig. 1. Comparison between input material equivalent stress and Bridgman corrected true stress [2]. FEM true stress is calculated by dividing load by current minimum cross section area.

For weldments, it is an even more challenging task to characterize the material mechanical properties since the outcome of a conventional cross weld tensile test strongly depends on the unpredictable location of fracture. Zhang et al. [14] proposed a notched tensile specimen for determining the true stress-strain curve of each individual material zone in a weldment. By introducing a notch on a smooth round bar, the deformation of the notched tensile specimen is constrained into a small region under tensile loading. Based on the load separation principle, a so-called notch geometry factor *G* is introduced to convert the true stress from a notched specimen to the corresponding true stress of a smooth specimen. The *G* factor depends on the material hardening exponent and ratio of the initial diameter of the minimum cross section to the initial notch radius. Numerical analysis shows that the method proposed in [14] provides good result when the strain is relatively small. As the strain increases, large difference between the true stress-strain curve obtained from a notched specimen by using the *G* factor and the material's equivalent stress-strain curve emerges.

In this study, numerical analyses have been conducted with different initial notch geometries and material hardening exponents to explore the existence of a special notch configuration such that the resulting stress-strain curve corrected by a single factor agrees with the material equivalent stress-strain curve even for the case when the strain is large. A special notched tensile specimen has indeed been identified which can output material's flow stress-strain curve directly and the Bridgman correction is not needed. The special notched tensile specimen can be applied to both homogeneous materials and weldments.

The paper consists of following sections. The definition of various stresses used in the notched tensile specimens and numerical procedure used in the study are briefly introduced in Section 2. Section 3 identifies the 'magic' notch geometry and explains why this special notch geometry can determine the material's equivalent/flow stress strain curve directly. The application of the 'magic' notched tensile testing method to weldments is presented in Section 4. Various parameters relevant to a weldment are discussed and limitation of the method to materials with significant Lüders plateau is also mentioned. A recommended procedure to determine material's flow stress-strain curve for each material zone of a weldment is presented in Section 5. The paper is concluded by a summary of the main results in Section 6.

2. Definition of notch stresses and numerical procedure

Notched tensile specimen with round cross section is widely used for fatigue analysis [15–17], stress concentration analysis [18] and fracture locus measurement at relatively high stress triaxiality [19–21]. The geometry of notched specimen used in this study is described in Fig. 2. For a notched tensile specimen, the average true strain can be calculated by the area reduction of the minimum cross section:

$$\varepsilon = 2 * \ln\left(\frac{a_0}{a}\right) \tag{1}$$

where ε is the average true strain; a_0 and a are the initial and current radius of the minimum cross section, respectively. The engineering stress of a notched tensile specimen $\sigma_{e,notch}$ is calculated by dividing the load by the initial area of the minimum cross section, and the true stress $\sigma_{T,notch}$ for a notched tensile specimen can be calculated by dividing the load by the current area of the minimum cross section:

$$\sigma_{e,notch} = \frac{P}{\pi a_0^2} \tag{2}$$

$$\sigma_{T,notch} = \frac{P}{\pi a^2} \tag{3}$$

where *P* is the load. For a power-law hardening material, the strain at the maximum load of both smooth and notched tensile specimens is equal to the hardening exponent [14]. The true stress-strain curve corresponding to a smooth specimen, σ_T, can be obtained from a notched tensile specimen by dividing $\sigma_{T,notch}$ by the *G* factor, which is dependent on a_0/R_0, the hardening exponent and is independent of strain. For a given notched tensile specimen, the value of the *G* factor [14] is defined as the ratio of the true stress of a notched specimen to the true stress of a smooth specimen at the strain equal to material's hardening exponent, Eq. (4).

$$G = \left.\frac{\sigma_{T,notch}}{\sigma_T}\right|_{\varepsilon=n} \tag{4}$$

In this study, a series of notched tensile specimens with different material properties and notch geometries have been analysed with ABAQUS 6.14 to identify the special notch geometry. Unless otherwise specified, the flow stress-strain curves of the materials analysed assume to follow a power-law hardening rule:

$$\bar{\sigma} = \sigma_0\left(1 + \frac{\overline{\varepsilon^p}}{\varepsilon_0}\right)^n \tag{5}$$

where $\bar{\sigma}$, $\overline{\varepsilon^p}$, σ_0, $\varepsilon_0 = \sigma_0/E$, n are the flow stress, equivalent plastic strain, yield stress, yield strain and hardening exponent, respectively. In this study, $\sigma_0 = 400$ MPa, $n = 0.1, 0.15, 0.2$, Young's modulus $E = 200$ GPa, and Poisson's ratio $v = 0.3$ have

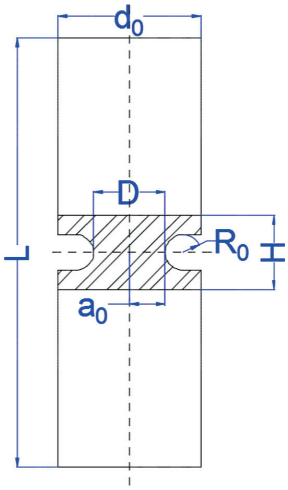

Fig. 2. Geometry of a notched tensile specimen.

been used. For all the notched tensile specimens in numerical procedure, $a_0 = 6$ and $d_0 = 24$ mm are used. Axisymmetric models with $a_0/R_0 = 1, 1.5, 2, 3$ have been analysed. Element type CAX4R is used considering larger deformation. In order to well capture the deformed notch shape, 60 elements in total are used in the notch profile and 20 elements with average size of 0.3×0.05 mm are used in the region close to the minimum cross section. The mesh of the notched tensile specimen with $a_0/R_0 = 3$ is shown in Fig. 3. The specimen is loaded under displacement control.

3. The 'magic' notched tensile testing specimen

3.1. Identification of the special notch geometry

The engineering stress-strain ($\sigma_{e,notch} - \varepsilon$) curves for the notched specimens are presented in Fig. 4. As expected, the $\sigma_{e,notch} - \varepsilon$ curves drop down after the peak load. For the same material, smaller notch (larger a_0/R_0) will result in higher engineering stress at the same strain level. Naturally, for a given notch configuration, material with higher hardening will yield higher maximum engineering stress at $\varepsilon = n$. It should be noted that the strain corresponding to the maximum load is equal to the hardening exponent for each material shown in Fig. 4 and is independent of the initial notch geometry [14]. The true

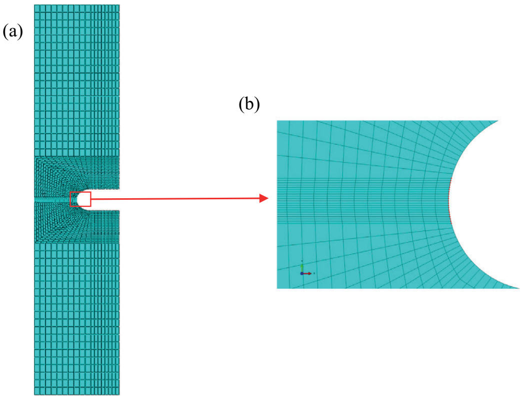

Fig. 3. Mesh of the notched tensile specimen with $a_0/R_0 = 3$: (a) global mesh, (b) local mesh.

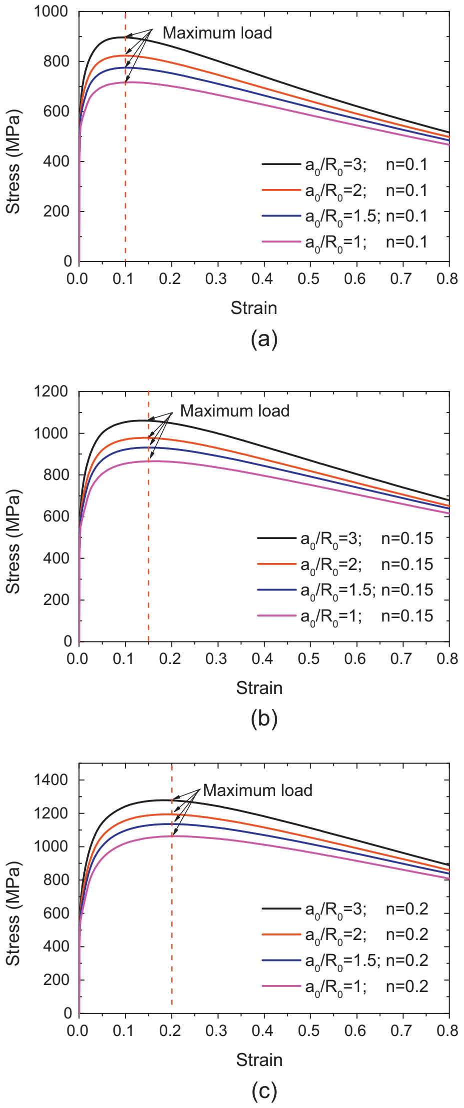

Fig. 4. $\sigma_{e,notch} - \varepsilon$ curves for the materials: (a) n = 0.1, (b) n = 0.15, (c) n = 0.2.

stress-strain curves ($\sigma_{T,notch} - \varepsilon$) for the notched tensile specimens are shown in Fig. 5. These curves are then individually corrected by the *G* factor defined in Eq. (4) and converted to flow stress-strain curves by subtracting the elastic strain, Eq. (6). Results of the *G* corrected flow stress-strain curves are compared in Fig. 6. The parameters involved in the *G* correction for different materials and notch geometries are listed in Table 1.

$$\overline{\varepsilon^p} = \varepsilon - \frac{\sigma_T^G}{E} \tag{6}$$

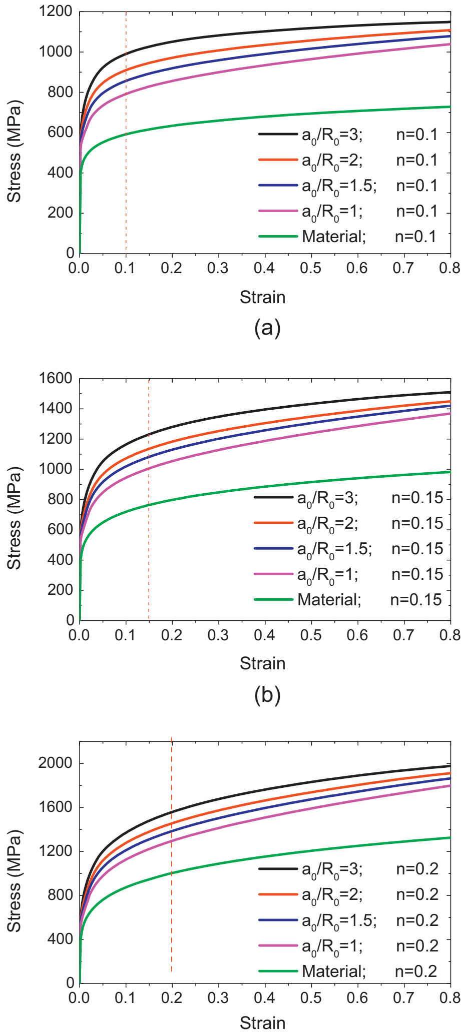

(a)

(b)

(c)

Fig. 5. $\sigma_{T,notch} - \varepsilon$ curves for the materials: (a) n = 0.1, (b) n = 0.15, (c) n = 0.2. The equivalent stress-strain curves of each material input for the analyses are also shown and denoted as green colour. (For interpretation of the references to colour in this figure legend, the reader is referred to the web version of this article.)

In the following, the G corrected flow stress-strain curve will be understood as the corrected flow stress-strain curve, unless otherwise stated. In Fig. 6, it can be observed that the corrected flow stress-strain curve agrees well with the material flow stress-strain curve when $\overline{\varepsilon^p} \leqslant n$ for all materials analysed. Difference between the corrected flow stress-strain curve and material's flow stress-strain curve input for the analysis appears and increases with the increase of equivalent plastic strain. For the specimen with $a_0/R_0 = 2$, the corrected flow stress-strain curves show good agreement with material's flow stress-strain curves with absolute errors at equivalent plastic strain $\overline{\varepsilon^p} = 0.8$ approaching to 1.4%, 0.8%, 0.7% for $n = 0.1, 0.15, 0.2$, respectively. Compared with other notch configurations, the specimens with $a_0/R_0 = 2$ yield smallest errors in Table 1.

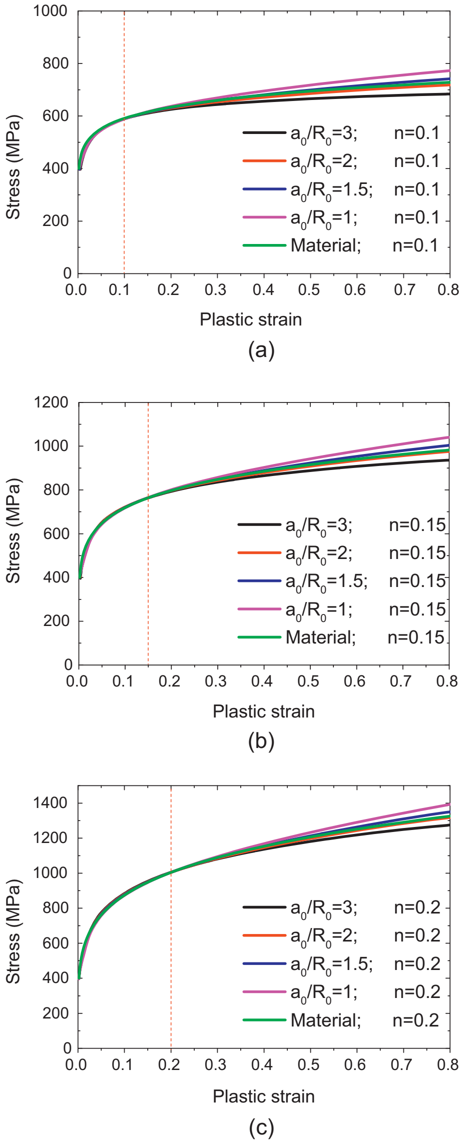

Fig. 6. G corrected flow stress-strain curves for the materials: (a) n = 0.1, (b) n = 0.15, (c) n = 0.2. Material's flow stress-strain curves input for the analyses are denoted as green colour.

Further studies with the same notch geometry $a_0/R_0 = 2$ but different hardening exponent $n = 0.05$, 0.075, 0.125 and 0.175 have been carried out to explore the feasibility of the special notch geometry. The results of corrected flow stress-strain curves are compared in Fig. 7. It can be seen that the corrected flow stress-strain curve overlaps with the material flow stress-strain curve in a large range of equivalent plastic strain for all the materials considered.

Hardening exponents varying from 0.05 to 0.2 in Figs. 6 and 7 cover a wide range of engineering materials obeying the power-law hardening rule. Error analysis in Table 1 shows that the notched tensile specimens with $a_0/R_0 = 2$ yield very

Table 1
Parameters for correcting flow stress-strain curves with the G factor.

	$\frac{a_0}{R_0}$	$\sigma_T\vert_{\varepsilon=n}$ MPa	$\sigma_{T,notch}\vert_{\varepsilon=n}$ MPa	G	$\frac{\vert\Delta\sigma\vert}{\bar{\sigma}}\Big\vert_{\overline{\varepsilon^p}=0.8}$ %
$n = 0.1$	3	590	991.11	1.6798	6.0
	2		909.72	1.5419	**1.4**
	1.5		857.86	1.454	1.9
	1		793	1.344	6.2
$n = 0.15$	3	764.46	1233	1.6129	4.7
	2		1135.17	1.4849	**0.8**
	1.5		1081.39	1.4146	2.1
	1		1005.5	1.3153	5.8
$n = 0.2$	3	1006.24	1560.86	1.5512	3.9
	2		1460.5	1.4514	**0.7**
	1.5		1389.19	1.3806	1.9
	1		1299.4	1.2913	5.1

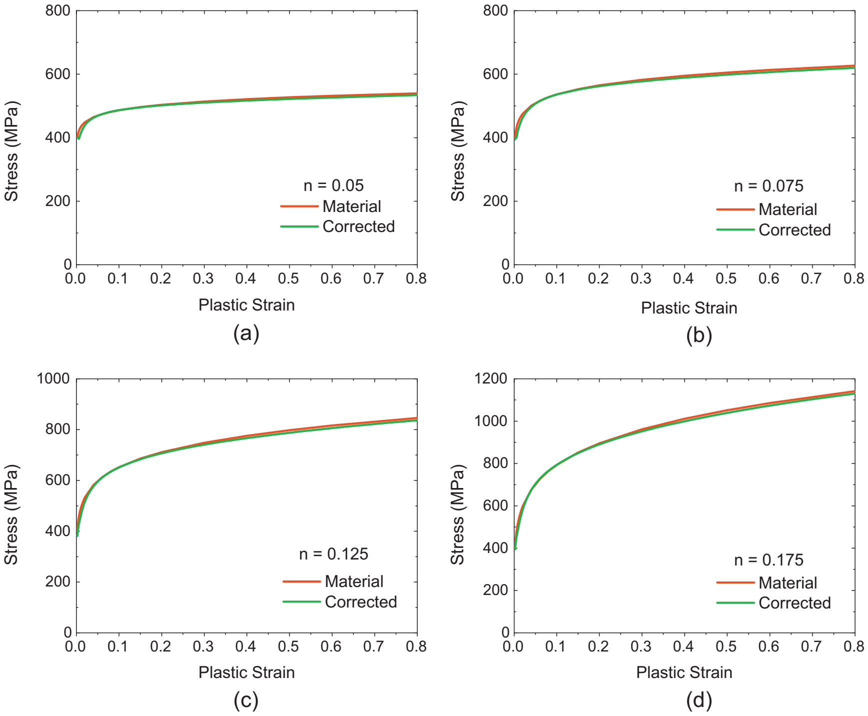

Fig. 7. G corrected flow stress-strain curves from the specimen with $a_0/R_0 = 2$: (a) n = 0.05, (b) n = 0.075, (c) n = 0.125, (d) n = 0.175. Material's flow stress-strain curves input for the analyses are denoted as green colour. (For interpretation of the references to colour in this figure legend, the reader is referred to the web version of this article.)

accurate flow stress-strain curves with absolute errors less than 1.5%. Based on these analyses, the notched tensile specimen with $a_0/R_0 = 2$ can be applied for direct derivation of flow stress-strain curve for homogeneous power-law hardening materials with a single value of correction factor defined by Eq. (4). Notched tensile specimen with $a_0/R_0 = 2$ is therefore identified as the special notched tensile specimen and notch geometry with $a_0/R_0 = 2$ is the so-called 'magic' notch. It should be noted that with the 'magic' notched specimen, no Bridgman correction is needed.

3.2. Origin of the ‘magic’ notch

It has been shown that the notched tensile specimen with $a_0/R_0 = 2$ can be used for directly deriving the flow stress-strain curve of any material that obeys the power-law hardening rule. In this section, the reason why the special notched tensile specimen functions well with only a single correction factor is discussed.

According to Bridgman’s analysis, the stress state in the minimum cross section is governed by the value of a/R. In order to illustrate the evolution of the notch geometry, the coordinates of the nodes at the root of the minimum cross section with an arc length close to 1 mm are fitted with the least square method. Fig. 8 shows the notch profile evolution for specimen with $a_0/R_0 = 2$ and hardening exponent $n = 0.15$ with the equivalent plastic strain varying from 0 to 0.8.

It can be seen from Fig. 8, as the equivalent plastic strain increases, the radius of the minimum cross section decreases and notch profile becomes more ‘curved’. The deformation highly concentrates at the minimum cross section resulting also in the decrease of the notch radius. Specially, when the equivalent plastic strain increases from 0 to 0.8, the radius of the minimum cross section varies from 6 to 4.02 mm with corresponding notch radius varying from 3 to 2.24 mm in Fig. 8.

The values of a/R for all the notched tensile specimens during loading are presented in Fig. 9. Considering low hardening exponent of recent high strength pipeline steels, such as X80, X100, material with $n = 0.05$ is studied and the evolution of a/R is also presented in Fig. 9. The trend of the evolution of a/R is different for each specimen. For the specimen with $a_0/R_0 = 3$, a/R decreases with the increase of the equivalent plastic strain, and larger hardening exponent yields a larger decrease of a/R at the same equivalent plastic strain. For the specimen with $a_0/R_0 = 2$, a/R decreases slightly firstly and then keeps constant when the equivalent plastic strain is larger than the value of hardening exponent. For the specimen with $a_0/R_0 = 1$, the value of a/R increases with the increase of the equivalent plastic strain. For the same initial notch geometry, hardening exponent has an influence on the evolution of a/R, which means that the evolution of a/R is not completely material independent.

Similar to the smooth round bar tensile specimen after necking, the true stress for a notched tensile specimen $\sigma_{T,notch}$ can be expressed as:

$$\sigma_{T,notch} = f\left(\frac{a}{R}\right) \cdot \sigma_{eq} \tag{7}$$

where f is the scaling factor which solely depends on the value of a/R and σ_{eq} is the Mises equivalent stress. As shown in Fig. 9, the value of a/R changes with the increase of equivalent plastic strain, except for the special notched tensile specimen when $\overline{\varepsilon^p} \geqslant n$. For the special notched tensile specimen, the scaling factor is therefore a constant when $\overline{\varepsilon^p} \geqslant n$ resulting in that the corrected flow stress-strain curves overlap with material flow stress-strain curves in a wide range of equivalent plastic strain.

4. Application to weldment and effect of geometry

The analysis above shows that notched tensile specimen with $a_0/R_0 = 2$ can be applied for direct measurement of material flow stress-strain curve. As mentioned in the introduction, application of the special notched tensile specimen to retrieve the material properties of each individual material zone in a weldment is of great interest. For this purpose, the effects of specimen geometry such as specimen outer diameter, the weld zone length in the notch region have been studied. The dimensions of notched tensile specimen with weld zone can be referred to Fig. 2.

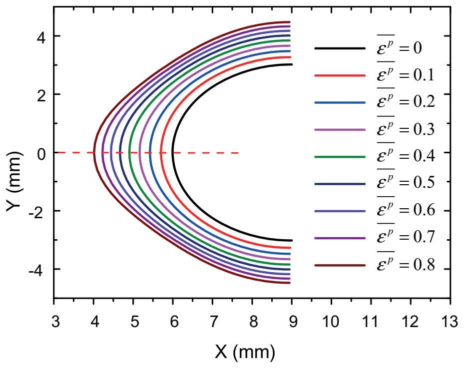

Fig. 8. Notch profile evolution of the notched tensile specimen with $a_0/R_0 = 2$ and $n = 0.15$.

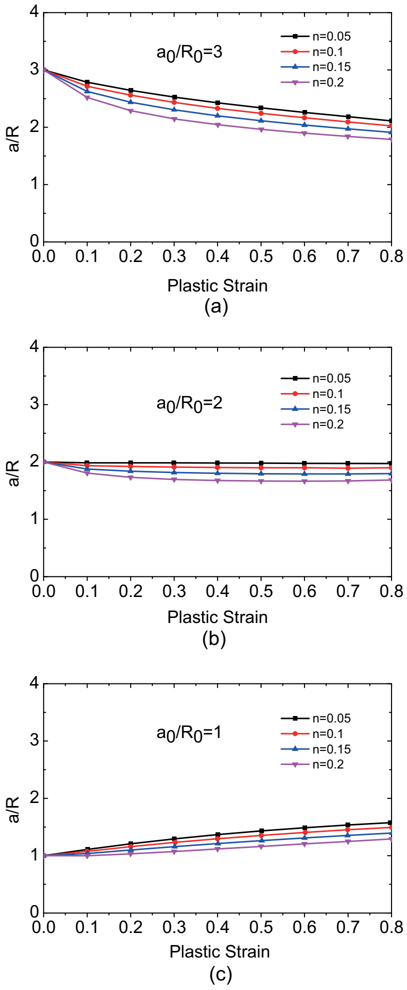

Fig. 9. Evolution of a/R: (a) $a_0/R_0 = 3$, (b) $a_0/R_0 = 2$, (c) $a_0/R_0 = 1$.

4.1. Effect of weld zone length

Strength mismatch and strain hardening mismatch are common characteristics of weldments due to different mechanical properties between the base material and weld metal. In the numerical analysis, $\sigma_0 = 400$ MPa, $n = 0.1$ have been taken as the yield stress and hardening exponent of the base material. The yield stress of the weld metal in the notched region varied from 300 MPa to 500 MPa to consider both strength undermatch and overmatch conditions. Strain hardening mismatch is considered with $n = 0.1$, 0.15 and 0.2 for weld metal. The length of weld zone H shown in Fig. 2 is normalized by initial diameter of the minimum cross section, and the values of H/D vary from 0.33 to 1.5.

$\sigma_{T,notch} - \varepsilon$ curves for specimens with weld zone are presented in Fig. 10. With the increase of H/D, the $\sigma_{T,notch} - \varepsilon$ curves calculated by Eq. (3) are collapsed into one curve quickly. For the case of strength overmatch in Fig. 10(b) and (d), the effect of weld zone length on the $\sigma_{T,notch} - \varepsilon$ curves is more obvious than the case with strength undermatch shown in Fig. 10(a), (c) and (e). For the case with overmatch shown in Fig. 10(b) and (d), $\sigma_{T,notch} - \varepsilon$ curves are collapsed into one curve

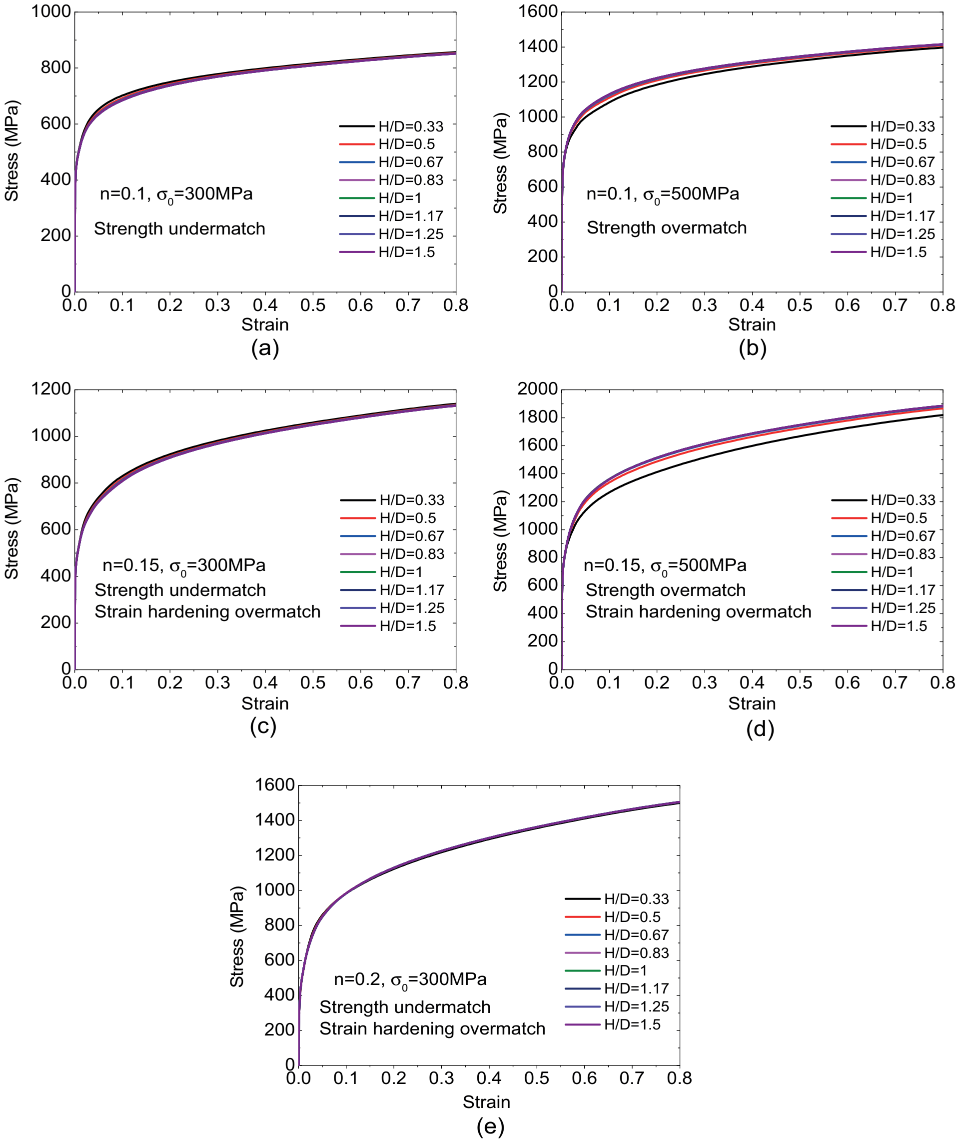

(a) (b) (c) (d) (e)

Fig. 10. $\sigma_{T,notch} - \varepsilon$ curves for the special notched tensile specimen ($a_0/R_0 = 2$) with different length of weld zone. $\sigma_0 = 400$ MPa and $n = 0.1$ are used for base material.

when $H/D > 0.5$. For the case with undermatch (strength undermatch or strain hardening undermatch), the deformation is always localized in the notched region and the weld zone length effect is not obvious. Based on these results, for a given weld zone length, it is recommended to machine notched tensile specimen with the initial radius of the minimum cross section no great than weld zone length, namely $a_0 \leqslant H$.

4.2. Effect of outer diameter

It should be noted that in all the analyses reported so far, the outer diameter of the special notched tensile specimen is constant, namely $d_0/a_0 = 4$. For the special notched tensile specimen, the outer diameter may influence the result of material flow stress-strain curve and its effect should be studied. In this section, numerical analyses have been conducted with d_0/a_0 varying from 2.5 to 4.5 and hardening exponent varying from 0.05 to 0.2. Results of corrected flow stress-strain curves are shown in Fig. 11 for hardening exponent $n = 0.05$ and 0.1 only.

It can be seen in Fig. 11 that the outer diameter has a strong effect on the results of corrected flow stress-stain curves. As it can be expected, the corrected flow stress-strain curves agree well with material flow stress-strain curves when $\overline{\varepsilon^p} < n$. With the increase of the equivalent plastic strain, the corrected flow stress-strain curves deviate with material flow stress-strain curve for $d_0/a_0 = 2.5$ and $d_0/a_0 = 3$. For $d_0/a_0 \geqslant 3.5$, the corrected flow stress-strain curves overlap with the material flow stress-strain curves. This is also seen for materials with $n = 0.075$, 0.125, 0.15, 0.175 and 0.2. Therefore, for the special notched tensile specimen, the value of outer diameter is recommended to be larger than $3.5a_0$. As discussed previously, the requirement of a_0 should be smaller than the weld zone length. Therefore, for the application of the special notched tensile specimen with weld zone, the specimen geometry is recommended to fulfil the condition: $a_0 \leqslant H, d_0 \geqslant 3.5a_0$.

4.3. Limitation of the ‘magic’ notch to materials with Lüders plateau

It should be noted that only the materials with the power-law hardening rule are considered so far. Materials with yield plateau or Lüders plateau are very common in practice, especially for materials used in the Arctic regions [22]. In order to explore the applicability of the special notched tensile specimen for materials with Lüders plateau, numerical analyses have been conducted with the special notched tensile specimen. The material flow stress-strain curves of the materials with Lüders plateau are described:

$$\overline{\sigma} = \begin{cases} \sigma_0 & \overline{\varepsilon^p} \leqslant \varepsilon_L \\ \sigma_0\left(1+\frac{\overline{\varepsilon^p}-\varepsilon_L}{\varepsilon_0}\right)^n & \overline{\varepsilon^p} > \varepsilon_L \end{cases} \tag{8}$$

ε_L is the length of Lüders plateau. In this study, an unrealistically large value $\varepsilon_L = 3\%$ has been used. The remaining parameters are the same as in Eq. (5). Results of corrected flow stress-strain curves with the ‘magic’ notched tensile specimen are plotted in Fig. 12. It can be seen that the corrected flow stresses increase smoothly without a clear plateau as the equivalent plastic strain increases. The errors between the corrected flow stress and material flow stress for $n = 0.1$, 0.15, 0.2 approach to 11.3%, 17.8%, 23.5%, respectively at the equivalent plastic strain $\overline{\varepsilon^p} = 3\%$. When the equivalent plastic strain $\overline{\varepsilon^p} > \varepsilon_L$, the corrected flow stress-strain curve overlaps with the material flow stress-strain curve for each material.

For materials with Lüders plateau, ideally, one could make two specimens to measure material true stress-strain curve. One is a standard smooth round bar specimen and the other one is the special notched tensile specimen. The whole stress-strain curve finally derived for a given material consists of two parts, one part is from the smooth round bar specimen when $\varepsilon \leqslant n$, the other part is from G corrected true stress-strain curve from the special notched tensile specimen when $\varepsilon > n$. In both cases, Bridgman correction is not necessary.

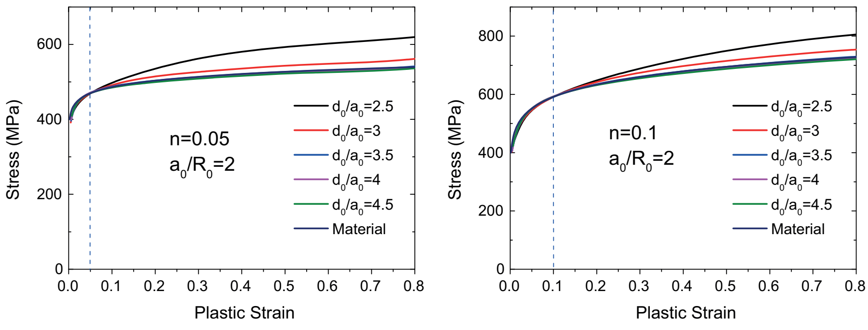

(a) (b)

Fig. 11. Corrected flow stress-strain curves for the special notched tensile specimens with different outer diameters. Material's flow stress-strain curves input for the analyses are denoted as dark blue colour. (For interpretation of the references to colour in this figure legend, the reader is referred to the web version of this article.)

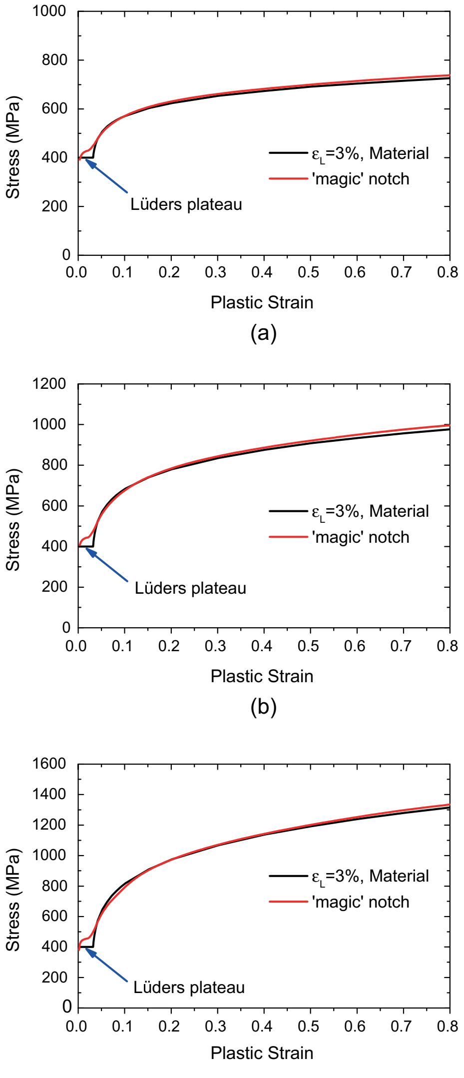

(a)

(b)

(c)

Fig. 12. Corrected flow stress-strain curves for materials with Lüders plateau (a) n = 0.1, (b) n = 0.15, (c) n = 0.2. Material's flow stress-strain curves input for the analyses are denoted as black colour.

5. Recommended procedure for flow stress-strain curve measurement with the special notched tensile specimen

The correction factor defined by Eq. (4) is unknown for a given material and also differs from material to material. The correction factors and the hardening exponents for the special notched tensile specimen obtained from numerical analyses are plotted in Fig. 13. The hardening exponent considered varies from 0.05 to 0.2, which covers a wide range of engineering materials following a power-law hardening rule.

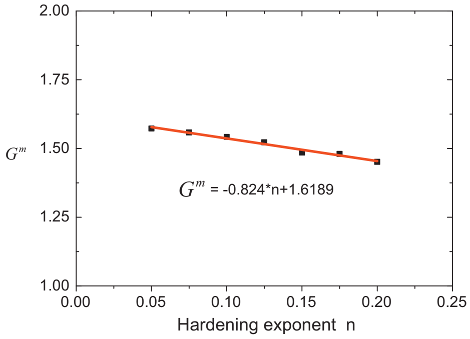

Fig. 13. Correction factor vs. hardening exponent for the special notched tensile specimen ($a_0/R_0 = 2$).

Fig. 13 can be linear fitted by:

$$G^m = -0.824 * n + 1.6189 \tag{9}$$

Once one knows the hardening exponent, the correction factor can be calculated from Eq. (9). The hardening exponent can be conveniently taken as the strain at the maximum stress on an engineering stress-strain curve of either a smooth or a notched tensile specimen. Therefore, for material that follows a power-law hardening rule, the flow stress-strain curve can be measured with the special notched tensile specimen with the following steps:

(1) Prepare the specimens with the geometric requirements: $a_0/R_0 = 2$ and $a_0 \leqslant H, d_0 \geqslant 3.5a_0$.
(2) Perform notched tensile tests.
(3) Calculate the $\sigma_{e,notch} - \varepsilon$ curve and $\sigma_{T,notch} - \varepsilon$ curve, determine the hardening exponent from $\sigma_{e,notch} - \varepsilon$ curve (the value of strain at the maximum stress).
(4) Calculate the correction factor with Eq. (9) and correct the $\sigma_{T,notch} - \varepsilon$ curve with correction factor to obtain the G corrected true stress-strain curve, and then convert to flow stress-strain curve with Eq. (6).

6. Conclusions

In this study, a special notched tensile specimen has been identified and a procedure is proposed to determine the material flow stress-strain curve without Bridgman correction. The special notched tensile specimen can be applied to both homogeneous material and weldments. Numerical analysis shows that outer diameter should be 3.5 times larger than initial radius of the minimum cross section in order to use the special notched tensile specimen. For weldments, the initial radius of the minimum cross section is recommended to be smaller than material zone length in notch region. It should be noted that the corrected flow stress derived with the special notched tensile specimen is less accurate for material with significant Lüders plateau in the initial yield stage.

Acknowledgement

The Chinese Scholarship Council is greatly acknowledged for the financial support. The authors wish to thank the Research Council of Norway for funding through the Petromaks 2 Programme, Contract No. 228513/E30.

References

[1] Bridgman PW. Studies in larger plastic flow and fracture. New York: McGraw-Hill; 1952.
[2] La Rosa G, Risitano A, et al. Post-necking elastoplastic characterization: degree of approximation in the Bridgman method and properties of the flow-stress/true-stress ratio. Metall Mater Trans A 2003;34(3):615–24.
[3] Bao Y, Wierzbicki T. On fracture locus in the equivalent strain and stress triaxiality space. Int J Mech Sci 2004;46(1):81–98.
[4] Bao Y. Dependence of ductile crack formation in tensile tests on stress triaxiality, stress and strain ratios. Engng Fract Mech 2005;72(4):505–22.
[5] Alves M, Jones N. Influence of hydrostatic stress on failure of axisymmetric notched specimens. J Mech Phys Solids 1999;47(3):643–67.
[6] La Rosa G, Mirone G, et al. Effect of stress triaxiality corrected plastic flow on ductile damage evolution in the framework of continuum damage mechanics. Engng Fract Mech 2001;68(4):417–34.
[7] Bai Y, Teng X, et al. On the application of stress triaxiality formula for plane strain fracture testing. J Engng Mater Technol 2009;131(2):021002.
[8] Le Roy G, Embury JD, et al. A model of ductile fracture based on the nucleation and growth of voids. Acta Metall 1981;29(8):1509–22.
[9] Tvergaard V. Necking in tensile bars with rectangular cross-section. Comput Methods Appl Mech Engng 1993;103(1–2):273–90.
[10] Zhang ZL, Hauge M, et al. Determining material true stress–strain curve from tensile specimens with rectangular cross-section. Int J Solids Struct 1999;36(23):3497–516.

[11] Zhang ZL, Ødegård J, et al. A study on determining true stress–strain curve for anisotropic materials with rectangular tensile bars. Int J Solids Struct 2001;38(26):4489–505.
[12] Zhang ZL, Ødegård J, et al. Determining true stress–strain curve for isotropic and anisotropic materials with rectangular tensile bars: method and verifications. Comput Mater Sci 2001;20(1):77–85.
[13] Ling Y. Uniaxial true stress-strain after necking. AMP J Technol 1996;5:37–48.
[14] Zhang ZL, Hauge M, et al. A notched cross weld tensile testing method for determining true stress–strain curves for weldments. Engng Fract Mech 2002;69(3):353–66.
[15] Berto F, Gallo P, et al. High temperature fatigue tests of un-notched and notched specimens made of 40CrMoV13.9 steel. Mater Des 2014;63:609–19.
[16] Gallo P, Berto F, Lazzarin P. High temperature fatigue tests of notched specimens made of titanium Grade 2. Theoret Appl Fract Mech 2015;76:27–34.
[17] Wormsen A, Avice M, et al. Fatigue testing and analysis of notched specimens with typical subsea design features. Int J Fatigue 2015;81:275–98.
[18] Noda NA, Takase Y. Stress concentration formula useful for all notch shape in a round bar (comparison between torsion, tension and bending). Int J Fatigue 2006;28(2):151–63.
[19] Giglio M, Manes A, et al. Ductile fracture locus of Ti–6Al–4V titanium alloy. Int J Mech Sci 2012;54(1):121–35.
[20] Gao X, Zhang T, et al. Effects of the stress state on plasticity and ductile failure of an aluminum 5083 alloy. Int J Plast 2009;25(12):2366–82.
[21] Zhang ZL, Niemi E. Studies on the ductility predictions by different local failure criteria. Engng Fract Mech 1994;48(4):529–40.
[22] Ren X, Nordhagen HO, et al. Tensile properties of 420 MPa steel at low temperature. In: The twenty-fifth international offshore and polar engineering conference. International Society of Offshore and Polar Engineers; 2015.

A.2

Paper II

A method for determining material's equivalent stress-strain curve with any axisymmetric notched tensile specimens without Bridgman correction

Authors: Shengwen Tu; Xiaobo Ren; Jianying He; Zhiliang Zhang

International Journal of Mechanical Sciences. 135 (2018), 656-667

International Journal of Mechanical Sciences 135 (2018) 656–667

Contents lists available at ScienceDirect

International Journal of Mechanical Sciences

journal homepage: www.elsevier.com/locate/ijmecsci

A method for determining material's equivalent stress-strain curve with any axisymmetric notched tensile specimens without Bridgman correction

Shengwen Tu[a], Xiaobo Ren[b], Jianying He[a], Zhiliang Zhang[a,*]

[a] Department of Structural Engineering, Norwegian University of Science and Technology, Trondheim 7491, Norway
[b] SINTEF Materials and Chemistry, Trondheim 7456, Norway

ARTICLE INFO

Keywords:
Equivalent stress-strain curve
Notched tensile specimen
Weldment
Bridgman correction
Testing method

ABSTRACT

Large deformation analyses of problems such as plastic forming, ductile fracture with finite element method need a full range of material's equivalent stress-strain curve or flow stress-strain curve. The equivalent stress-strain curve determined from the smooth round bar specimen should be corrected after diffuse necking, since tri-axial stress state occurs in the neck. The well-known Bridgman correction method is a candidate, however, it is not accurate as the strain increases. Furthermore, it is impossible to measure the equivalent stress-strain curve of each individual material zone in a weldment with cross weld tensile tests. To cope with these challenges, a correction function and an associated test procedure are proposed in this study. With the proposed procedure, the true stress-strain curve from any axisymmetric notched tensile specimen can be converted to the material's equivalent stress-strain curve accurately and no Bridgman correction is needed. The proposed procedure can be applied to both perfectly plastic and strain hardening materials. The equivalent stress-strain curve of each individual material zone in a weldment can also be measured with the proposed procedure.

1. Introduction

Large deformation analyses of problems such as plastic forming [1,2], ductile fracture [3-7] with finite element method need a full range of material's equivalent stress-strain curve or flow stress-strain curve. For homogeneous materials, the true stress-strain curve can be measured by performing uniaxial tensile test with smooth round bar specimen or rectangular cross-section specimen [8-12]. However, the determination of the true stress-strain curve of each individual material zone in a weldment is difficult, due to the inhomogeneity of the weldment and the unpredictable fracture location on the cross weld tensile specimen. Zhang, Hauge, Thaulow and Ødegård [13] proposed a method to determine the true stress-strain curve of a weldment with axisymmetric notched tensile specimen. The true stress-strain curve from an axisymmetric notched tensile specimen can be converted to the true stress-strain curve of a smooth round bar specimen by a so-called G factor. The notch can be located either in the base metal, weld metal or possibly the heat affect zone (HAZ).

It is worth noting that whether from a smooth round bar specimen [8-10] or by conversion from an axisymmetric notched tensile specimen [13], the true stress-strain curve deviates from the material's equivalent stress-stress curve, since the tri-axial stress state occurs in the localized region after the onset of diffuse necking [8,14]. In general, the true stress-strain curve should be corrected. Several approaches have been proposed for the correction of the initially smooth round bar tensile specimen [15-17]. The well-known Bridgman correction method [18] is widely referred in the literature. By assuming a uniform distribution of the equivalent strain in the minimum cross section, Bridgman proposed an analytical solution of stress distribution in the minimum cross section of a necked specimen. Application of the Bridgman correction method is expensive since the current notch radius ratio (the minimum cross section radius a over the notch radius R) a/R should be measured simultaneously during the test [14,19]. Even with the value of notch radius measured, the equivalent stress-strain curve corrected by the Bridgman correction method is not accurate when the strain is large [19]. Bao [20] performed numerical analysis with a smooth round bar specimen and showed that the stress distribution in the minimum cross-section differed significantly to the Bridgman's analytical solution at the strain $\varepsilon = 0.29$. The inaccuracy of the Bridgman correction method attributes to the assumption that the equivalent strain is uniformly distributed in the minimum cross section.

An alternative method with more accurate results and lower test cost has been proposed recently to measure material's flow stress-strain curve [21]. The authors further studied the axisymmetric notched tensile specimen with numerical analyses and a special notch geometry with $a_0/R_0 = 2$ has been identified. a_0 and R_0 are the initial minimum cross-section radius and the initial notch radius, respectively. With this

---

* Corresponding author.
E-mail address: zhiliang.zhang@ntnu.no (Z. Zhang).

https://doi.org/10.1016/j.ijmecsci.2017.12.012
Received 16 August 2017; Received in revised form 11 November 2017; Accepted 7 December 2017

Nomenclature

a	instantaneous minimum cross-section radius
a_0	initial minimum cross-section radius
d_0	outer diameter of the notched tensile specimen
E	Young's modulus
H	material zone length in the notch region
n	material's hardening exponent
P	tensile load
R	instantaneous notch radius
R_0	initial notch radius
a_0/R_0	initial notch radius ratio
ν	Poisson's ratio
ε_0	yield strain
ε	average true strain
$\overline{\varepsilon^p}$	equivalent plastic strain
ε_N	true strain at necking for smooth round bar specimen
$\varepsilon_{P\max}$	true strain at the maximum tensile load
σ_0	yield stress
$\sigma_{0.2}$	0.2% offset yield stress
σ_T	true stress from smooth round bar specimen
$\sigma_{0.5}$	yield stress corresponding to 0.5% total strain
$\overline{\sigma}$	flow stress
$\sigma_{e,notch}$	engineering stress from an axisymmetric notched tensile specimen
σ_{eq}	von Mises equivalent stress
$\sigma_{T,notch}$	average true stress from an axisymmetric notched tensile specimen
ξ	ratio between the average true stress from an axisymmetric notched tensile specimen and the material's equivalent stress at the same strain

'magic' notched tensile specimen and a smooth round bar specimen, the equivalent stress-strain curve of the hardening material can be directly derived with a single G factor and no Bridgman correction is needed. Good agreements between the equivalent stress-strain curves input for numerical analyses and the G-corrected equivalent stress-strain curves with the 'magic' notched tensile specimen have been observed. Similar with the Bridgman correction method, the proposed 'magic' notch method is not accurate for the perfectly plastic or weak hardening material [15].

In the present study, a new correction function is proposed to determine the material's equivalent stress-strain curve with any axisymmetric notched tensile specimens rather than the only 'magic' notch. The proposed correction function depends on the deformation level (the average true strain ε), the true strain corresponding to the maximum tensile load $\varepsilon_{P\max}$ and the initial notch geometry a_0/R_0 of the specimen. Different notch configurations can be used. The proposed correction function herein can also be applied to perfectly plastic materials.

The paper consists of the following sections. In Section 2, the axisymmetric notched tensile specimen is introduced, along with the definitions of the specimen geometry used in this study. Details of the numerical procedure and materials used are presented in Section 3. Results from the numerical analyses, the influence of notch radius ratio, as well as the derivation of the correction function are presented in Section 4. Verification and application of the proposed correction function are discussed in Section 5. The main conclusions are summarized in Section 6.

2. Axisymmetric notched tensile specimen

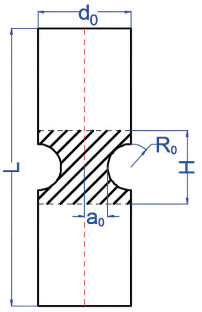

Fig. 1. Geometry of an axisymmetric notched tensile specimen.

The axisymmetric notched tensile specimen has a wide range of applications in characterizing material's mechanical properties [22-25], especially for the metallic material fracture locus measurement in the range of stress triaxiality larger than 1/3 [26-28]. In order to conquer the limitations of the conventional cross weld tensile test, Zhang, Hauge, Thaulow and Ødegård [13] proposed a method to determine the true stress-strain curve of each individual material zone of weldments with the axisymmetric notched tensile specimen. The sketch of an axisymmetric notched tensile specimen is shown in Fig. 1. Due to the existence of a notch on the specimen, the deformation localizes mainly in the notched region under uniaxial tension. During the tensile testing, the average true strain ε is defined by the minimum cross-section area reduction:

$$\varepsilon = 2 \cdot \ln(a_0/a) \tag{1}$$

where a is the instantaneous minimum cross-section radius, which can be measured by a linear variable displacement transducer. The true stress $\sigma_{T,notch}$ and the engineering stress $\sigma_{e,notch}$ from an axisymmetric notched tensile specimen are calculated by dividing the load P by the current minimum cross-section area and the initial minimum cross-section area, respectively.

$$\sigma_{T,notch} = P/\pi a^2 \tag{2}$$

$$\sigma_{e,notch} = P/\pi a_0^2 \tag{3}$$

Recent study by the authors [21] showed that the true stress calculated by Eq. (2) with the axisymmetric notched tensile specimen is independent of the specimen outer diameter d_0 when the geometry condition $d_0 \geq 3.5a_0$ is fulfilled. In order to measure the equivalent stress-strain curve of each individual material zone of a weldment, the authors carried out a series of numerical analyses and found that the true stress from an axisymmetric notched tensile specimen is unique and independent of the material zone length when $a_0 \leq H$. When these geometry requirements are fulfilled, the axisymmetric notched tensile specimen can be characterized by the initial notch radius ratio, a_0/R_0.

The strategy of the present study is illustrated in Fig. 2. The assumed materials' equivalent stress-strain curves are used for numerical analyses first. Then, the true stress-strain curves output from the numerical analyses are studied to derive the proposed correction function. With the proposed correction function, the true stress-strain curve from an axisymmetric notched tensile specimen can be converted to the material's equivalent stress-strain curve.

3. Numerical procedure

3.1. Finite element model

A series of numerical analyses of axisymmetric notched tensile specimens with a_0/R_0 varying from 0.25 to 3 have been performed with Abaqus/standard 6.14. $a_0 = 6$ mm is used for all the notched tensile specimens, with R_0 varying from 2 to 24 mm. The outer diameter is

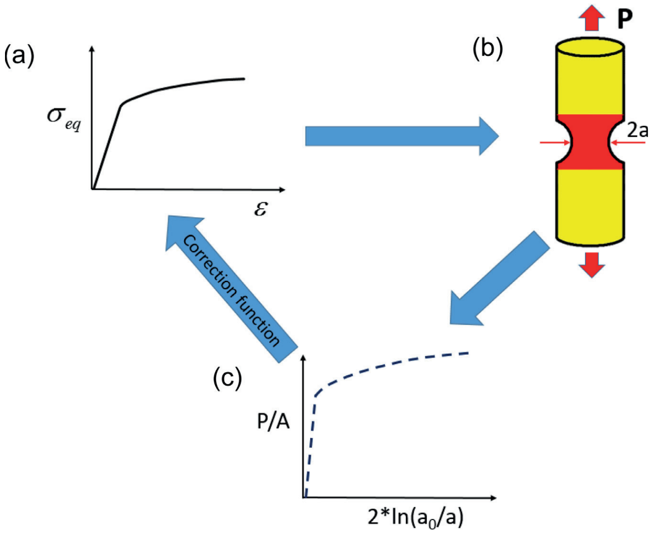

Fig. 2. Layout of the present study: (a) Assumed material's equivalent stress-strain curve; (b) Numerical tensile tests with axisymmetric notched tensile specimens, material in red can be undermatched, overmatched or evenmatched with the base material in yellow; (c) True stress-strain curve for the notched specimen obtained from (b). With the proposed correction function, true stress-strain curve in Fig. 2(c) can be corrected back to Fig. 2(a).

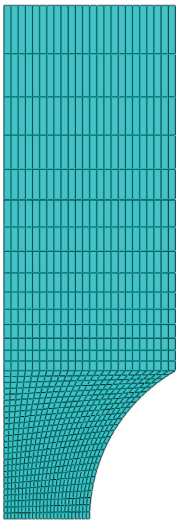

Fig. 3. Mesh of the axisymmetric notched tensile specimen with $a_0/R_0 = 0.5$.

24 mm, which meets the geometry requirement: $d_0 \geq 3.5a_0$. Axisymmetric model has been used with the element type CAX4R. Large deformation is accounted. A typical finite element meshes is shown in Fig. 3 for the axisymmetric notched tensile specimen with $a_0/R_0 = 0.5$. Average mesh size in the notch center is 0.5×0.5 mm and relative coarse meshes are used in the remaining part. Symmetric boundary condition is applied in the minimum cross-section. The specimen is loaded under displacement control.

3.2. Materials

The flow stress-strain curves of the materials used in this study are assumed to follow a power law hardening rule [29]:

$$\bar{\sigma} = \sigma_0 \left(1 + \frac{\overline{\varepsilon^p}}{\varepsilon_0}\right)^n \tag{4}$$

where $\bar{\sigma}$, $\overline{\varepsilon^p}$ are the flow stress and the equivalent plastic strain, respectively. $\sigma_0 = E\varepsilon_0$ describes the elastic behavior of the material. The yield stress $\sigma_0 = 400$ MPa, the Young's modulus $E = 200$ GPa, and corresponding yield strain $\varepsilon_0 = 0.002$ have been used together with the Poisson's ratio $\nu = 0.3$, for all the numerical analyses. Hardening of the material is characterized by a single hardening exponent *n*. In this study, numerical analyses with hardening exponents ranging from 0 to 0.2 have been investigated, representing most engineering materials. For a given hardening exponent *n*, the flow stress-strain curve can be converted to the equivalent stress-strain curve by Eq. (5):

$$\begin{cases} \sigma_{eq} = \bar{\sigma},\ \varepsilon = \bar{\sigma}/E & \overline{\varepsilon^p} = 0 \\ \sigma_{eq} = \bar{\sigma},\ \varepsilon = \frac{\bar{\sigma}}{E} + \overline{\varepsilon^p} & \overline{\varepsilon^p} > 0 \end{cases} \tag{5}$$

In the following sections, material's equivalent stress-strain curve is calculated by converting the corresponding flow stress-strain curve by Eq. (5). By combining different hardening exponents and initial notch radius ratios (a_0/R_0), in total 30 analyses have been performed to derive the correction function in Section 4.

4. Derivation of the correction function

4.1. Normalized $\sigma_{\mathrm{T,notch}} - \varepsilon$ and $\sigma_{\mathrm{e,notch}} - \varepsilon$ curves from numerical analyses

The true stress-strain curves ($\sigma_{T,notch} - \varepsilon$) calculated by Eq. (2) for the axisymmetric notched tensile specimens are normalized by the yield

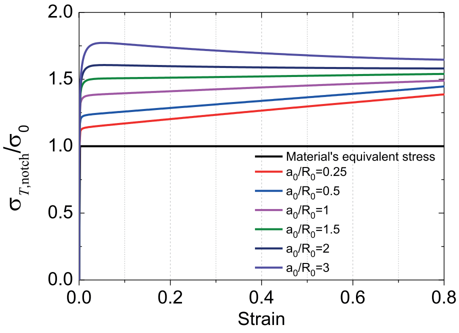

Fig. 4. Normalized $\sigma_{T,notch}-\varepsilon$ curves of the axisymmetric notched tensile specimens for the perfectly plastic material ($n=0$). The material's equivalent stress-strain curve is denoted as black.

stress and are presented in Fig. 4 for the perfectly plastic material and Fig. 5 for hardening materials. The corresponding materials' equivalent stress-strain curves are also presented.

As expected, for axisymmetric notched tensile specimens with the same hardening exponent in Fig. 4 and Fig. 5, the true stress calculated by Eq. (2) is larger than the material's equivalent stress at the same strain, and the sharper notch (larger value of a_0/R_0) yields a larger true stress. It is interesting to note that for the perfectly plastic material shown in Fig. 4, the true stress increases with the increase of the strain for the specimen with $a_0/R_0 < 1.5$. For the specimen with $a_0/R_0=3$, the true stress increases when the strain is small, and then decreases as the strain increases. For the specimens with $a_0/R_0=1.5$ and $a_0/R_0=2$, the true stress increases firstly, and then varies slightly as the strain increases. It indicates that, with a single correction parameter, the true stress output from an axisymmetric notched tensile specimen with $a_0/R_0=1.5$ or $a_0/R_0=2$ can be converted to the material's equivalent stress. This has been investigated by the authors for hardening materials [21], and the axisymmetric notched tensile specimen with $a_0/R_0=2$ has been proved to present a good agreement between the material's equivalent stress-strain curve and the corrected stress-strain curve with a single G factor.

Indeed, the effect of the initial notch radius ratio (a_0/R_0) on the resulting true stress-strain curve also occurs for hardening materials shown in Fig. 5. However, it is difficult to observe this phenomenon due to the materials' strain hardening. The reason for the initial notch radius ratio effect is mainly due to the stress distribution on the minimum cross-section and will not be discussed in this paper.

The normalized engineering stress-true strain curves (normalized $\sigma_{e,notch}-\varepsilon$) of the axisymmetric notched tensile specimens with hardening exponents $n=0.1$ and $n=0.2$ are presented in Fig. 6. As expected, the engineering stress decreases after reaching the maximum value, for all the notched tensile specimens. It has been demonstrated that the strain corresponding to the maximum value of the engineering stress is approximately equal to the material's hardening exponent ($\varepsilon_{P\max} \approx n$), independent of the initial notch radius ratio [13,21]. This is further investigated and a function describes the notch effect on diffuse necking is established in this paper.

4.2. The derivation of the correction function

4.2.1. Normalizing the ratio between the true stress and the material's equivalent stress

The purpose for this study is to provide a simple correction function to convert the true stress-strain curve from an axisymmetric notched tensile specimen to the material's equivalent stress-strain curve. The ratio ξ between the true stress from an axisymmetric notched tensile specimen and the material's equivalent stress in Fig. (4)–(5) are calculated by Eq. (6), with the strain varying from 0.01 to 0.8.

$$\xi = \frac{\sigma_{T,notch}}{\sigma_{eq}}\Big|_{\varepsilon} \tag{6}$$

The ξ versus the strain for the axisymmetric notched tensile specimens with $a_0/R_0=3$ and hardening exponents from 0 to 0.2 are presented in Fig. 7. It can be seen in Fig. 7(a) that the curves for different hardening exponents show similar trend. The values of ξ increases with the increase of the strain initially, and then decreases, for all the materials shown in Fig. 7(a). By taking the ratio ξ at strain $\varepsilon=0.8$ as a reference, the curves in Fig. 7(a) are normalized and the results are presented in Fig. 7(b). Interestingly, the normalized curves in Fig. 7(b) collapse into one, except small deviations when the strain is very small. Same behavior of the $\xi-\varepsilon$ curves is also observed in Fig. 8-12 for the notched tensile specimens with a_0/R_0 ranging from 0.25 to 2.

The influence of notch radius ratio on the true stress-strain curve of axisymmetric notched tensile specimens has been analyzed previously for the perfectly plastic material. Interestingly, the influence of notch radius ratio (a_0/R_0) can also be observed from the normalized $\xi-\varepsilon$ curves, as seen in Fig. 7(b)–12 (b). The value of normalized ξ for notched tensile specimens with $a_0/R_0 > 1.5$ decreases as the strain increases, and larger a_0/R_0 corresponds a faster decrease of the normalized ξ. On the contrary, the value of normalized ξ for notched tensile specimens with $a_0/R_0 > 1.5$ increases with the increase of the strain, and smaller a_0/R_0 yields a faster increase of the normalized ξ. Therefore, we may conclude that the notch radius ratio effect is determined by the notch geometry (a_0/R_0), independent of the material's hardening exponent.

4.2.2. Normalizing $\xi_{\varepsilon=0.8}$

The ratio between the true stress and the material's equivalent stress at $\varepsilon=0.8$ (namely the reference points $\xi_{\varepsilon=0.8}$ used in Fig. 7-12) versus the materials' hardening exponents for axisymmetric notched tensile specimens with different notch geometries are shown in Fig. 13, with hardening exponents up to 0.35. For a given axisymmetric notched tensile specimen (a_0/R_0), the value of $\xi_{\varepsilon=0.8}$ decreases with increasing hardening exponent. Very interestingly, for axisymmetric notched tensile specimens with different notch geometries, the curves in Fig. 13(a) behave similar to each other and can be normalized. By taking the value of $\xi_{\varepsilon=0.8}$ for material with the hardening exponent $n=0$ ($\xi_{\varepsilon=0.8,\, n=0}$) as a reference, the curves for axisymmetric notched tensile specimens with different notch geometries in Fig. 13(a) can be normalized. The corresponding normalized curves are presented in Fig. 13(b). As it can be seen, the normalized curves in Fig. 13(b) collapse into one, which can be fitted by Eq. (7):

$$f(n) = -0.22942 \cdot n^2 - 0.36902 \cdot n + 1 \tag{7}$$

where n is the material's hardening exponent. Eq. (7) describes the material's hardening effect on the true stress-strain curves from notched specimen. As mentioned previously, for materials obeying the power law hardening (see Eq. (4)), the hardening exponent n approximately equals to the true strain at the maximum tensile load, $\varepsilon_{P\max}$. We further investigate $\varepsilon_{P\max}$ for each numerical analysis for hardening materials in Section 4.1. The $\varepsilon_{P\max}$ for each case is normalized by the hardening exponent n and is plotted against the initial notch radius ratio in Fig. 14. As can be seen, the normalized $\varepsilon_{P\max}$ presents a small scatter at the given a_0/R_0 and decreases with the increase of a_0/R_0, for all the hardening exponents discussed here. Fig. 14 indicates that sharper notch accelerates the diffuse necking, while the shallow notch postpones the diffuse necking. Fig. 14 is then fitted by Eq. (8).

$$\varepsilon_{P\max}/n = 0.0466 \cdot \left(a_0/R_0\right)^2 - 0.2515 \cdot \left(a_0/R_0\right) + 1.2462 \tag{8}$$

Eq. (8) describes the notch effect on diffuse necking. The strain hardening exponent n can be determined with Eq. (8) when $\varepsilon_{P\max}$ from a notched specimen is measured. For a given notched tensile specimen,

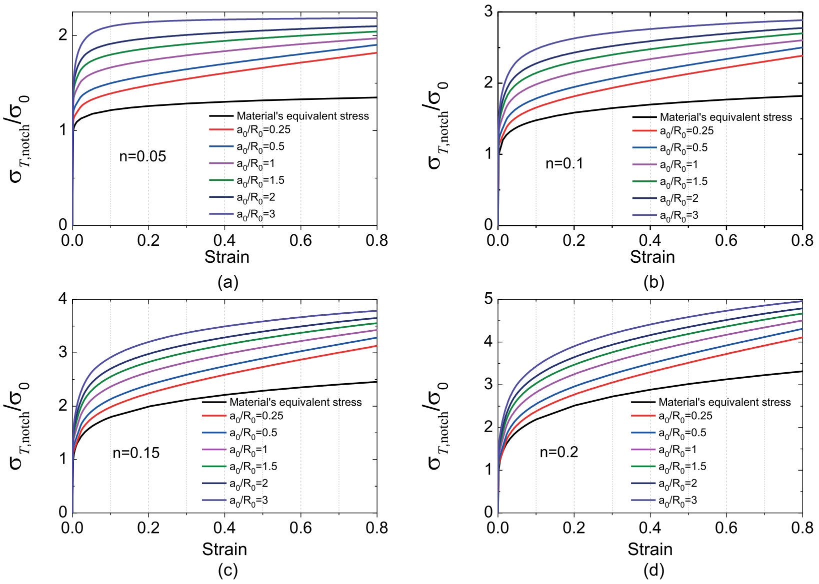

Fig. 5. Normalized $\sigma_{T,notch} - \varepsilon$ curves of axisymmetric notched tensile specimens with different notch configurations: (a) $n = 0.05$; (b) $n = 0.1$; (c) $n = 0.15$; (d) $n = 0.2$. The corresponding materials' equivalent stress-strain curves are shown in black.

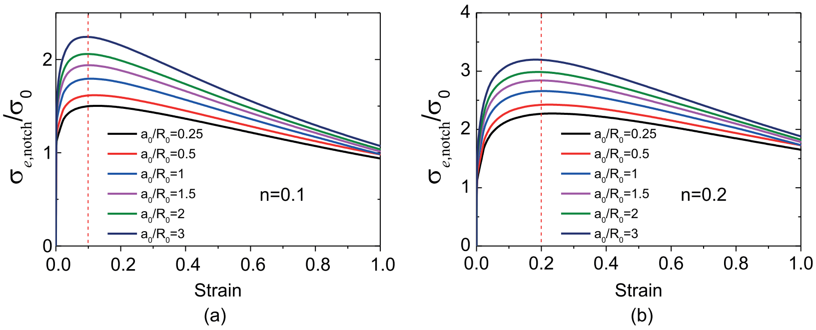

Fig. 6. Normalized $\sigma_{e,notch} - \varepsilon$ curves of axisymmetric notched tensile specimens: (a) $n = 0.1$; (b) $n = 0.2$. The strains corresponding to the maximum engineering stresses are shown with red lines.

the ratio ξ at the strain $\varepsilon = 0.8$ can be calculated, once $\varepsilon_{P\max}$ and the reference value $\xi_{\varepsilon=0.8,\,n=0}$ is known:

$$\xi_{\varepsilon=0.8} = f(n) \cdot \xi_{\varepsilon=0.8,n=0} \tag{9}$$

4.2.3. The proposed correction function

As mentioned previously, for a given axisymmetric notched tensile specimen with different material properties (namely, different hardening exponents), the normalized $\xi - \varepsilon$ curves collapse into one and can be linearly fitted by Eq. (10), as seen in Fig. 7(b)–12(b).

$$g_{a_0/R_0}(\varepsilon) = (b_1 * \varepsilon + b_2)_{a_0/R_0} \tag{10}$$

where b_1 and b_2 are the slope and the intersection of Eq. (10), respectively. The subscript in Eq. (10) denotes the initial notch radius ratio for a given axisymmetric notched tensile specimen. Combining Eq. (9) and (10), the ratio ξ can be written as:

$$\xi = f(n) \cdot \xi_{\varepsilon=0.8,n=0} \cdot g_{a_0/R_0}(\varepsilon) \tag{11}$$

Considering that the $\xi - \varepsilon$ curves in Fig. 7(a)–12(a) are normalized by $\xi_{\varepsilon=0.8}$, the product of the second and third term in Eq. (11) returns back to the linear fitted curves for the perfectly plastic materials ($n = 0$) in Fig. 7(a)–12(a). In this case, $\xi_{\varepsilon=0.8,\,n=0}$ cancels out and Eq. (11) can be written:

$$\begin{gathered} \xi = f(n) \cdot g_{a_0/R_0,n=0}(\varepsilon) \\ g_{a_0/R_0,n=0}(\varepsilon) = \left(b_{1,n=0} \cdot \varepsilon + b_{2,n=0}\right)_{a_0/R_0} \end{gathered} \tag{12}$$

where $b_{1,n=0}$ and $b_{2,n=0}$ are the slope and intersection from the linear fitting of the curves for $n = 0$ in Fig. 7(a)–12(a), respectively. Corresponding values of $b_{1,n=0}$ and $b_{2,n=0}$ of Eq. (12) are listed in Table 1 and are presented in Fig. 15 as functions of the initial notch radius ratio. The

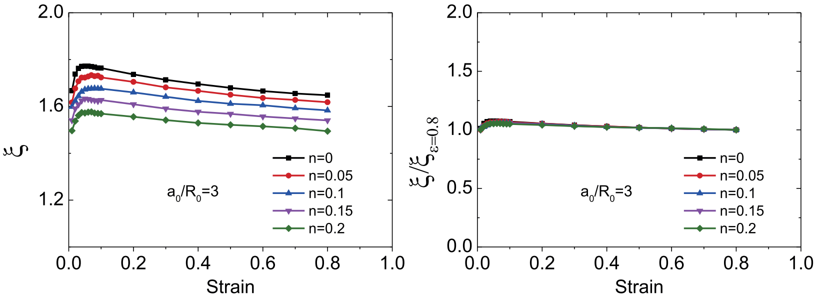

(a)

(b)

Fig. 7. (a) ξ versus ε for the axisymmetric notched tensile specimen with $a_0/R_0 = 3$ and n ranging from 0 to 0.2; (b) Normalized curves of Fig. 7(a) by $\xi_{\varepsilon=0.8}$.

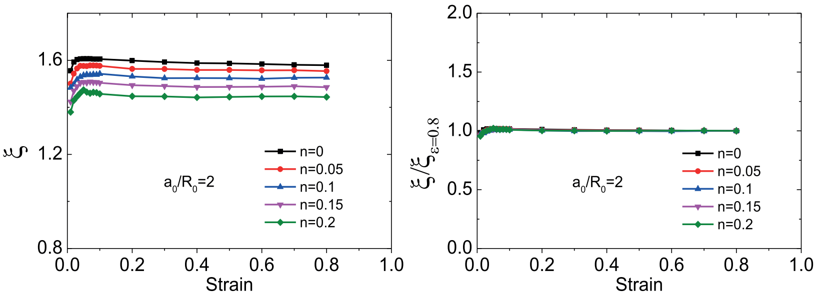

(a)

(b)

Fig. 8. (a) ξ versus ε for the axisymmetric notched tensile specimen with $a_0/R_0 = 2$ and n ranging from 0 to 0.2; (b) Normalized curves of Fig. 8(a) by $\xi_{\varepsilon=0.8}$.

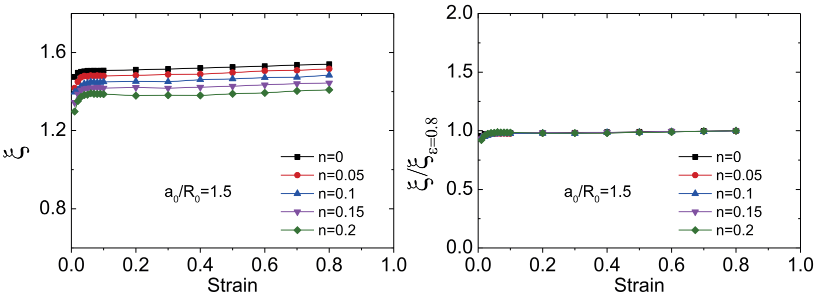

(a)

(b)

Fig. 9. (a) ξ versus ε for the axisymmetric notched tensile specimen with $a_0/R_0 = 1.5$ and n ranging from 0 to 0.2; (b) Normalized curves of Fig. 9(a) by $\xi_{\varepsilon=0.8}$.

value of slope of Eq. (12) decreases with the increase of the initial notch radius ratio; inversely, the value of the intersection increases. The slope represents the notch radius ratio effect, while the intersection infers the stress concentration due to the existence of notch. The data in Fig. 15(a) and (b) are fitted by Eq. (13) and Eq. (14):

$$b_{1,n=0} = 0.03232\left(\frac{a_0}{R_0}\right)^2 - 0.27\left(\frac{a_0}{R_0}\right) + 0.3866 \tag{13}$$

$$b_{2,n=0} = -0.04084\left(\frac{a_0}{R_0}\right)^2 + 0.3557\left(\frac{a_0}{R_0}\right) + 1.0577 \tag{14}$$

Inserting Eq. (13)-(14) into Eq. (12), the ratio ξ between the true stress from an axisymmetric notched tensile specimen and the material's equivalent stress can be written in a general format:

$$\xi = (b_{1,n=0} \cdot \varepsilon + b_{2,n=0}) \cdot f(n) \tag{15}$$

Eq. (15) consists of two terms: the first term is related to the initial notch geometry and is a function of the average true strain ε; the second term is a function of the hardening exponent n, considering the material's

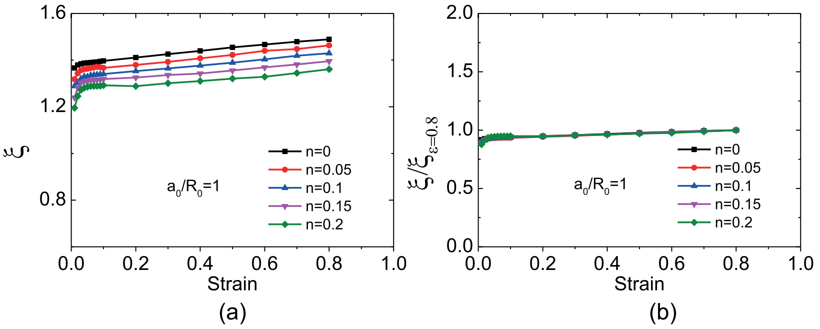

(a)

(b)

Fig. 10. (a) ξ versus ε for the axisymmetric notched tensile specimen with $a_0/R_0 = 1$ and n ranging from 0 to 0.2; (b) Normalized curves of Fig. 10(a) by $\xi_{\varepsilon=0.8}$.

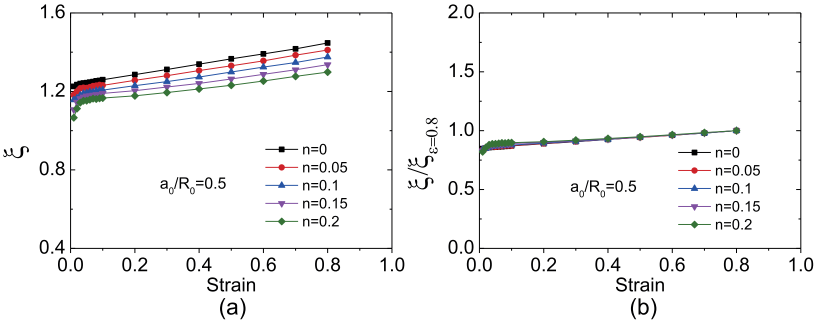

(a)

(b)

Fig. 11. (a) ξ versus ε for the axisymmetric notched tensile specimen with $a_0/R_0 = 0.5$ and n ranging from 0 to 0.2; (b) Normalized curves of Fig. 11(a) by $\xi_{\varepsilon=0.8}$.

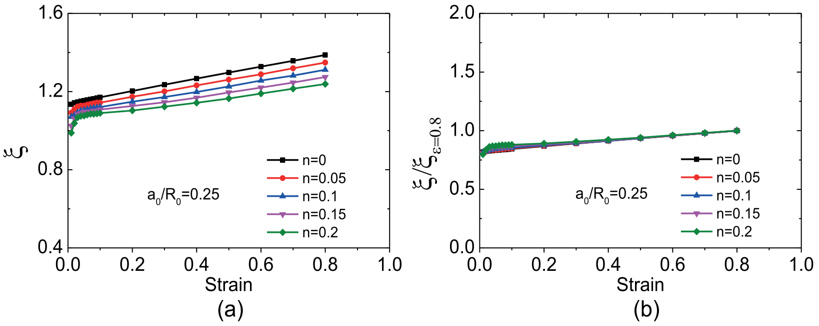

(a)

(b)

Fig. 12. (a) ξ versus ε for the axisymmetric notched tensile specimen with $a_0/R_0 = 0.25$ and n ranging from 0 to 0.2; (b) Normalized curves of Fig. 12(a) by $\xi_{\varepsilon=0.8}$.

Table 1
Parameters from linear fitting of Fig. 7(b)–12(b) by Eq. (10).

a_0/R_0	*Slope* $b_{1,n=0}$	*Intersection* $b_{2,n=0}$
3	−0.135	1.7597
2	−0.0194	1.5985
1.5	0.0529	1.4987
1	0.137	1.3799
0.5	0.2743	1.2299
0.25	0.3143	1.1376

strain hardening effect. With Eq. (15), the $\sigma_{T,notch} - \varepsilon$ curve from an axisymmetric notched tensile specimen can be converted to the material's equivalent stress-strain curve by Eq. (16). Therefore, Eq. (15) is the proposed correction function.

$$\sigma_{eq} = \frac{\sigma_{T,notch}}{\xi}\Big|_{\varepsilon} \tag{16}$$

It should be noted that the correction function Eq. (16) are derived based on notched specimens and are not accurate for $a_0/R_0 = 0$, namely the smooth round bar specimen. The extrapolated value (0.3866 for $a_0/R_0 = 0$) of Eq. (13) (see in Fig. 15(a)) is very close to the slope

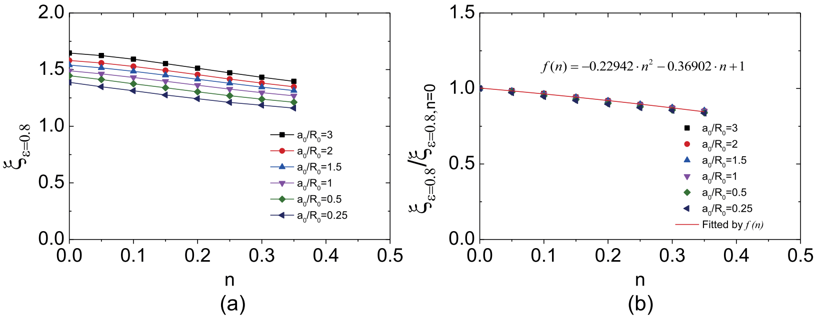

Fig. 13. (a) $\xi_{\varepsilon=0.8}$ versus n for axisymmetric notched tensile specimens with different notch geometries; (b) Normalized curves of Fig. 13(a) by $\xi_{\varepsilon=0.8,\,n=0}$ and are fitted by Eq. (7).

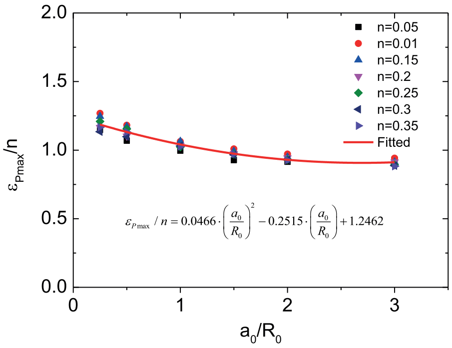

Fig. 14. Strain corresponding to the maximum load is normalized by hardening exponent and is plotted against the initial notch radius ratio.

(0.3718) by linearly fitting the ratio between the true stress-strain curve from smooth round bar specimen and the input stress-strain curve for the perfectly plastic material; while the extrapolated value (1.0577 for $a_0/R_0=0$) of Eq. (14) is very close to 1, giving reasonable indication that there is no stress concentration for smooth round bar specimen. However, the proposed correction function applies to the whole range of the $\sigma_{T,notch}-\varepsilon$ curve. For the smooth round bar specimen before diffuse necking, the true stress-strain curve is exactly the same as material's equivalent stress-strain curve and no correction is needed. Application of Eq. (15) to smooth round bar specimen may results in considerable error, especially when the strain is large.

5. Verification and discussion

To verify the proposed correction function, the axisymmetric notched tensile specimen with $a_0/R_0=1.25$ has been analyzed numerically. The equivalent stress-strain curves calculated by converting the true stress-strain curves from the axisymmetric notched tensile specimen with Eq. (16) are compared in Fig. 16 with the materials' equivalent stress-strain curves. Very satisfactory agreement can be seen in Fig. 16 for materials with $n=0$ and $n=0.125$. Compared with the well-known Bridgman correction method, the proposed correction function does not need to measure the current notch radius. Gromada et al. (2011) performed the Bridgman correction method with the perfectly plastic material numerically, and found that errors between the Bridgman corrected stress and the material's equivalent stress occurred quite early and increased to 10% at the strain $\varepsilon=1.25$. Compared with the Bridgman correction method, the proposed correction function yields accurate results for the perfectly plastic material, as can be seen in Fig. 16(a).

It should be noted that the conversion of the true stress-train curve from the axisymmetric notched tensile specimens to the material's equivalent stress-strain curve with the proposed correction function is

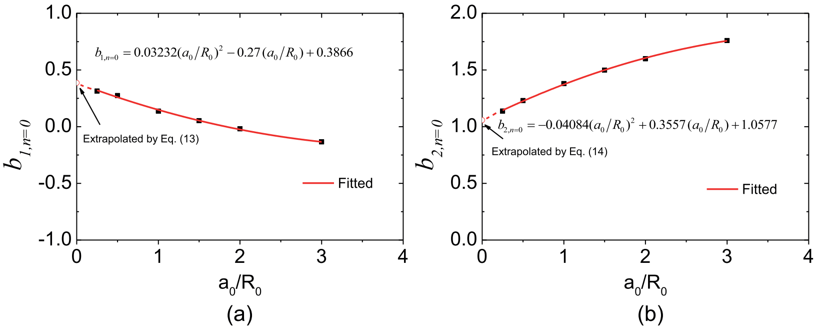

Fig. 15. (a) Slopes of linearly fitted equations of the $\xi-\varepsilon$ curves with $n=0$ in Fig. 7(a)–12(a) versus the initial notch radius ratio a_0/R_0; (b) Intersections of linearly fitted equations of the $\xi-\varepsilon$ curves for $n=0$ in Fig. 7(a)–12(a) versus the initial notch radius ratio a_0/R_0.

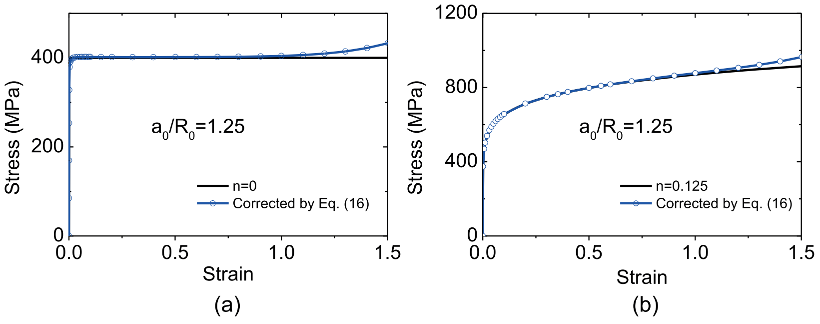

Fig. 16. Comparison of the equivalent stress-strain curve calculated by correcting the trues stress-strain curve from the axisymmetric notched tensile specimen with the proposed correction function and the material's equivalent stress-strain curve: (a) $n=0$; (b) $n=0.125$.

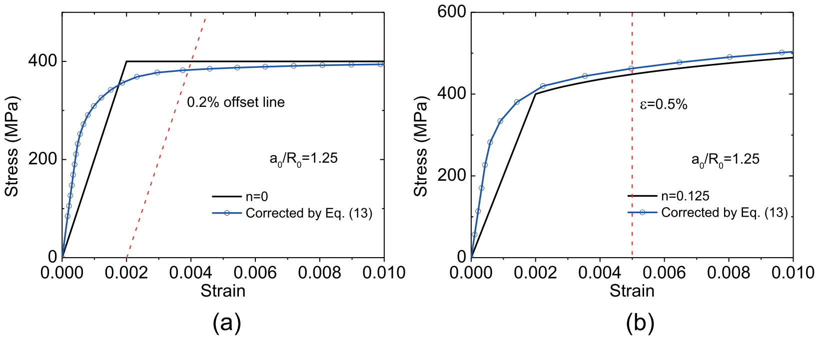

Fig. 17. Converted equivalent stress-strain curve by the proposed correction function at the strain less than 1% for materials with: (a) $n=0$; (b) $n=0.125$.

not perfect when the strain is very small. Fig. 16 is replotted by ranging strain from 0 to 0.01 in Fig. 17. Difference between the equivalent stress-strain curves converted by the proposed correction function and the material's equivalent stress-strain curves is shown in Fig. 17. One reason for the errors is that the normalized $\xi-\varepsilon$ curves in Fig. 7(b)–12(b) are linearly fitted, however, the normalized ξ deviates slightly to the linearly fitted equation in the initial stage. The second reason is that the transition of yielding for the notched tensile specimen is different to the smooth specimen. Yielding develops on the whole cross-section simultaneously for the smooth specimen, while the yielding for the axisymmetric notched tensile specimen develops firstly at part of the minimum cross-section. Gradual yielding of the axisymmetric notched tensile specimens also results in a smooth transition on the converted equivalent stress-strain curve, instead of a sharp transition in a smooth round bar specimen.

In practice, for tensile tests with smooth round bar specimen or rectangular cross-section specimen, the yield stress is determined by the intersection of the 0.2% offset line ($\sigma_{0.2}$) or the vertical line at the strain 0.5% ($\sigma_{0.5}$) on the equivalent stress-strain curve, for materials without obvious yield plateau [30]. In this study, both $\sigma_{0.2}$ and $\sigma_{0.5}$ are derived from both the corrected equivalent stress-strain curve and the material's equivalent stress-strain curve for all the analyses in Section 4, see in Fig. 17 as an example. The relative errors (absolute value) are presented in Table 2 for $\sigma_{0.2}$ and Table 3 for $\sigma_{0.5}$, respectively.

It can be seen that the values of the relative errors in Table 2 and Table 3 are within 5%, except the data marked in red which are mainly from the axisymmetric notched tensile specimen with $a_0/R_0=2$ and $a_0/R_0=3$ Therefore, it is not recommended to use very sharp axisymmetric notched tensile specimen to measure material's yield stress on the converted equivalent stress-strain curve with the proposed correction function.

Table 2
Absolute value of relative error of the 0.2% offset yield stress ($\sigma_{0.2}$).

n	a_0/R_0					
	0.25	0.5	1	1.5	2	3
0	0.018	0.013	0.025	0.05	0.08	0.121
0.05	0.005	0.008	0.018	0.046	0.049	0.083
0.1	0.008	0.011	0.008	0.032	0.064	0.101
0.15	0.03	0.031	0.011	0.016	0.044	0.078
0.2	0.046	0.045	0.027	0.023	0.021	0.049

Table 3
Absolute value of relative error of the yield stress at $\varepsilon=0.5\%$ ($\sigma_{0.5}$).

n	a_0/R_0					
	0.25	0.5	1	1.5	2	3
0	0.013	0.006	0.015	0.035	0.059	0.098
0.05	0.007	0.003	0.016	0.039	0.025	0.051
0.1	0.002	0.005	0.013	0.033	0.055	0.086
0.15	0.019	0.017	0	0.021	0.042	0.069
0.2	0.032	0.032	0.018	0.003	0.022	0.043

Since not all the materials follow power law hardening rule, the true stress-strain curves from smooth round bar specimen for steel

Table 4
Error analysis for the application of the proposed correction function.

Material	Failure strain	a_0/R_0	$\varepsilon_{P\max}$	Error
20MnMoNi55	1.1	3	0.091	1.02%
		2	0.095	0.98%
		1.5	0.097	1.81%
		1	0.102	3.11%
		0.5	0.115	1.58%
		0.25	0.12	4.75%
AISI 304	1.33	3	0.212	7.16%
		2	0.225	3.98%
		1.5	0.236	2.34%
		1	0.253	1.36%
		0.5	0.273	3.17%
		0.25	0.275	2.32%
FE 430	1.1	3	0.16	4.04%
		2	0.169	2.59%
		1.5	0.176	1.57%
		1	0.188	1.31%
		0.5	0.199	0.04%
		0.25	0.2	2.6%

20MnMoNi 55 [16], AISI 304 and FE 430 [17] have been used to verify the correction function. The true stress-strain curves are expressed as Eq. (17)-(19) and are converted to equivalent stress-strain curves with the so-called MLR method introduced in [16]. The correction factor for the MLR method can be expressed as Eq. (20):
For steel 20MnMoNi 55:

$$\sigma_T = \begin{cases} 828 \cdot \varepsilon^{0.1} & \text{for } (0 < \varepsilon \leq 0.1) \\ 614 + 460 \cdot \varepsilon & \text{for } (\varepsilon > 0.1) \end{cases} \tag{17}$$

For steel AISI 304:

$$\sigma_T = \begin{cases} 1183 \cdot \varepsilon^{0.25} & \text{for } (0 < \varepsilon \leq 0.25) \\ 693 + 592 \cdot \varepsilon & \text{for} (\varepsilon > 0.25) \end{cases} \tag{18}$$

For steel FE 430:

$$\sigma_T = \begin{cases} 818 \cdot \varepsilon^{0.19} & \text{for } (0 < \varepsilon \leq 0.19) \\ 527 + 365 \cdot \varepsilon & \text{for } (\varepsilon > 0.19) \end{cases} \tag{19}$$

$$MLR\sigma(\varepsilon, \varepsilon_N) = 1 - 0.6058(\varepsilon - \varepsilon_N)^2 + 0.6317(\varepsilon - \varepsilon_N)^3 - 0.2107(\varepsilon - \varepsilon_N)^4 \tag{20}$$

where ε_N is the true strain at diffuse necking, which can be found in ref. [16] and [17]. By multiplying the true stress with the MLR correction factor, the equivalent stress-strain curve can be derived after diffuse necking. It should be noted that the error induced by the MLR is not considered here. The equivalent stress-strain curves converted by the MLR method are then converted to flow stress-strain curves and are input for numerical analyses with different axisymmetric notched tensile specimens. True stress-strain curves from the numerical analyses are then corrected with the proposed correction function, Eq. (15), up to the same failure strain as in ref. [16] and [17]. Results of the corresponding equivalent stress-strain curves converted by the proposed correction function from numerical analyses as well as the MLR converted equivalent stress-strain curves are presented in Fig. 18. For the application of Eq. (15), the true strain at the maximum tensile load is obtained from the force-true strain curve for each material and each specimen geometry and is presented in Table 4.

As can be seen in Fig. 18, the equivalent stress-strain curves derived from the axisymmetric notched tensile specimens with the proposed correction function agree well with the MLR corrected equivalent stress-strain curves, except small deviations. It can also be noted that difference occurs when the strain is large in Fig. 18. Errors between the equivalent stress-strain curves from notched specimens and from the MLR corrected equivalent stress-strain curves are listed in Table 4. It can be seen that most of the errors are within 5%, except the one for steel AISI 304 with $a_0/R_0 = 3$. It can also be observed that the strain at the maximum tensile load deviates slightly from the strain at necking from smooth round bar specimen.

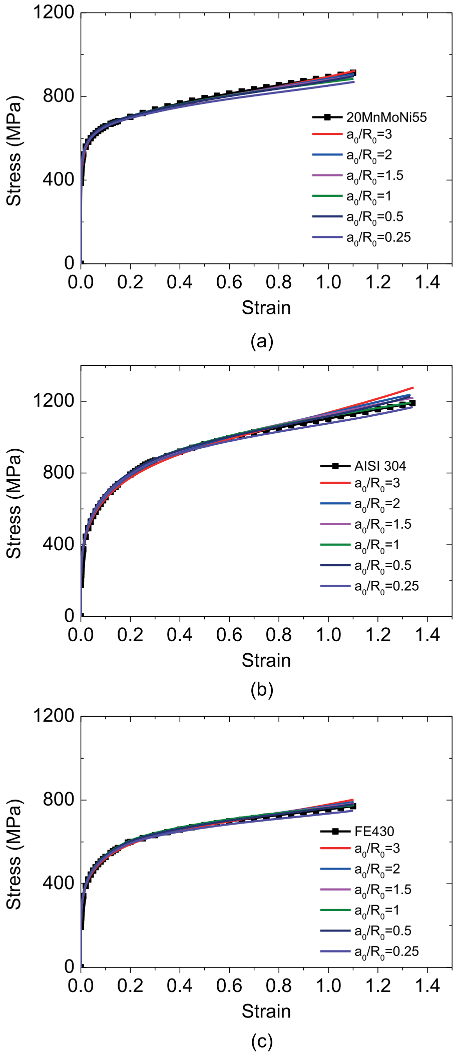

(a)
(b)
(c)

Fig. 18. Comparison of the equivalent stress-strain curves calculated by correcting the trues stress-strain curves from the axisymmetric notched tensile specimens with the proposed correction function and the MLR corrected equivalent stress-strain curve: (a) 20MnMoNi 55; (b) AISI 304; (c) FE 430.

Fig. 19 presents the results of the equivalent stress-strain curves by correcting the true stress-strain curves from notched specimens with Eq. (15), together with the reference equivalent stress-strain curve for material D98 in ref. [19]. The true stress-strain curves are calculated numerically. The reference equivalent stress-strain curve in ref. [19] was derived by correcting true stress-strain curve from smooth round bar

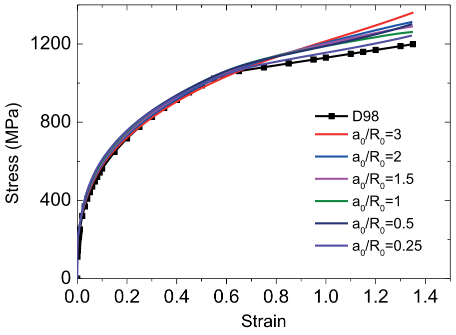

Fig. 19. Comparison of the equivalent stress-strain curves calculated from the axisymmetric notched tensile specimens with the proposed correction function and the equivalent stress-strain curve from Ref. [19].

specimen with Bridgman correction method and expressed as:

$$\sigma_{eq} = \begin{cases} 1260 \cdot \varepsilon^{0.35} & \text{for } (0 < \varepsilon \leq 0.55) \\ 933 + 197 \cdot \varepsilon & \text{for } (\varepsilon > 0.65) \end{cases} \tag{21}$$

Tensile test with smooth round bar specimen in ref. [19] shows that diffuse necking occur at strain $\varepsilon = 0.35$ for this D98 material. The authors in [19] performed numerical analysis with smooth round bar specimen, using Eq. (21) as the input equivalent stress-strain curve. True stress-strain curve from numerical analysis was then corrected with Bridgman correction. They found that the equivalent stress-strain curve corrected by the Bridgman correction from numerical analysis differed with the input equivalent stress-strain curve at large strain. The error reaches up to 10.6% at the strain $\varepsilon = 1.35$. As can be seen in Fig. 19, the equivalent stress-strain curves corrected by Eq. (16) are higher than the reference curve when the strain is larger than 0.7. The errors at the strain $\varepsilon = 1.35$ range from 3.68% to 13.52%. It can also be noticed that notched specimen with larger a_0/R_0 shows larger deviation with the reference curve.

It should be noted that notched specimen fails at smaller strain than smooth round bar specimen. The sharper (larger a_0/R_0) the notch is, the smaller the failure strain will be. This is due to the reason that the failure strain depends significantly on the stress triaxiality, which is the ratio of mean stress and Mises equivalent stress. Sharper notch corresponds to a higher stress triaxiality, resulting in a smaller failure strain. In order to obtain equivalent stress-strain curve in larger strain and considering the error analysis, we recommend to use notched specimen with smaller a_0/R_0 for the application of the proposed correction function.

The proposed correction function can also be applied to determine the equivalent stress-strain curve of each individual material zone in a weldment. By locating the notch either in the base material, weld metal, or possibly in the heat affected zone, the material's equivalent stress-strain curve in the notched region as shown in Fig. 1 can be determined with the proposed correction function, once the geometry conditions ($d_0 \geq 3.5a_0$; $a_0 \leq H$) are fulfilled.

By summarizing the results above, a recommended procedure is proposed to determine material's equivalent stress-strain curve with an axisymmetric notched tensile specimen:

1. Prepare the axisymmetric notched tensile specimen under the geometry requirements: $d_0 \geq 3.5a_0$, $a_0 \leq H$;
2. Perform tensile test with the axisymmetric notched tensile specimen, record the load and the minimum cross section diameter;
3. Calculate the $\sigma_{T,notch} - \varepsilon$ curve and the $\sigma_{e,notch} - \varepsilon$ curve, determine $\varepsilon_{P\max}$ on the $\sigma_{e,notch} - \varepsilon$ curve;
4. With the data of the initial notch radius ratio a_0/R_0 and $\varepsilon_{P\max}$, convert the $\sigma_{T,notch} - \varepsilon$ curve by Eq. (16) to derive the material's equivalent stress-strain curve.

6. Conclusions

Recently, we identified a so-called 'magic' special axisymmetric notched tensile specimen to derive material's flow stress-strain curve for hardening material [21]. In this study, we proposed a correction function by performing a series of numerical analyses with axisymmetric notched tensile specimens. With the proposed correction function, the true stress-strain curve from any axisymmetric notched tensile specimen can be converted to the material's equivalent stress-strain curve and no Bridgman correction is needed. Accordingly, a recommended procedure to determine the material's equivalent stress-strain curve with the axisymmetric notched tensile specimens is proposed. The proposed procedure can be used to hardening materials, as well as perfectly plastic material. Furthermore, the proposed procedure can be applied to both homogeneous material and inhomogeneous materials (such as the weldment), by locating the notch in the target material zone under the geometry requirements ($d_0 \geq 3.5a_0$, $a_0 \leq H$). The proposed procedure is cheap and accurate, since the only information needed to record during the tensile test is load and minimum cross section area (radius).

Acknowledgement

The Chinese Scholarship Council is greatly acknowledged for the financial support. The authors wish to thank the Research Council of Norway for funding through the Petromaks 2 Programme, Contract No.228513/E30.

References

[1] Andrade Pires FM, César de Sá JMA, Costa Sousa L, Natal Jorge RM. Numerical modelling of ductile plastic damage in bulk metal forming. Int J Mech Sci 2003;45:273–94.
[2] Badr OM, Barlat F, Rolfe B, Lee M-G, Hodgson P, Weiss M. Constitutive modelling of high strength titanium alloy Ti-6Al-4V for sheet forming applications at room temperature. Int J Solids Struct 2016;80:334–47.
[3] Zhang ZL, Thaulow C, Ødegård J. A complete Gurson model approach for ductile fracture. Eng Fract Mech 2000;67:155–68.
[4] Zhang ZL. A sensitivity analysis of material parameters for for the Gurson constitutive model. Fatigue Fract Eng Mater Struct 1996;19:561–70.
[5] Xu J, Zhang ZL, Østby E, Nyhus B, Sun DB. Constraint effect on the ductile crack growth resistance of circumferentially cracked pipes. Eng Fract Mech 2010;77:671–84.
[6] Xu J, Zhang ZL, Østby E, Nyhus B, Sun DB. Effects of crack depth and specimen size on ductile crack growth of SENT and SENB specimens for fracture mechanics evaluation of pipeline steels. Int J Press Vessels Pip 2009;86:787–97.
[7] Dunbar A, Wang X, Tyson WR, Xu S. Simulation of ductile crack propagation and determination of CTOAs in pipeline steels using cohesive zone modelling. Fatigue Fract Eng Mater Struct 2014;37:592–602.
[8] Zhang ZL, Hauge M, Ødegård J, Thaulow C. Determining material true stress-strain curve from tensile specimens with rectangular cross-section. Int J Solids Struct 1999;36:3497–516.
[9] Scheider I, Brocks W, Cornec A. Procedure for the determination of true stress-strain curves from tensile tests with rectangular cross-section specimens. J Eng Mater Technol 2004;126:70–76..
[10] Joun M, Eom JG, Lee MC. A new method for acquiring true stress–strain curves over a large range of strains using a tensile test and finite element method. Mech Mater 2008;40:586–593..
[11] Zhang ZL, Ødegård J, Søvik OP. Determining true stress-strain curve for isotropic and anisotropic materials with rectangular tensile bars: method and verifications. Comput Mater Sci 2001;20:77–85.
[12] Yuan WJ, Zhang ZL, Su YJ, Qiao LJ, Chu WY. Influence of specimen thickness with rectangular cross-section on the tensile properties of structural steels. Mater Sci Eng: A 2012;532:601–605..
[13] Zhang ZL, Hauge M, Thaulow C, Ødegård J. A notched cross weld tensile testing method for determining true stress–strain curves for weldments. Eng Fract Mech 2002;69:353–66.
[14] Choung J. Comparative studies of fracture models for marine structural steels. Ocean Eng 2009;36:1164–74.
[15] Gromada M, Mishuris G. Andreas, correction formulae for the stress distribution in round tensile specimens at neck presence. Springer; 2011.
[16] Mirone G. A new model for the elastoplastic characterization and the stress–strain determination on the necking section of a tensile specimen. Int J Solids Struct 2004;41:3545–64.
[17] Mirone G, Corallo D. A local viewpoint for evaluating the influence of stress triaxiality and Lode angle on ductile failure and hardening. Int J Plast 2010;26:348–71.
[18] Bridgman PW. Studies in large plastic flow and fracture. New York: MaGraw-Hill; 1952.

[19] La Rosa G, Mirone G, Risitano A. Postnecking elastoplastic characterization degree of approximation in the bridgman method and properties of the flow stress true stress ratio. Metall Mater Trans A 2003;34:615–24.

[20] Bao Y. Dependence of ductile crack formation in tensile tests on stress triaxiality, stress and strain ratios. Eng Fract Mech 2005;72:505–22.

[21] Tu S, Ren X, Nyhus B, Akselsen OM, He J, Zhang ZL. A special notched tensile specimen to determine the flow stress-strain curve of hardening materials without applying the Bridgman correction. Eng Fract Mech 2017;179:225–39.

[22] Børvik T, Hopperstad OS, Berstad T. On the influence of stress triaxiality and strain rate on the behaviour of a structural steel. Part II. Numerical study. Eur J Mech A Solids 2003;22:15–32.

[23] Børvik T, Hopperstad OS, Dey S, Pizzinato EV, Langseth M, Albertini C. Strength and ductility of Weldox 460 E steel at high strain rates, elevated temperatures and various stress triaxialities. Eng Fract Mech 2005;72:1071–87.

[24] Hopperstad OS, Børvik T, Langseth M, Labibes K, Albertini C. On the influence of stress triaxiality and strain rate on the behaviour of a structural steel. Part I. Experiments. Eur J Mech A Solids 2003;22:1–13.

[25] Yu H, Olsen JS, Alvaro A, Olden V, He J, Zhang ZL. A uniform hydrogen degradation law for high strength steels. Eng Fract Mech 2016;157:56–71.

[26] Bao Y, Wierzbicki T. On fracture locus in the equivalent strain and stress triaxiality space. Int J Mech Sci 2004;46:81–98.

[27] Bao Y, Wierzbicki T. On the cut-off value of negative triaxiality for fracture. Eng Fract Mech 2005;72:1049–69.

[28] Yu H, Olsen JS, He J, Zhang ZL. Effects of loading path on the fracture loci in a 3D space. Eng Fract Mech 2016;151:22–36.

[29] Zhang ZL, Hauge M, Thaulow C. Two parameter characterization of the near-tip stress field for a bi-material elastic-plastic interface crack. Int J Fract 1996;79:65–83.

[30] ASTM E8/E8M-16a. Standard test method for tension test of metallic materials, in. West Conshohocken, PA: ASTM International; 2016.

A.3

Paper III

Experimental measurement of temperature-dependent equivalent stress-strain curve of a 420 MPa structural steel with axisymmetric notched tensile specimens

Authors: Shengwen Tu; Xiaobo Ren; Jianying He; Zhiliang Zhang

Submitted

A.4

Paper IV

Study of low-temperature effect on the fracture locus of a 420-MPa structural steel with the edge tracing method

Authors: Shengwen Tu; Xiaobo Ren; Tore Andre Kristensen; Jianying He; Zhiliang Zhang

Fatigue & Fracture of Engineering Materials & Structures. vol. 41 (8)

The final published version is available at https://doi.org/10.1111/ffe.12803

Study of low temperature effect on the fracture locus of a 420 MPa structural steel with the edge tracing method

S. Tu[1], X. Ren[2], T. A. Kristensen[2], J. He[1], Z. Zhang [1,*]

[1]Department of Structural Engineering, Norwegian University of Science and Technology, Trondheim 7491, Norway

[2]SINTEF Materials and Chemistry, Trondheim 7456, Norway

Abstract

Quasi-static tensile tests with smooth round bar and axisymmetric notched tensile specimens have been performed to study the low temperature effect on the fracture locus of a 420 MPa structural steel. Combined with a digital high-speed camera and a two-plane mirrors system, specimen deformation was recorded in two orthogonal planes. Pictures taken were then analyzed with the edge tracing method to calculate the minimum cross-section diameter reduction of the necked/notched specimen. Obvious temperature effect was observed on the load-strain curves for smooth and notched specimens. Both the strength and strain hardening characterized by the strain at maximum load increase with temperature decrease down to -60℃. Somewhat unexpected, the fracture strains (ductility) of both smooth and notched specimens at temperatures down to -60℃ do not deteriorate, compared with those at room temperature. Combined with numerical analyses, it shows that the effect of low temperatures (down to -60℃) on fracture locus is insignificant. These findings shed new light on material selection for Arctic operation.

Keywords: *fracture locus; low temperature; notched tensile specimen; edge tracing method; stress triaxiality.*

1. Introduction

The increasing demands of energy motivate the petroleum sector to move their exploitation activities to harsher environments, resulting in new challenges for structural design, maintenance, and failure assessment. It has been demonstrated that there are considerable oil and gas resources in the Arctic region [1], the low temperature effect should be considered in the selection of structural steels. Previous research has shown that decreasing temperature increases the yield strength of most steels. Ren [2] carried out tensile tests of a 420 MPa steel with temperature ranging from 0℃ down to -90℃, and found that the Lüders strain [3-5] increased as the temperature decreased. For most structural steels, as the temperature decreases continuously, the fracture behavior will transform from ductile to brittle (DBT) [6-12], reducing the steels' ductility and fracture toughness. The DBT occurs when the temperature decreases down to the steel's DBT temperature.

Hybrid experimental-numerical analyses [13-18] or numerical analyses with unit cell model [19, 20] alone have demonstrated that the fracture strain ε_f (the equivalent strain corresponding to crack initiation) strongly depends on the stress triaxiality and the Lode angle parameter. The stress triaxiality T which is defined by the ratio of the mean stress σ_m and the von Mises equivalent stress σ_{eq} ($T = \sigma_m / \sigma_{eq}$) is widely used to characterize the hydrostatic pressure effect [21-25] and crack tip constraint level [26-28]. Bao [13] carried out a series of tests on 2024-T351 aluminum alloy with initial stress triaxiality ranging from -0.33 to 1 at room temperature. Combined with numerical analyses, a fracture strain versus strain-weighted average stress triaxiality T^* diagram was established. The curve, namely the fracture locus consists of three branches: the fracture strain decreases with the increase of T^* when $-0.33 < T^* < 0$ and $T^* > 0.33$; while the fracture strain increases in the range $0 \le T^* \le 0.33$. Recent study shows that the Lode angle parameter L ($L = (2\sigma_2 - \sigma_1 - \sigma_3)/(\sigma_1 - \sigma_3)$; σ_1 , σ_2 , σ_3 are the principle stresses) also plays an important role on the evolution of fracture locus [16, 19, 29-32]. For smooth round bar and axisymmetric notched specimens under quasi-static tensile loading, which are the focus of this study, the Lode angle parameter at a given material point on the minimum cross-section is constant [32, 33], and therefore will not be discussed here. The influence of loading rate [18, 22], loading path [19, 20, 31, 34] on the evolution of the fracture locus have been studied extensively in the range of the stress triaxiality $T > 0.33$. Johnson and Cook [22] performed torsion tests over a range of strain rates, Hopkinson bar tests over a range of temperatures and quasi-static tensile tests with various notch geometries to investigate fracture characteristics of OFHC copper, Armco iron and 4340 steel. Their test results indicate that fracture strain is very dependent on stress triaxiality and less dependent on strain rate and temperature. Hopperstad and Børvik [18, 35, 36] performed Split Hopkinson tension tests on the structural steel Weldox 460E at high strain rates and elevated temperatures (100 to 500℃) with smooth and axisymmetric notched specimens, neither obvious strain rate effect nor temperature dependence on the fracture locus was observed.

Fracture locus of metallic materials has attracted wide attention over the past decades, however, the study on the effect of low temperature on fracture locus is very limited. In order to facilitate the selection of structural steels for the application in the Arctic region, it is very important to characterize the low temperature effect on fracture locus of structural steels.

In the current study, we carried out quasi-static tensile tests with smooth and axisymmetric notched specimens made of a 420 MPa structural steel, with temperature varied from room temperature down to -60℃. A digital high-speed camera was used to record the specimen deformation during the test in conjunction with a two-plane mirrors system. Pictures taken were then analyzed with the edge tracing method to calculate the global average strain, up to crack initiation. Detailed information about the test materials, test set-up and the edge tracing method are introduced in section 2. Experimental results are presented in section 3. Numerical analyses are performed to simulate the experiments to capture the stress triaxiality evolution at the location where crack initiation is supposed to occur. The numerical procedure and results are presented in section 4. The results indicate that both the strength and hardening characterized by the strain at maximum load increase with the decrease of temperature, while the temperature down to -60℃ does not significantly alter the dependence of fracture strain on stress triaxiality.

2. Experimental program

2.1 Material and specimens

The specimens were machined from 50 mm thick plates of a 420 MPa steel, along the rolling direction. Sketches of the smooth round bar specimens and axisymmetric notched tensile specimens are shown in Fig. 1. Bridgman [21] proposed an analytic solution to characterize the stress distribution of a necked tensile specimen, the stress triaxiality in the center of the minimum cross section where crack formation occurs first is expressed as:

$$T = \frac{1}{3} + \ln(1 + \frac{a}{2R}) \tag{1}$$

where a and R are the current minimum cross-section radius and the notch curvature radius of a necked tensile specimen, respectively. Bao performed tensile test with smooth round bar specimen numerically, and found that the stress distribution differed significantly with Bridgman's analytical solution on the minimum cross-section. Based on numerical simulation, an empirical expression of stress triaxiality in the center of specimen minimum cross-section was proposed [33, 37]:

$$T = \frac{1}{3} + \sqrt{2}\ln(1 + \frac{a}{2R}) \tag{2}$$

According to Eq. (1) and Eq. (2), the stress triaxiality in the center of specimen minimum cross-section is a function of the notch radius ratio a/R. By machining axisymmetric notch in the center of smooth specimen, different initial stress triaxiality can be realized by varying the initial notch radius ratio, a_0/R_0. For all the axisymmetric notched specimens tested in present study, $a_0 = 6\,\text{mm}$. a_0/R_0 varied from 0.5 to 3 by varying R_0 from 2 mm to 12 mm. Combined with the smooth round bar specimen, the initial stress triaxiality varied in a range from 0.33 to 1.63, calculated by Eq. (2).

(a)

(b)

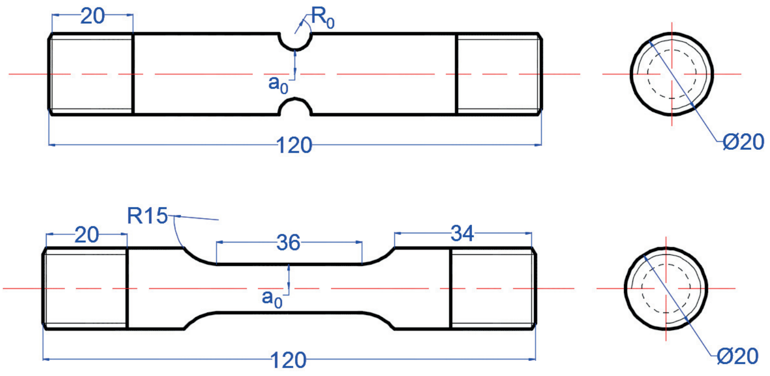

Fig. 1 Sketches of the tensile Specimens: (a) axisymmetric notched tensile specimen; (b) smooth round bar specimen.

2.2 Test set-up

The test set-up is shown in Fig. 2. The tests were carried out using an universal test machine **Instron 5985,** with the loading cell of 250 KN. A liquid nitrogen-cooled temperature chamber was used to create low temperature environment. The tests were carried out at room temperature, -30℃, and -60℃. The air inside of the temperature chamber was replaced with nitrogen gas first, in order to avoid ice formation on the specimen surface. A thermocouple shown in Fig. 3 (a) was used to measure the temperature at the specimen surface. On one side of the temperature chamber, there is a window, through which the inside of the temperature chamber can be observed clearly. A digital high-speed CCD camera with the resolution of 2448×2050 pixels was located besides the window to take pictures of the specimen during the test, with the framing rate of 1 frame per second. All the tests were performed in displacement control manner, with the crosshead speed of 0.3 mm/minute. During the tests, the force was recorded with the same camera framing frequency

Inside the temperature chamber, there are two LED lights and a two-plane mirrors system, as seen in Fig. 3. The two-plane mirrors system consists of 2 plane mirrors with the angle of 135°, as illustrated in Fig. 3 (b). The specimen and the camera located on the angle bisector of the two-plane mirrors system. According to the plane image formation principle, the specimen images form in two orthogonal planes, seen in Fig. 3 (b). Therefore, the deformation of the specimen can be observed in two perpendicular directions during the test. The consideration of using the two-plane mirrors system is that, due to the localized deformation on necked smooth and axisymmetric notched specimens, it is more accurate to use the average value of minimum cross-section diameter in two orthogonal directions to calculate the current minimum cross-section area, instead of only one direction [36]. By adjusting the position of the LED lights, the specimen images can be located in the LED light images center. The camera was set in mono mode in the test. A very strong grey-value gradient can be formed between the specimen images and the picture background, for the purpose to use the edge tracing method to measure the specimen deformation. Fig. 4 shows a picture of a smooth specimen taken with the camera in the beginning of the test.

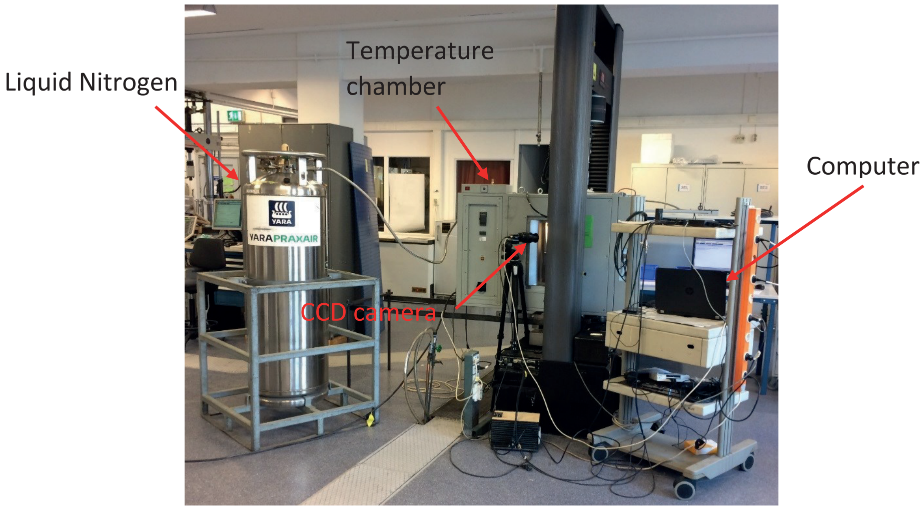

Fig. 2 Test system in this study

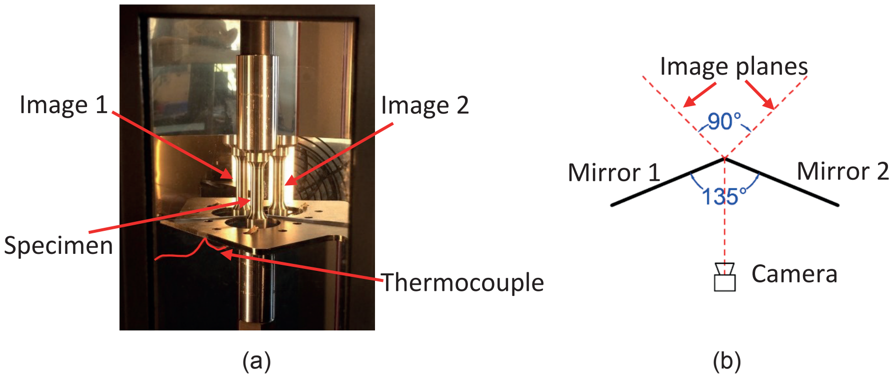

Fig. 3 (a) Layout of the inside of temperature chamber; (b) Illustration of the two-plane mirrors system.

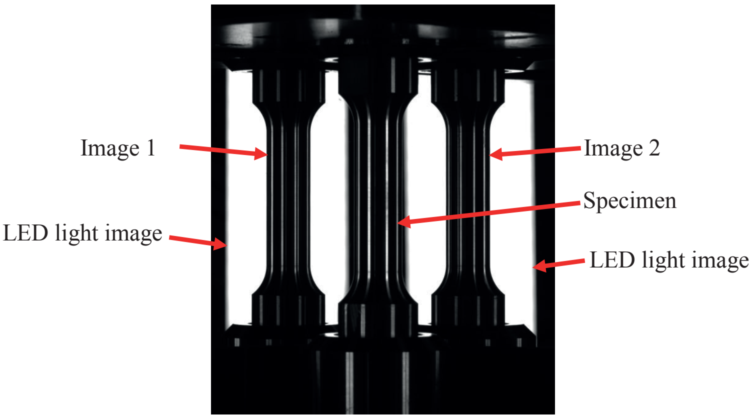

Fig. 4 Picture of smooth round bar specimen taken at the beginning of the test.

2.3 The edge tracing method

Digital pictures consists of numbers of pixels which depend on the resolution of the digital camera [38]. Each pixel in the picture represents a grey-value. From black to white, the grey-value ranges from 0 to 255. Digital pictures can be read by Matlab and grey-value of each pixel can be output and stored in a matrix for analysis. For one arbitrary row in the digital pictures as red line marked in Fig. 5 (a), peak values of the derivative (absolute value) of grey-value can be found, due to the strong contrast between the specimen images and the background, as shown in Fig. 5 (b). There were several peak values in Fig. 5 (b), however, only the two maximum peak values were regarded as the boundaries between the specimen image and the background. The small peak values were caused by the white color on the specimen image, formed due to light reflection. The pixel numbers between the two boundaries represent the corresponding cross-section diameter. By scanning each row of the picture, the edges of the specimen image can be captured, together with the minimum cross-section diameter, shown as red curves in Fig. 6. Due to the existence of necking or notch, the deformation was localized in the necking /notch region. The edge tracing method was therefore mainly focused on the necking/notch region to save calculation cost.

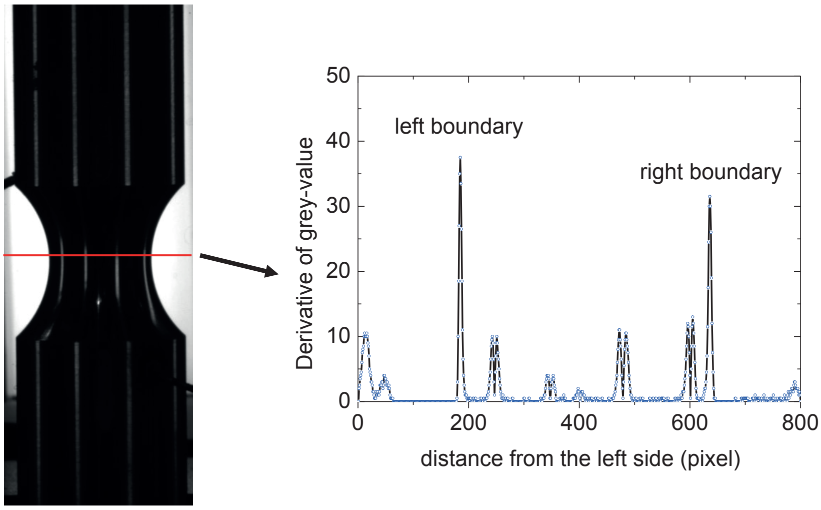

(a) (b)

Fig. 5 The edge tracing method. (a) One arbitrary row of pixels of axisymmetric notched specimen with $a_0/R_0 = 0.5$ *; (b) absolute value of derivative of the grey-value.*

Fig. 6 Specimen image edges in Fig. 5 (a) derived with the edge tracing method. The minimum cross-section diameter is also shown in pixels.

Before the test, the minimum cross-section diameter of each specimen was measured with a laser gauge. The ‘unit pixel length’ then can be calculated by dividing the initial minimum cross-section diameter by the corresponding pixel numbers in the picture taken in the beginning. The current minimum cross-section diameters are calculated by multiplying the pixel numbers and the 'unit pixel length' in all the following pictures taken during the test. In order to verify the accuracy of the edge tracing method, several trial tests with notched specimens were performed. After certain deformation, we held the test and took a picture of the specimen. Then the minimum cross-section diameter in the same directions as in the picture was measured by the laser gauge. The picture was analyzed with the edge tracing method. The minimum cross-section diameter calculated from the picture agreed well with the value measured by the laser gauge in the same direction, with errors within $\pm 1.2\ \%$. The trial tests confirmed that the edge tracing method can be used to measure the specimen minimum cross-section diameter accurately. A difference of the minimum cross-section diameters measured in the two perpendicular directions has been observed, from both the edge tracing method and the laser gauge measurement. For example, for the axisymmetric notched specimen with $a_0/R_0 = 0.5$, the minimum cross-section diameters measured were 8.05 and 8.23 mm, at the load $P = 54.33\ KN$. This is attributed to the material anisotropy and anisotropic damage evolution. Therefore, it is more accurate to use the average value of diameters measured in two orthogonal planes in minimum cross-section to characterize the diameter reduction. For all the pictures taken in each test, the edge tracing method was used to detect the specimen image edges and to measure the corresponding average minimum cross-section diameter.

3. Experimental results

In this study, the specimen deformation is characterized by the average true strain ε, which is defined by the minimum cross-section area reduction [39]:

$$\varepsilon = \ln(A_0/A) = 2\ln(a_0/a) \tag{3}$$

where A_0 and A are the initial and current minimum cross-section area, respectively. a is the current averaged minimum cross-section radius measured from the specimen images with the edge tracing method. True stress σ_t for the smooth round bar specimen is calculated by dividing load by the current minimum cross-section area:

$$\sigma_t = P/\pi a^2 \tag{4}$$

Deformed plots of the smooth round bar specimen tested at room temperature and axisymmetric notched specimen with $a_0/R_0 = 0.5$ tested at -60°C are presented in Fig. 7 and Fig. 8, respectively. For the smooth round bar specimen in Fig. 7, the deformation developed in the whole specimen when the strain is small. As the load increases, diffuse necking occurred, which can be observed on the specimen image in Fig. 7. By studying the specimen images and the load-strain curves, it was found that diffuse necking occurred approximately at the strain $\varepsilon = 0.1$ for tests performed at room temperature. For the smooth specimen tested at low temperatures, the strain corresponding to diffuse necking increased slightly as temperature decreased, seen in Fig. 9 (a). After diffuse necking, the deformation localized in the necking zone, and a blunt axisymmetric notch was formed. The blunt notch became sharper and sharper, until the specimen failed into two parts. For the axisymmetric notched specimen, deformation localized mainly in the notch region. As the strain increases, the notch deformed form an initial 'U' shape to a 'V' shape, until the specimen failed into two parts, as seen in Fig. 8. For the first picture in which the specimen failure (broken into two parts) was observed in each test, specimen images in the previous frames were used to calculate the strain with the edge tracing method. Note that, in Fig. 7 and Fig. 8, the picture annotated by $\varepsilon = \varepsilon_f$ corresponds to crack initiation, instead of measuring after the complete fracture. This will be discussed in the following section.

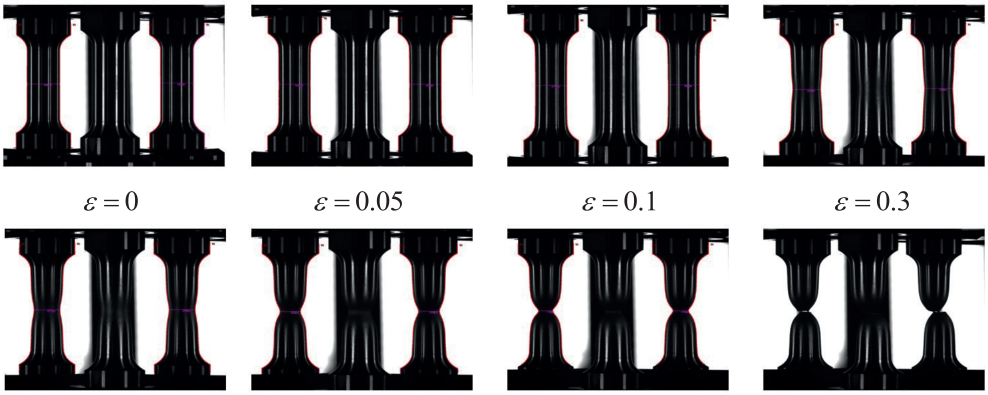
$\varepsilon = 0$ $\varepsilon = 0.05$ $\varepsilon = 0.1$ $\varepsilon = 0.3$

$\varepsilon = 0.5$ $\varepsilon = 1$ $\varepsilon = \varepsilon_f$ *fractured*

Fig. 7 Smooth specimen at different deformation level tested at room temperature.

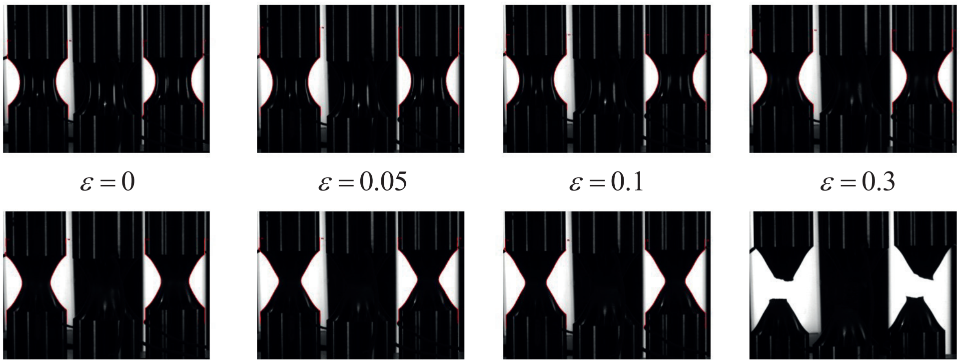
$\varepsilon = 0$ $\varepsilon = 0.05$ $\varepsilon = 0.1$ $\varepsilon = 0.3$

$\varepsilon = 0.5$ $\varepsilon = 1$ $\varepsilon = \varepsilon_f$ *fractured*

Fig. 8 Axisymmetric notched specimen with $a_0/R_0 = 0.5$ at different deformation levels tested at -60℃.

The load-strain curves and true stress-stain curves of the smooth round bar specimens tested at different temperatures are presented in Fig. 9. As expected, the load increased to a maximum value and then decreased, up to specimen failed. The true stress increases with the decrease of test temperature at the same strain. It can be seen that the maximum load and the strain at the maximum load, $\varepsilon_{P_{\max}}$, increase with the decrease of the test temperature. At the end of the load-strain curves, a sudden drop of load which indicates specimen load carrying capacity loss can be found [13]. This point is regarded as the crack initiation and the corresponding strain is defined as fracture strain, ε_f . It has been pointed out by Benzerga [34] that the strain at crack initiation is smaller than the strain measured from broken specimen fracture surface. The difference is induced due to the server deformation after crack initiation. It is evident in Fig. 9 that the fracture strain ε_f of the smooth round bar specimen increases slightly as temperature decreases. Usually, for most structural steels, decreasing test temperature increases material's strength and hardening, while material's ductility is reduced. Michael and Richard [40] performed quasi-static tensile tests with smooth round bar from 25℃ to 150℃. The specimens were cut from an Al-Cu-Mg-Ag alloy sheet. They found that fracture strain for smooth round bar specimen increased with test temperature increase. Quasi-static tensile test conducted by Børvik and Hopperstad [41] at temperature from 20℃ to 500℃ showed that fracture strain for smooth round bar specimen of Weldox 460 E steel was independent of temperature from 20℃ to 300℃; while from 300℃ to 500℃, fracture strain increased with temperature increase. It is very interesting that the ductility for this 420 MPa structural steel indeed increases (slightly) with decreasing test temperature (down to -60℃). The reason may be that the fracture strain here is defined at crack initiation, instead of strain at the complete fracture of specimens.

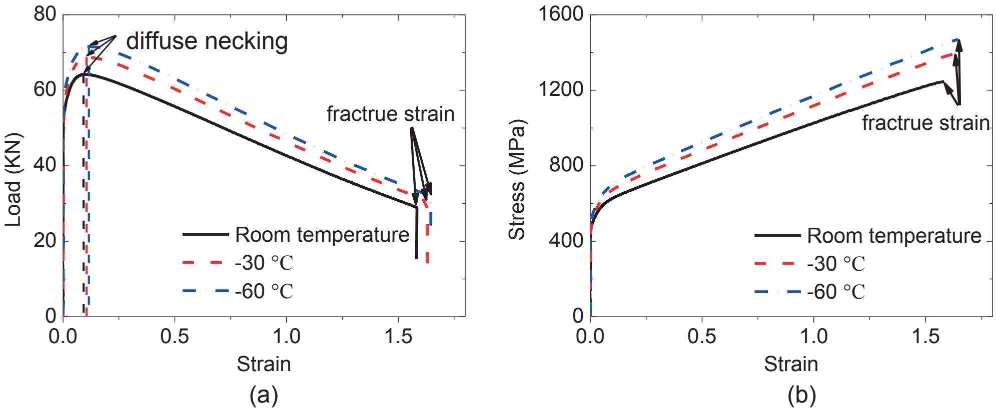

Fig. 9 (a) Load-strain curves of smooth round bar specimen. (b) True stress-strain curves of smooth round bar specimen. The strain corresponding to diffuse necking and fracture are annotated.

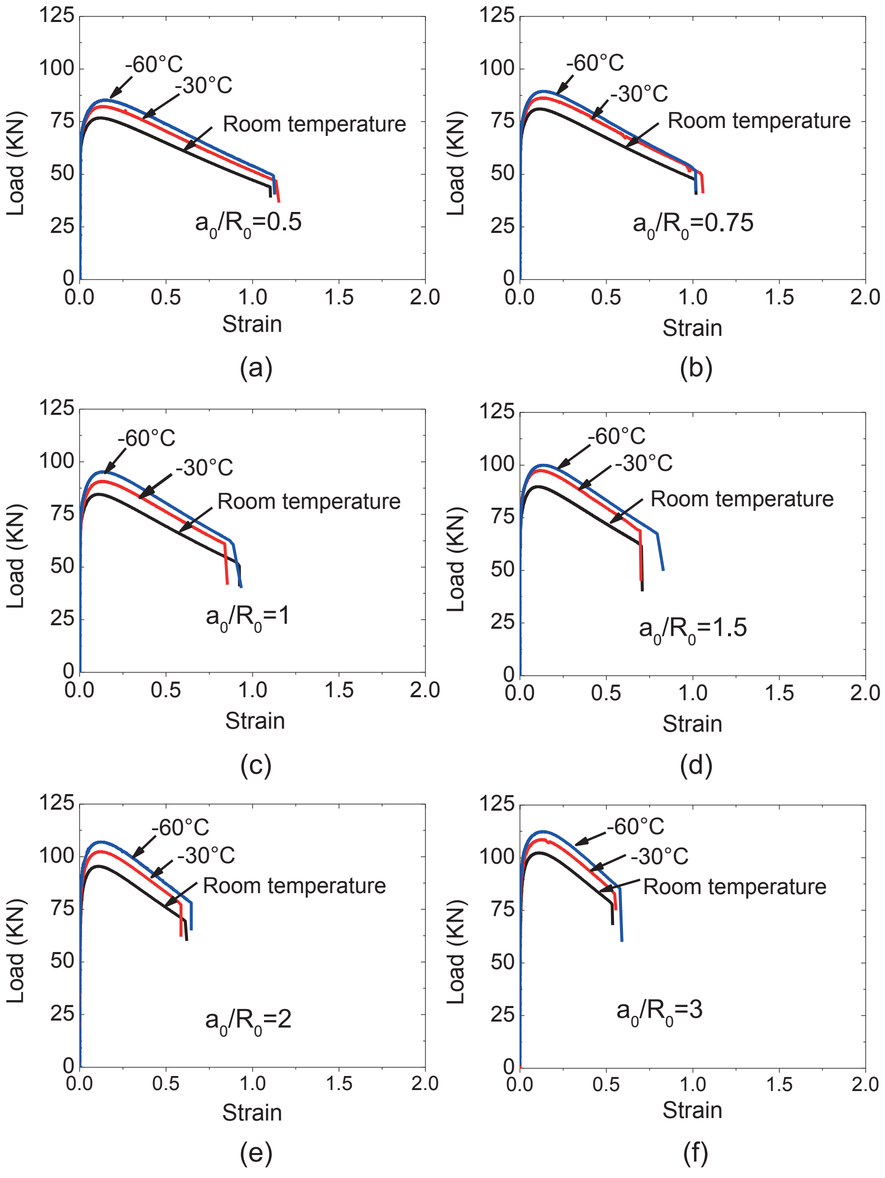

(a) (b)

(c) (d)

(e) (f)

Fig. 10 Load-strain curves for axisymmetric notched tensile specimens with same geometry tested at different temperatures. (a) $a_0/R_0 = 0.5$*; (b)* $a_0/R_0 = 0.75$*;(c)* $a_0/R_0 = 1$*;(d)* $a_0/R_0 = 1.5$*;(e)* $a_0/R_0 = 2$*;(f)* $a_0/R_0 = 3$.

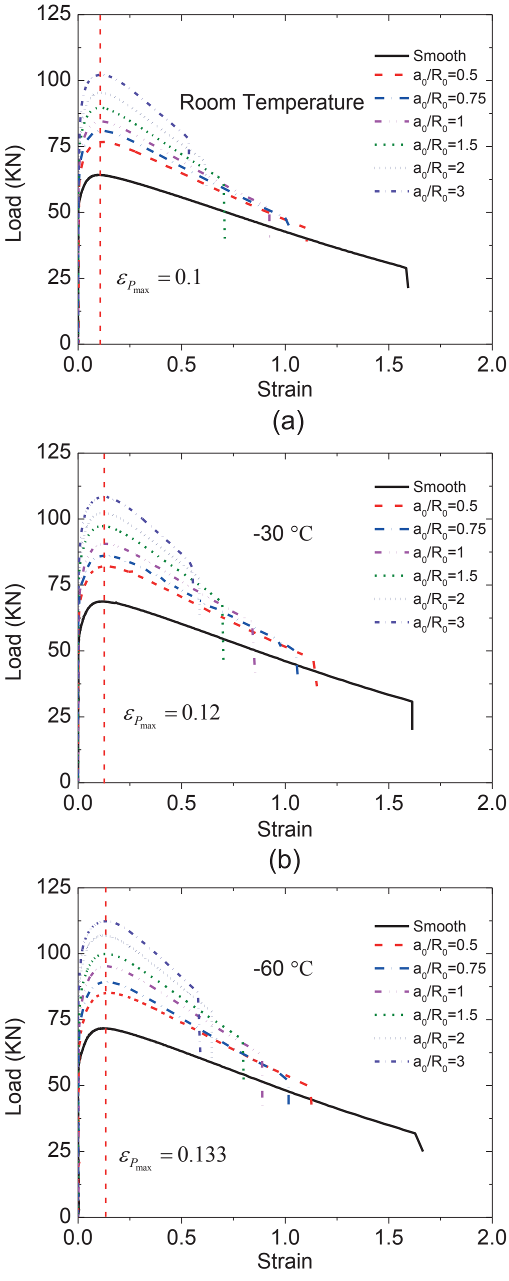

(a)

(b)

(c)

Fig. 11 Load-strain curve for specimens tested at same temperature.

(a) Room temperature; (b) -30℃; (c) -60℃.

Representative load-strain curves for axisymmetric notched specimens with same geometry at different test temperatures are presented in Fig. 10. As expected, the load for specimen tested at lower temperature is larger than that at higher temperature at the same strain level. The maximum load also increases with the decrease of test temperature. The influence of lowering temperature on the fracture strain for each notch geometry shown in Fig. 10 is not very obvious.

Load-strain curves in Fig. 9 and Fig. 10 are regrouped by test temperature and are presented in Fig. 11. It is clearly seen that specimen with sharper notch (larger a_0/R_0) corresponds to higher load at the same strain. The maximum load increases with the increase of a_0/R_0 at each test temperature. Instability analysis of axisymmetric notched tensile specimen showed that the strain corresponding to the maximum load, $\varepsilon_{P_{\max}}$, is a material parameter which is approximately equal to the value of $\varepsilon_{P_{\max}}$ for the smooth round bar specimen and independent of the notch geometry [42]. This is true for the axisymmetric notched specimen tested at the same temperature, as red dash curve points out in Fig. 11. For materials following power law hardening rule, the value of $\varepsilon_{P_{\max}}$ equals to the strain hardening exponent. It should be noted that $\varepsilon_{P_{\max}}$ is sensitive to temperature. For the structural steel studied, $\varepsilon_{P_{\max}}$ increases slightly as temperature decreases.

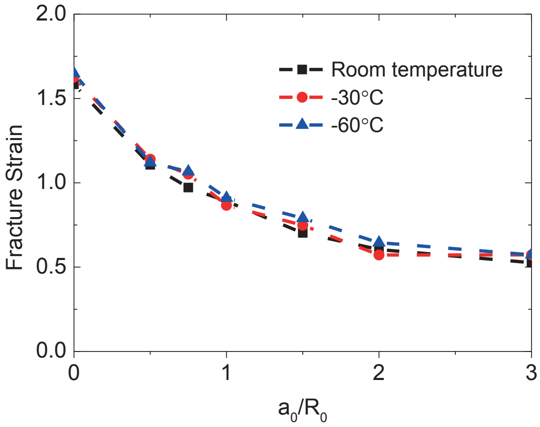

Fig. 12 Fracture strain versus initial notch radius ratio.

The average value of fracture strains from parallel tests in Fig. 11 are presented in Fig. 12 as a function of initial notch radius ratio. It is very interesting to observe that the average fracture strains do not deteriorate with the decrease of temperature to -60℃. For the notched specimens, the fracture strains at low temperatures are somewhat slightly higher than those at room temperature. Michael and Richard [40] performed quasi-static tensile test with Al-Cu-Mg-Ag alloy from 25℃ to 150℃. They found that the temperature effect on fracture strain for axisymmetric notched specimens can be neglected. Spit Hopkinson tension bar tests at 100 to 500°C reported by Børvik and Hopperstad [18, 36] showed that the influence of test temperature on fracture locus of Weldox 460 E steel was insignificant. Our study in this paper shows that load carrying capacity of smooth and notched specimens of this 420MPa structural steel increase with low temperature, however, the fracture strains (ductility) for smooth and notched specimens don't tend to deteriorate with decreasing test temperature (down to -60℃).

4. Numerical analysis

In order to construct the fracture locus, we need to perform numerical analysis to capture the stress triaxiality evolution. During the loading, the specimen deformed and the stress triaxiality at the center of the specimen minimum cross-section varied accordingly. For non-proportional loading, a strain-weighted average stress triaxiality T^* is widely used [19, 33, 34, 43]:

$$T^* = \frac{1}{\varepsilon_f}\int_0^{\varepsilon_f} T(\varepsilon)\,\mathrm{d}\varepsilon \tag{5}$$

In order to capture the evolution of stress triaxiality in the center of minimum cross-section of the necked/notched specimen, we performed numerical analyses with Abaqus/Standard 6.14[44]. The specimen configurations used for numerical analyses are the same as used in experiments. Axisymmetric model is used with very small mesh size (approximately 0.4*0.4 mm) in the notch region. The 4-noded axisymmetric element with reduced integration (CAX4R) is used. Large deformation is accounted. Symmetric boundary condition is applied in the symmetric plane of smooth specimen and axisymmetric notched specimens. A typical mesh of axisymmetric notched specimen with $a_0/R_0 = 3$ is presented in Fig. 13. For all the numerical analyses, the specimen is loaded in displacement control manner.

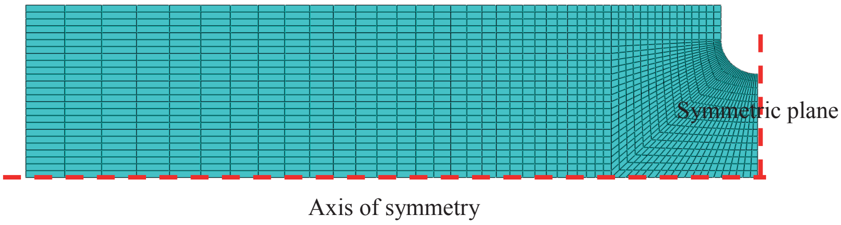

Fig. 13 Typical mesh for axisymmetric notched tensile specimen with $a_0/R_0 = 3$.

The true stress-strain curves in Fig. 9 (b) cannot be used directly for numerical analyses, due to the tri-axial stress state in the specimen necked region after diffuse necking [21, 37, 39, 45]. Bridgman [21] proposed an analytical correction method based on axisymmetric analysis of a necked round bar specimen, Eq. (6). However, the Bridgman correction is difficult to practice, since the current notch curvature radius should be measured. Le Roy have presented an empirical relation with a/R and ε [46], see Eq. (7). Combined with Eq. (6) and Eq. (7), true stress-strain curves from smooth round bar specimen can be corrected. Fig. 14 shows the equivalent stress-strain curves by correcting the curves in Fig. 9 (b), together with the corresponding true stress-strain curves. Obvious difference can be seen between the true stress-strain curves and equivalent stress-strain curves at large strain. Recently, we proposed a new correction function, with which true stress-strain curve from an axisymmetric notched tensile specimen can be converted to material's equivalent stress-strain curve accurately [47, 48]. The equivalent stress-strain curves derived with notch specimens present to be identical to the Bridgman method for this 420 MPa structure steel. The equivalent stress-strain curves in Fig. 14 are then used in the numerical analyses, together with Poisson ratio $\nu = 0.3$ and Young's modulus $E = 200GPa$.

$$\xi = (1+\frac{2R}{a})\cdot\ln(1+\frac{a}{2R}) \tag{6}$$

$$\frac{a}{R} = 1.1\cdot(\varepsilon - \varepsilon_{P\max}) \tag{7}$$

$$\sigma_{eq} = \frac{\sigma_t}{\xi} \tag{8}$$

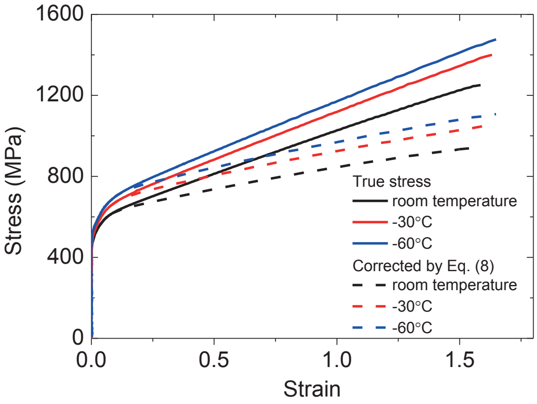

Fig. 14 Equivalent stress-strain curves obtained by correcting true stress-strain curves from smooth specimen at each test temperature with the Bridgman method, Eq. (8).

Load-strain curves from numerical analyses are compared with those from experiments for specimen with same geometry and test temperature. Fig. 15 presents the load-strain curves from experiment and from numerical simulation for axisymmetric notched specimen with $a_0/R_0 = 2$ tested at -60°C. Very good agreement can be observed, which confirms that the correction function Eq. (8) is accurate. It also indicates that the deformation in the notch region can be well captured during the loading process.

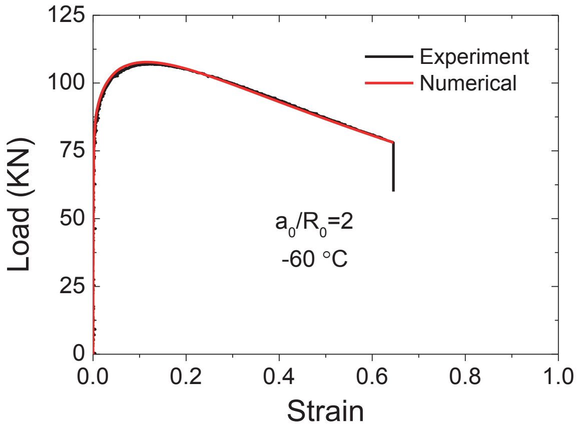

Fig. 15 Comparison of load-strain curves from experiment and from numerical analysis for notched tensile specimen with $a_0/R_0 = 2$ *tested at* -60°C.

From numerical analysis, the stress triaxiality at each material point can be calculated. Fig. 16 presents the stress triaxiality evolution at the center of the minimum cross-section, up to fracture strain. As it can be seen in Fig. 16, for the smooth specimen, the stress triaxiality is constant and equals to 1/3 at the beginning, and then increases with the increase of strain. For axisymmetric notched specimens with $a_0/R_0 \leq 1$, stress triaxiality increases with the increase of strain, while for specimens with $a_0/R_0 > 1$, stress triaxiality increases firstly and then decrease with the increase of strain. This infers that the specimen initial notch geometry strongly affects the stress triaxiality evolution. For the smooth specimen, the value of stress triaxiality at fracture presents to be even larger than the notched specimen with $a_0/R_0 = 0.5$ in Fig. 16, reflecting the severe deformation in the necking region at failure for smooth specimen.

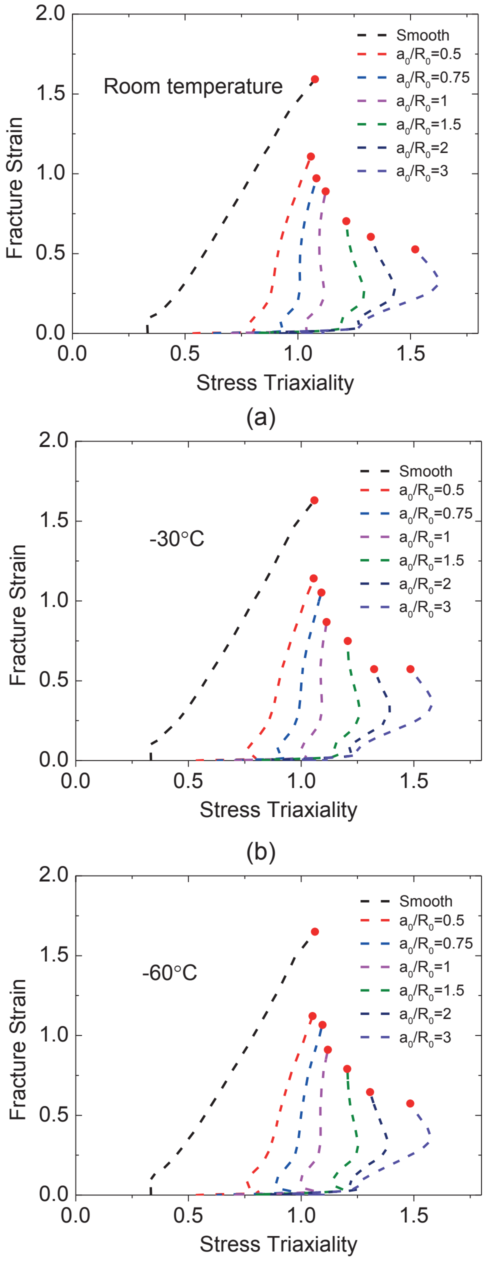

(a)

(b)

(c)

Fig. 16 Stress triaxiality evolution at the specimen minimum cross-section center up to fracture strain. (a) Room temperature; (b) -30℃; (c) -60℃.

For each specimen in Fig. 16, the average stress triaxiality is calculated by Eq. (5). Fracture strain is plotted against the corresponding average stress triaxiality in Fig. 17 for specimens tested at the same temperature. It can be clearly observed that the fracture strain decreases with the increase of average stress triaxiality. Similar to Fig. 12, the three curves in Fig. 17 almost collapse into one, except small scatter. Interestingly, the local behavior shown in Fig. 17 closely reflect the global behavior in Fig. 12.

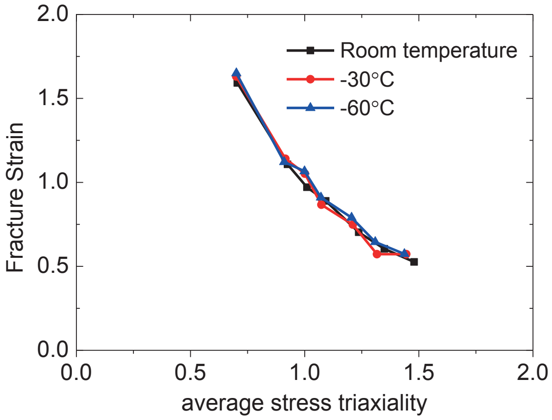

Fig. 17 Fracture strain versus average stress triaxiality at different temperatures.

Indeed, we can formulate the fracture locus with different measures of stress triaxiality: the initial stress triaxiality (calculated by Eq. (1)), the strain-weighted average stress triaxiality and the stress triaxiality at failure. Fig. 18 presents these three measures of fracture loci for specimens tested at room temperature. These three curves behave differently, but show similar trend that the fracture strain decreases with the increase of stress triaxiality. It can be observed that for the smooth specimens, the values of stress triaxiality by different measures differ significantly; while for the notched specimen, the difference tend to decrease with increasing a_0/R_0, especially for the red and green curves. It is difficult to conclude which curve in Fig. 18 is better, since each of them presents pros and cons in certain aspects. For the fracture locus determined with the initial stress triaxiality, it can be conveniently formulated once the fracture strain is known. However, the stress triaxiality evolution or the damage evolution is not considered. The curve constructed on the space of average stress triaxiality and fracture strain takes the strain history into account and depicts the damage accumulation in the form: $D = \int_0^{\varepsilon_f} T(\varepsilon)\, d\varepsilon = T^* \cdot \varepsilon_f$. D is a material failure indicator. However, we need to run numerical analyses in parallel to capture the deformation history and stress triaxiality evolution. The stress triaxiality at failure is more straightforward to represent the instantaneous stress state at the fracture point. Similar to the strain-weighted average stress triaxiality, numerical analysis is also necessary. Only for proportional loading, fracture loci constructed by initial stress triaxiality, strain-weighted average stress triaxiality and stress triaxiality at failure collapse into one. It should be noted that when it comes to complex or non-proportional loading, the initial and finial value of stress triaxiality are more or less meaningless and the strain-weighted average stress triaxiality tends to be more representative.

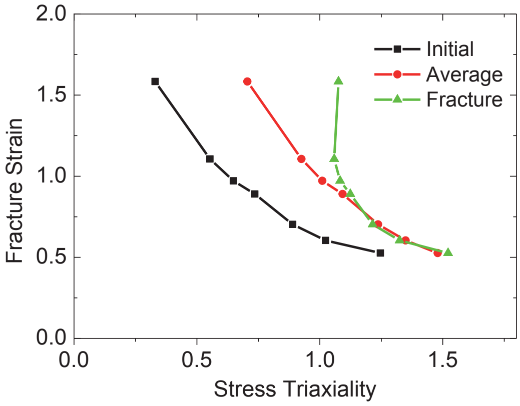

Fig. 18 Fracture strain versus different measures of stress triaxiality for the tests performed at room temperature.

5. Concluding remarks

In this study, smooth round bar specimens and axisymmetric notched tensile specimens have been used to investigate low temperature (down to -60℃) effect on a 420 MPa structural steel fracture locus. A two-plane mirror system and a digital high-speed camera were used together to monitor specimen deformation in the tests. Combined with numerical analyses, the specimen deformation was simulated to capture the stress triaxiality evolution up to failure. Tensile tests with smooth and notched specimen show that decreasing temperature increases material's strength and strain at maximum load, while the fracture strain (ductility) doesn't deteriorate for the testing temperature down to -60℃. The fracture locus formulated with the initial, strain-weighted or the finial value (the value at failure) of stress triaxiality and the fracture strain shows the significant dependence of ductile failure on the stress state. The mechanical response at low temperature in this study indicate that this 420 MPa structural steel is very promising for the application in the Arctic region.

Acknowledgement

The Chinese Scholarship Council is greatly acknowledged for the financial support. The authors wish to thank the Research Council of Norway for funding through the Petromaks 2 Programme, Contract No.228513/E30.

Reference

1. Gautier DL, Bird KJ, Charpentier RR, Grantz A (2009) Assessment of undiscovered oil and gas in the Arctic. *Science*. **324**: 1175-1179.
2. Ren X, Nordhagen HO, Zhang Z (2015) Tensile properties of 420MPa steel at low temperature. *Twenty-fifth Internation Ocean and Polar Engineering Conference*, Hawaii.
3. Tsykahara H, Iung T (1998) Finite element simulation of the Piobert–Lüders behavior in an uniaxial tensile test. *Materials Science and Engineering: A*. **248**: 304-308.
4. Zhang J (2005) Lüders bands propagation of 1045 steel under multiaxial stress state. *International Journal of Plasticity*. **21**: 651-670.
5. Dahl BA (2016) Effect of low temperature tensile priperties on crack driving force for arctic application. *submitted*.
6. Avila JA, Lucon E, Sowards J, Mei PR, Ramirez AJ (2016) Assessment of Ductile-to-Brittle Transition Behavior of Localized Microstructural Regions in a Friction-Stir Welded X80 Pipeline Steel with Miniaturized Charpy V-Notch Testing. *Metallurgical and Materials Transactions A*. **47**: 2855-2865.
7. Capelle J, Furtado J, Azari Z, Jallais S, Pluvinage G (2013) Design based on ductile–brittle transition temperature for API 5L X65 steel used for dense CO2 transport. *Engineering Fracture Mechanics*. **110**: 270-280.
8. Chao YJ, Ward JD, Sands RG (2007) Charpy impact energy, fracture toughness and ductile–brittle transition temperature of dual-phase 590 Steel. *Materials & Design*. **28**: 551-557.
9. Chatterjee A, Chakrabarti D, Moitra A, Mitra R, Bhaduri AK (2015) Effect of deformation temperature on the ductile–brittle transition behavior of a modified 9Cr–1Mo steel. *Materials Science and Engineering: A*. **630**: 58-70.
10. Gopalan A, Samal MK, Chakravartty JK (2015) Fracture toughness evaluation of 20MnMoNi55 pressure vessel steel in the ductile to brittle transition regime: Experiment & numerical simulations. *Journal of Nuclear Materials*. **465**: 424-432.
11. Tanguy B, Besson J, Piques R, Pineau A (2005) Ductile to brittle transition of an A508 steel characterized by Charpy impact test. *Engineering Fracture Mechanics*. **72**: 49-72.
12. Zhang Y, Yu C, Zhou T, et al. (2015) Effects of Ti and a twice-quenching treatment on the microstructure and ductile brittle transition temperature of 9CrWVTiN steels. *Materials & Design*. **88**: 675-682.
13. Bao Y, Wierzbicki T (2004) On fracture locus in the equivalent strain and stress triaxiality space. *International Journal of Mechanical Sciences*. **46**: 81-98.
14. Malcher L, Andrade Pires FM, César de Sá JMA (2014) An extended GTN model for ductile fracture under high and low stress triaxiality. *International Journal of Plasticity*. **54**: 193-228.
15. Mirone G (2007) Role of stress triaxiality in elastoplastic characterization and ductile failure prediction. *Engineering Fracture Mechanics*. **74**: 1203-1221.
16. Mirone G, Corallo D (2010) A local viewpoint for evaluating the influence of stress triaxiality and Lode angle on ductile failure and hardening. *International Journal of Plasticity*. **26**: 348-371.
17. Mohr D, Henn S (2007) Calibration of Stress-triaxiality Dependent Crack Formation Criteria: A New Hybrid Experimental–Numerical Method. *Experimental Mechanics*. **47**: 805-820.
18. Børvik T, Hopperstad OS, Dey S, Pizzinato EV, Langseth M, Albertini C (2005) Strength and ductility of Weldox 460 E steel at high strain rates, elevated temperatures and various stress triaxialities. *Engineering Fracture Mechanics*. **72**: 1071-1087.
19. Yu H, Olsen JS, He J, Zhang Z (2016) Effects of loading path on the fracture loci in a 3D space. *Engineering Fracture Mechanics*. **151**: 22-36.

20. Benzerga AA, Surovik D, Keralavarma SM (2012) On the path-dependence of the fracture locus in ductile materials – Analysis. *International Journal of Plasticity*. **37**: 157-170.

21. Bridgman PW (1952) *Studies in large plastic flow and fracture*. MaGraw-Hill, New York.

22. Johnson GR, Cook WH (1985) Fracture characteristics of three metals subjected to various strains, strain rates, temperatures and pressures. *Engineering Fracture Mechanics*. **21**: 31-48.

23. Peng J, Wu PD, Huang Y, Chen X (2009) Effects of superimposed hydrostatic pressure on fracture in round bars under tension. *International Journal of Solids and Structures*. **46**: 3741-3749.

24. Wu PD, Embury JD, Lloyd DJ, Huang Y, Neale KW (2009) Effects of superimposed hydrostatic pressure on sheet metal formability. *International Journal of Plasticity*. **25**: 1711-1725.

25. Alves Ml, Jones N (1999) Influence of hydrostatic stress on failure of axisymmetric notched specimens. *Journal of the Mechanics and Physics of Solids*. **47**: 643-667.

26. Han KJ, Shuai J, Deng X, Kong L, Zhao X, Sutton M (2014) The effect of constraint on CTOD fracture toughness of API X65 steel. *Engineering Fracture Mechanics*. **124-125**: 167-181.

27. Xu J, Zhang ZL, Østby E, Nyhus B, Sun DB (2010) Constraint effect on the ductile crack growth resistance of circumferentially cracked pipes. *Engineering Fracture Mechanics*. **77**: 671-684.

28. Z.L.Zhang, Niemi E (1994) Studies on the ductility predictions by different local failure criteria. *Engineering Fracture Mechanics*. **48**: 529-540.

29. Dunand M, Mohr D (2011) On the predictive capabilities of the shear modified Gurson and the modified Mohr–Coulomb fracture models over a wide range of stress triaxialities and Lode angles. *Journal of the Mechanics and Physics of Solids*. **59**: 1374-1394.

30. Dunand M, Mohr D (2014) Effect of Lode parameter on plastic flow localization after proportional loading at low stress triaxialities. *Journal of the Mechanics and Physics of Solids*. **66**: 133-153.

31. Bryhni Dæhli LE, Børvik T, Hopperstad OS (2016) Influence of loading path on ductile fracture of tensile specimens made from aluminium alloys. *International Journal of Solids and Structures*. **88-89**: 17-34.

32. Mohr D, Marcadet SJ (2015) Micromechanically-motivated phenomenological Hosford–Coulomb model for predicting ductile fracture initiation at low stress triaxialities. *International Journal of Solids and Structures*. **67-68**: 40-55.

33. Bai Y, Teng X, Wierzbicki T (2009) On the Application of Stress triaxiality formula for plane strain fracture testing. *Journal of Engineering Material and Technology*. **131**.

34. Basu S, Benzerga AA (2015) On the path-dependence of the fracture locus in ductile materials: Experiments. *International Journal of Solids and Structures*. **71**: 79-90.

35. Børvik T, Hopperstad OS, Berstad T (2003) On the influence of stress triaxiality and strain rate on the behaviour of a structural steel. Part II. Numerical study. *European Journal of Mechanics - A/Solids*. **22**: 15-32.

36. Hopperstad OS, Børvik T, Langseth M, Labibes K, Albertini C (2003) On the influence of stress triaxiality and strain rate on the behaviour of a structural steel. Part I. Experiments. *European Journal of Mechanics - A/Solids*. **22**: 1-13.

37. Bao Y, Wierzbicki T (2005) On the cut-off value of negative triaxiality for fracture. *Engineering Fracture Mechanics*. **72**: 1049-1069.

38. Bruck HA, McNeill SR, Sutton MA, Peters WH (1989) Digital image correlation using Newton-Raphson method of partial differential correction. *Experimental Mechanics*. **29**: 261-267.

39. Tu S, Ren X, Nyhus B, Akselsen OM, He J, Zhang Z (2017) A special notched tensile specimen to determine the flow stress-strain curve of hardening materials without applying the Bridgman correction. *Engineering Fracture Mechanics*. **179**: 225-239.

40. Michael JH, Richard PG (1997) Elevated temperature fractrue toughness of Al-Cu-Mg-Ag sheet Characterization and modeling. *Metallurgical and Materials Transactions A*. **28A**: 1815-1829.

41. Børvik T, Hopperstad OS, Berstad T, Langseth M (2001) A computational model of viscoplasticity and ductile damage for impact and penetration. *European Journal of Mechanics - A/Solids*. **20**: 685-712.

42. Zhang ZL, Hauge M, Thaulow C, Ødegård J (2002) A notched cross weld tensile testing method for determining true stress–strain curves for weldments. *Engineering Fracture Mechanics*. **69**: 353-366.

43. Bao Y, Wierzbicki T (2004) A Comparative Study on Various Ductile Crack Formation Criteria. *Journal of Engineering Materials and technology*. **126**: 314-324.

44. Abaqus (2014) *Abaqus User Manual (Version 6.14)*.

45. Mirone G (2004) A new model for the elastoplastic characterization and the stress–strain determination on the necking section of a tensile specimen. *International Journal of Solids and Structures*. **41**: 3545-3564.

46. Roy GL, Embury JD, Edward G, Ashby MF (1981) A model of ductile fracture based on the nucleation and growth of voids. *Acta Metallurgica*. **29**: 1509-1522.

47. Tu S, Ren X, He J, Zhang Z (2018) A method for determining material's equivalent stress-strain curve with any axisymmetric notched tensile specimens without Bridgman correction. *International Journal of Mechanical Sciences*. **135**: 656-667.

48. Tu S, Ren X, He J, Zhang Z Experimental measurement of equivalent stress-strain curve of a 420 MPa structure steel with axisymmetric notched tensile specimen. *In preparation*.

A.5

Numerical study on the effect of Lüders plateau on the ductile crack growth resistance of SENT specimens

Authors: Shengwen Tu; Xiaobo Ren; Jianying He; Zhiliang Zhang

Submitted to International Journal of Fracture

Paper V

Publication List-Department of Structural Engineering

Appendix B

DEPARTMENT OF STRUCTURAL ENGINEERING
NORWEGIAN UNIVERSITY OF SCIENCE AND TECHNOLOGY

N–7491 TRONDHEIM, NORWAY
Telephone: +47 73 59 47 00 Telefax: +47 73 59 47 01

"Reliability Analysis of Structural Systems using Nonlinear Finite Element Methods",
C. A. Holm, 1990:23, ISBN 82-7119-178-0.

"Uniform Stratified Flow Interaction with a Submerged Horizontal Cylinder",
Ø. Arntsen, 1990:32, ISBN 82-7119-188-8.

"Large Displacement Analysis of Flexible and Rigid Systems Considering Displacement-Dependent Loads and Nonlinear Constraints",
K. M. Mathisen, 1990:33, ISBN 82-7119-189-6.

"Solid Mechanics and Material Models including Large Deformations",
E. Levold, 1990:56, ISBN 82-7119-214-0, ISSN 0802-3271.

"Inelastic Deformation Capacity of Flexurally-Loaded Aluminium Alloy Structures",
T. Welo, 1990:62, ISBN 82-7119-220-5, ISSN 0802-3271.

"Visualization of Results from Mechanical Engineering Analysis",
K. Aamnes, 1990:63, ISBN 82-7119-221-3, ISSN 0802-3271.

"Object-Oriented Product Modeling for Structural Design",
S. I. Dale, 1991:6, ISBN 82-7119-258-2, ISSN 0802-3271.

"Parallel Techniques for Solving Finite Element Problems on Transputer Networks",
T. H. Hansen, 1991:19, ISBN 82-7119-273-6, ISSN 0802-3271.

"Statistical Description and Estimation of Ocean Drift Ice Environments",
R. Korsnes, 1991:24, ISBN 82-7119-278-7, ISSN 0802-3271.

“Properties of concrete related to fatigue damage: with emphasis on high strength concrete”,
G. Petkovic, 1991:35, ISBN 82-7119-290-6, ISSN 0802-3271.

"Turbidity Current Modelling",
B. Brørs, 1991:38, ISBN 82-7119-293-0, ISSN 0802-3271.

"Zero-Slump Concrete: Rheology, Degree of Compaction and Strength. Effects of Fillers as Part Cement-Replacement",
C. Sørensen, 1992:8, ISBN 82-7119-357-0, ISSN 0802-3271.

"Nonlinear Analysis of Reinforced Concrete Structures Exposed to Transient Loading",
K. V. Høiseth, 1992:15, ISBN 82-7119-364-3, ISSN 0802-3271.

"Finite Element Formulations and Solution Algorithms for Buckling and Collapse Analysis of Thin Shells",
R. O. Bjærum, 1992:30, ISBN 82-7119-380-5, ISSN 0802-3271.

"Response Statistics of Nonlinear Dynamic Systems",
J. M. Johnsen, 1992:42, ISBN 82-7119-393-7, ISSN 0802-3271.

"Digital Models in Engineering. A Study on why and how engineers build and operate digital models for decisison support",
J. Høyte, 1992:75, ISBN 82-7119-429-1, ISSN 0802-3271.

"Sparse Solution of Finite Element Equations",
A. C. Damhaug, 1992:76, ISBN 82-7119-430-5, ISSN 0802-3271.

"Some Aspects of Floating Ice Related to Sea Surface Operations in the Barents Sea",
S. Løset, 1992:95, ISBN 82-7119-452-6, ISSN 0802-3271.

"Modelling of Cyclic Plasticity with Application to Steel and Aluminium Structures",
O. S. Hopperstad, 1993:7, ISBN 82-7119-461-5, ISSN 0802-3271.

"The Free Formulation: Linear Theory and Extensions with Applications to Tetrahedral Elements
with Rotational Freedoms",
G. Skeie, 1993:17, ISBN 82-7119-472-0, ISSN 0802-3271.

"Høyfast betongs motstand mot piggdekkslitasje. Analyse av resultater fra prøving i Veisliter'n",
T. Tveter, 1993:62, ISBN 82-7119-522-0, ISSN 0802-3271.

"A Nonlinear Finite Element Based on Free Formulation Theory for Analysis of Sandwich Structures",
O. Aamlid, 1993:72, ISBN 82-7119-534-4, ISSN 0802-3271.

"The Effect of Curing Temperature and Silica Fume on Chloride Migration and Pore Structure of High Strength Concrete",
C. J. Hauck, 1993:90, ISBN 82-7119-553-0, ISSN 0802-3271.

"Failure of Concrete under Compressive Strain Gradients",
G. Markeset, 1993:110, ISBN 82-7119-575-1, ISSN 0802-3271.

"An experimental study of internal tidal amphidromes in Vestfjorden",
J. H. Nilsen, 1994:39, ISBN 82-7119-640-5, ISSN 0802-3271.

"Structural analysis of oil wells with emphasis on conductor design",
H. Larsen, 1994:46, ISBN 82-7119-648-0, ISSN 0802-3271.

"Adaptive methods for non-linear finite element analysis of shell structures",
K. M. Okstad, 1994:66, ISBN 82-7119-670-7, ISSN 0802-3271.

"On constitutive modelling in nonlinear analysis of concrete structures",
O. Fyrileiv, 1994:115, ISBN 82-7119-725-8, ISSN 0802-3271.

"Fluctuating wind load and response of a line-like engineering structure with emphasis on motion-induced wind forces",
J. Bogunovic Jakobsen, 1995:62, ISBN 82-7119-809-2, ISSN 0802-3271.

"An experimental study of beam-columns subjected to combined torsion, bending and axial actions",
A. Aalberg, 1995:66, ISBN 82-7119-813-0, ISSN 0802-3271.

"Scaling and cracking in unsealed freeze/thaw testing of Portland cement and silica fume concretes",
S. Jacobsen, 1995:101, ISBN 82-7119-851-3, ISSN 0802-3271.

"Damping of water waves by submerged vegetation. A case study of laminaria hyperborea",
A. M. Dubi, 1995:108, ISBN 82-7119-859-9, ISSN 0802-3271.

"The dynamics of a slope current in the Barents Sea",
Sheng Li, 1995:109, ISBN 82-7119-860-2, ISSN 0802-3271.

"Modellering av delmaterialenes betydning for betongens konsistens",
Ernst Mørtsell, 1996:12, ISBN 82-7119-894-7, ISSN 0802-3271.

"Bending of thin-walled aluminium extrusions",
Birgit Søvik Opheim, 1996:60, ISBN 82-7119-947-1, ISSN 0802-3271.

"Material modelling of aluminium for crashworthiness analysis",
Torodd Berstad, 1996:89, ISBN 82-7119-980-3, ISSN 0802-3271.

"Estimation of structural parameters from response measurements on submerged floating tunnels",
Rolf Magne Larssen, 1996:119, ISBN 82-471-0014-2, ISSN 0802-3271.

“Numerical modelling of plain and reinforced concrete by damage mechanics”,
Mario A. Polanco-Loria, 1997:20, ISBN 82-471-0049-5, ISSN 0802-3271.

“Nonlinear random vibrations - numerical analysis by path integration methods”,
Vibeke Moe, 1997:26, ISBN 82-471-0056-8, ISSN 0802-3271.

“Numerical prediction of vortex-induced vibration by the finite element method”,
Joar Martin Dalheim, 1997:63, ISBN 82-471-0096-7, ISSN 0802-3271.

“Time domain calculations of buffeting response for wind sensitive structures”,
Ketil Aas-Jakobsen, 1997:148, ISBN 82-471-0189-0, ISSN 0802-3271.

"A numerical study of flow about fixed and flexibly mounted circular cylinders",
Trond Stokka Meling, 1998:48, ISBN 82-471-0244-7, ISSN 0802-3271.

“Estimation of chloride penetration into concrete bridges in coastal areas”,
Per Egil Steen, 1998:89, ISBN 82-471-0290-0, ISSN 0802-3271.

“Stress-resultant material models for reinforced concrete plates and shells”,
Jan Arve Øverli, 1998:95, ISBN 82-471-0297-8, ISSN 0802-3271.

“Chloride binding in concrete. Effect of surrounding environment and concrete composition”,
Claus Kenneth Larsen, 1998:101, ISBN 82-471-0337-0, ISSN 0802-3271.

“Rotational capacity of aluminium alloy beams”,
Lars A. Moen, 1999:1, ISBN 82-471-0365-6, ISSN 0802-3271.

“Stretch Bending of Aluminium Extrusions”,
Arild H. Clausen, 1999:29, ISBN 82-471-0396-6, ISSN 0802-3271.

“Aluminium and Steel Beams under Concentrated Loading”,
Tore Tryland, 1999:30, ISBN 82-471-0397-4, ISSN 0802-3271.

"Engineering Models of Elastoplasticity and Fracture for Aluminium Alloys",
Odd-Geir Lademo, 1999:39, ISBN 82-471-0406-7, ISSN 0802-3271.

"Kapasitet og duktilitet av dybelforbindelser i trekonstruksjoner",
Jan Siem, 1999:46, ISBN 82-471-0414-8, ISSN 0802-3271.

“Etablering av distribuert ingeniørarbeid; Teknologiske og organisatoriske erfaringer fra en norsk ingeniørbedrift”,
Lars Line, 1999:52, ISBN 82-471-0420-2, ISSN 0802-3271.

“Estimation of Earthquake-Induced Response”,
Símon Ólafsson, 1999:73, ISBN 82-471-0443-1, ISSN 0802-3271.

“Coastal Concrete Bridges: Moisture State, Chloride Permeability and Aging Effects”
Ragnhild Holen Relling, 1999:74, ISBN 82-471-0445-8, ISSN 0802-3271.

”Capacity Assessment of Titanium Pipes Subjected to Bending and External Pressure”,
Arve Bjørset, 1999:100, ISBN 82-471-0473-3, ISSN 0802-3271.

“Validation of Numerical Collapse Behaviour of Thin-Walled Corrugated Panels”,
Håvar Ilstad, 1999:101, ISBN 82-471-0474-1, ISSN 0802-3271.

“Strength and Ductility of Welded Structures in Aluminium Alloys”,
Miroslaw Matusiak, 1999:113, ISBN 82-471-0487-3, ISSN 0802-3271.

“Thermal Dilation and Autogenous Deformation as Driving Forces to Self-Induced Stresses in High Performance Concrete”,
Øyvind Bjøntegaard, 1999:121, ISBN 82-7984-002-8, ISSN 0802-3271.

“Some Aspects of Ski Base Sliding Friction and Ski Base Structure”,
Dag Anders Moldestad, 1999:137, ISBN 82-7984-019-2, ISSN 0802-3271.

"Electrode reactions and corrosion resistance for steel in mortar and concrete",
Roy Antonsen, 2000:10, ISBN 82-7984-030-3, ISSN 0802-3271.

"Hydro-Physical Conditions in Kelp Forests and the Effect on Wave Damping and Dune Erosion. A case study on Laminaria Hyperborea",
Stig Magnar Løvås, 2000:28, ISBN 82-7984-050-8, ISSN 0802-3271.

"Random Vibration and the Path Integral Method",
Christian Skaug, 2000:39, ISBN 82-7984-061-3, ISSN 0802-3271.

"Buckling and geometrical nonlinear beam-type analyses of timber structures",
Trond Even Eggen, 2000:56, ISBN 82-7984-081-8, ISSN 0802-3271.

”Structural Crashworthiness of Aluminium Foam-Based Components”,
Arve Grønsund Hanssen, 2000:76, ISBN 82-7984-102-4, ISSN 0809-103X.

“Measurements and simulations of the consolidation in first-year sea ice ridges, and some aspects of mechanical behaviour”,
Knut V. Høyland, 2000:94, ISBN 82-7984-121-0, ISSN 0809-103X.

”Kinematics in Regular and Irregular Waves based on a Lagrangian Formulation”,
Svein Helge Gjøsund, 2000-86, ISBN 82-7984-112-1, ISSN 0809-103X.

”Self-Induced Cracking Problems in Hardening Concrete Structures”,
Daniela Bosnjak, 2000-121, ISBN 82-7984-151-2, ISSN 0809-103X.

"Ballistic Penetration and Perforation of Steel Plates",
Tore Børvik, 2000:124, ISBN 82-7984-154-7, ISSN 0809-103X.

"Freeze-Thaw resistance of Concrete. Effect of: Curing Conditions, Moisture Exchange and Materials",
Terje Finnerup Rønning, 2001:14, ISBN 82-7984-165-2, ISSN 0809-103X

"Structural behaviour of post tensioned concrete structures. Flat slab. Slabs on ground",
Steinar Trygstad, 2001:52, ISBN 82-471-5314-9, ISSN 0809-103X.

"Slipforming of Vertical Concrete Structures. Friction between concrete and slipform panel",
Kjell Tore Fosså, 2001:61, ISBN 82-471-5325-4, ISSN 0809-103X.

"Some numerical methods for the simulation of laminar and turbulent incompressible flows",
Jens Holmen, 2002:6, ISBN 82-471-5396-3, ISSN 0809-103X.

“Improved Fatigue Performance of Threaded Drillstring Connections by Cold Rolling”,
Steinar Kristoffersen, 2002:11, ISBN: 82-421-5402-1, ISSN 0809-103X.

"Deformations in Concrete Cantilever Bridges: Observations and Theoretical Modelling",
Peter F. Takâcs, 2002:23, ISBN 82-471-5415-3, ISSN 0809-103X.

"Stiffened aluminium plates subjected to impact loading",
Hilde Giæver Hildrum, 2002:69, ISBN 82-471-5467-6, ISSN 0809-103X.

"Full- and model scale study of wind effects on a medium-rise building in a built up area",
Jónas Thór Snæbjørnsson, 2002:95, ISBN82-471-5495-1, ISSN 0809-103X.

“Evaluation of Concepts for Loading of Hydrocarbons in Ice-infested water”,
Arnor Jensen, 2002:114, ISBN 82-417-5506-0, ISSN 0809-103X.

”Numerical and Physical Modelling of Oil Spreading in Broken Ice”,
Janne K. Økland Gjøsteen, 2002:130, ISBN 82-471-5523-0, ISSN 0809-103X.

”Diagnosis and protection of corroding steel in concrete”,
Franz Pruckner, 20002:140, ISBN 82-471-5555-4, ISSN 0809-103X.

“Tensile and Compressive Creep of Young Concrete: Testing and Modelling”,
Dawood Atrushi, 2003:17, ISBN 82-471-5565-6, ISSN 0809-103X.

“Rheology of Particle Suspensions. Fresh Concrete, Mortar and Cement Paste with Various Types of Lignosulfonates”,
Jon Elvar Wallevik, 2003:18, ISBN 82-471-5566-4, ISSN 0809-103X.

“Oblique Loading of Aluminium Crash Components”,
Aase Reyes, 2003:15, ISBN 82-471-5562-1, ISSN 0809-103X.

“Utilization of Ethiopian Natural Pozzolans”,
Surafel Ketema Desta, 2003:26, ISSN 82-471-5574-5, ISSN:0809-103X.

"Behaviour and strength prediction of reinforced concrete structures with discontinuity regions", Helge Brå, 2004:11, ISBN 82-471-6222-9, ISSN 1503-8181.

"High-strength steel plates subjected to projectile impact. An experimental and numerical study", Sumita Dey, 2004:38, ISBN 82-471-6282-2 (printed version), ISBN 82-471-6281-4 (electronic version), ISSN 1503-8181.

"Alkali-reactive and inert fillers in concrete. Rheology of fresh mixtures and expansive reactions."
Bård M. Pedersen, 2004:92, ISBN 82-471-6401-9 (printed version), ISBN 82-471-6400-0 (electronic version), ISSN 1503-8181.

"On the Shear Capacity of Steel Girders with Large Web Openings".
Nils Christian Hagen, 2005:9 ISBN 82-471-6878-2 (printed version), ISBN 82-471-6877-4 (electronic version), ISSN 1503-8181.

"Behaviour of aluminium extrusions subjected to axial loading".
Østen Jensen, 2005:7, ISBN 82-471-6873-1 (printed version), ISBN 82-471-6872-3 (electronic version), ISSN 1503-8181.

"Thermal Aspects of corrosion of Steel in Concrete".
Jan-Magnus Østvik, 2005:5, ISBN 82-471-6869-3 (printed version), ISBN 82-471-6868 (electronic version), ISSN 1503-8181.

"Mechanical and adaptive behaviour of bone in relation to hip replacement." A study of bone remodelling and bone grafting.
Sébastien Muller, 2005:34, ISBN 82-471-6933-9 (printed version), ISBN 82-471-6932-0 (electronic version), ISSN 1503-8181.

"Analysis of geometrical nonlinearities with applications to timber structures".
Lars Wollebæk, 2005:74, ISBN 82-471-7050-5 (printed version), ISBN 82-471-7019-1 (electronic version), ISSN 1503-8181.

"Pedestrian induced lateral vibrations of slender footbridges",
Anders Rönnquist, 2005:102, ISBN 82-471-7082-5 (printed version), ISBN 82-471-7081-7 (electronic version), ISSN 1503-8181.

"Initial Strength Development of Fly Ash and Limestone Blended Cements at Various Temperatures Predicted by Ultrasonic Pulse Velocity",
Tom Ivar Fredvik, 2005:112, ISBN 82-471-7105-8 (printed version), ISBN 82-471-7103-1 (electronic version), ISSN 1503-8181.

"Behaviour and modelling of thin-walled cast components",
Cato Dørum, 2005:128, ISBN 82-471-7140-6 (printed version), ISBN 82-471-7139-2 (electronic version), ISSN 1503-8181.

“Behaviour and modelling of selfpiercing riveted connections”,
Raffaele Porcaro, 2005:165, ISBN 82-471-7219-4 (printed version), ISBN 82-471-7218-6 (electronic version), ISSN 1503-8181.

”Behaviour and Modelling og Aluminium Plates subjected to Compressive Load”,
Lars Rønning, 2005:154, ISBN 82-471-7169-1 (printed version), ISBN 82-471-7195-3 (electronic version), ISSN 1503-8181.

”Bumper beam-longitudinal system subjected to offset impact loading”,
Satyanarayana Kokkula, 2005:193, ISBN 82-471-7280-1 (printed version), ISBN 82-471-7279-8 (electronic version), ISSN 1503-8181.

“Control of Chloride Penetration into Concrete Structures at Early Age”,
Guofei Liu, 2006:46, ISBN 82-471-7838-9 (printed version), ISBN 82-471-7837-0 (electronic version), ISSN 1503-8181.

“Modelling of Welded Thin-Walled Aluminium Structures”,
Ting Wang, 2006:78, ISBN 82-471-7907-5 (printed version), ISBN 82-471-7906-7 (electronic version), ISSN 1503-8181.

”Time-variant reliability of dynamic systems by importance sampling and probabilistic analysis of ice loads”,
Anna Ivanova Olsen, 2006:139, ISBN 82-471-8041-3 (printed version), ISBN 82-471-8040-5 (electronic version), ISSN 1503-8181.

“Fatigue life prediction of an aluminium alloy automotive component using finite element analysis of surface topography”.
Sigmund Kyrre Ås, 2006:25, ISBN 82-471-7791-9 (printed version), ISBN 82-471-7791-9 (electronic version), ISSN 1503-8181.

”Constitutive models of elastoplasticity and fracture for aluminium alloys under strain path change”,
Dasharatha Achani, 2006:76, ISBN 82-471-7903-2 (printed version), ISBN 82-471-7902-4 (electronic version), ISSN 1503-8181.

“Simulations of 2D dynamic brittle fracture by the Element-free Galerkin method and linear fracture mechanics”,
Tommy Karlsson, 2006:125, ISBN 82-471-8011-1 (printed version), ISBN 82-471-8010-3 (electronic version), ISSN 1503-8181.

“Penetration and Perforation of Granite Targets by Hard Projectiles”,
Chong Chiang Seah, 2006:188, ISBN 82-471-8150-9 (printed version), ISBN 82-471-8149-5 (electronic version), ISSN 1503-8181.

“Deformations, strain capacity and cracking of concrete in plastic and early hardening phases”,
Tor Arne Hammer, 2007:234, ISBN 978-82-471-5191-4 (printed version), ISBN 978-82-471-5207-2 (electronic version), ISSN 1503-8181.

“Crashworthiness of dual-phase high-strength steel: Material and Component behaviour”, Venkatapathi Tarigopula, 2007:230, ISBN 82-471-5076-4 (printed version), ISBN 82-471-5093-1 (electronic version), ISSN 1503-8181.

“Fibre reinforcement in load carrying concrete structures”,
Åse Lyslo Døssland, 2008:50, ISBN 978-82-471-6910-0 (printed version), ISBN 978-82-471-6924-7 (electronic version), ISSN 1503-8181.

“Low-velocity penetration of aluminium plates”,
Frode Grytten, 2008:46, ISBN 978-82-471-6826-4 (printed version), ISBN 978-82-471-6843-1 (electronic version), ISSN 1503-8181.

“Robustness studies of structures subjected to large deformations”,
Ørjan Fyllingen, 2008:24, ISBN 978-82-471-6339-9 (printed version), ISBN 978-82-471-6342-9 (electronic version), ISSN 1503-8181.

“Constitutive modelling of morsellised bone”,
Knut Birger Lunde, 2008:92, ISBN 978-82-471-7829-4 (printed version), ISBN 978-82-471-7832-4 (electronic version), ISSN 1503-8181.

“Experimental Investigations of Wind Loading on a Suspension Bridge Girder”,
Bjørn Isaksen, 2008:131, ISBN 978-82-471-8656-5 (printed version), ISBN 978-82-471-8673-2 (electronic version), ISSN 1503-8181.

“Cracking Risk of Concrete Structures in The Hardening Phase”,
Guomin Ji, 2008:198, ISBN 978-82-471-1079-9 (printed version), ISBN 978-82-471-1080-5 (electronic version), ISSN 1503-8181.

“Modelling and numerical analysis of the porcine and human mitral apparatus”,
Victorien Emile Prot, 2008:249, ISBN 978-82-471-1192-5 (printed version), ISBN 978-82-471-1193-2 (electronic version), ISSN 1503-8181.

“Strength analysis of net structures”,
Heidi Moe, 2009:48, ISBN 978-82-471-1468-1 (printed version), ISBN 978-82-471-1469-8 (electronic version), ISSN1503-8181.

“Numerical analysis of ductile fracture in surface cracked shells”,
Espen Berg, 2009:80, ISBN 978-82-471-1537-4 (printed version), ISBN 978-82-471-1538-1 (electronic version), ISSN 1503-8181.

“Subject specific finite element analysis of bone – for evaluation of the healing of a leg lengthening and evaluation of femoral stem design”,
Sune Hansborg Pettersen, 2009:99, ISBN 978-82-471-1579-4 (printed version), ISBN 978-82-471-1580-0 (electronic version), ISSN 1503-8181.

“Evaluation of fracture parameters for notched multi-layered structures”,
Lingyun Shang, 2009:137, ISBN 978-82-471-1662-3 (printed version), ISBN 978-82-471-1663-0 (electronic version), ISSN 1503-8181.

“Modelling of Dynamic Material Behaviour and Fracture of Aluminium Alloys for Structural Applications”
Yan Chen, 2009:69, ISBN 978-82-471-1515-2 (printed version), ISBN 978-82 471-1516-9 (electronic version), ISSN 1503-8181.

“Nanomechanics of polymer and composite particles”
Jianying He 2009:213, ISBN 978-82-471-1828-3 (printed version), ISBN 978-82-471-1829-0 (electronic version), ISSN 1503-8181.

“Mechanical properties of clear wood from Norway spruce”
Kristian Berbom Dahl 2009:250, ISBN 978-82-471-1911-2 (printed version) ISBN 978-82-471-1912-9 (electronic version), ISSN 1503-8181.

“Modeling of the degradation of TiB_2 mechanical properties by residual stresses and liquid Al penetration along grain boundaries”
Micol Pezzotta 2009:254, ISBN 978-82-471-1923-5 (printed version) ISBN 978-82-471-1924-2 (electronic version) ISSN 1503-8181.

“Effect of welding residual stress on fracture”
Xiabo Ren 2010:77, ISBN 978-82-471-2115-3 (printed version) ISBN 978-82-471-2116-0 (electronic version), ISSN 1503-8181.

“Pan-based carbon fiber as anode material in cathodic protection system for concrete structures”
Mahdi Chini 2010:122, ISBN 978-82-471-2210-5 (printed version) ISBN 978-82-471-2213-6 (electronic version), ISSN 1503-8181.

“Structural Behaviour of deteriorated and retrofitted concrete structures”
Irina Vasililjeva Sæther 2010:171, ISBN 978-82-471-2315-7 (printed version) ISBN 978-82-471-2316-4 (electronic version) ISSN 1503-8181.

“Prediction of local snow loads on roofs”
Vivian Meløysund 2010:247, ISBN 978-82-471-2490-1 (printed version) ISBN 978-82-471-2491-8 (electronic version) ISSN 1503-8181.

“Behaviour and modelling of polymers for crash applications”
Virgile Delhaye 2010:251, ISBN 978-82-471-2501-4 (printed version) ISBN 978-82-471-2502-1 (electronic version) ISSN 1503-8181.

“Blended cement with reducted CO_2 emission – Utilizing the Fly Ash-Limestone Synergy”,
Klaartje De Weerdt 2011:32, ISBN 978-82-471-2584-7 (printed version) ISBN 978-82-471-2584-4 (electronic version) ISSN 1503-8181.

“Chloride induced reinforcement corrosion in concrete” Concept of critical chloride content – methods and mechanisms.
Ueli Angst 2011:113, ISBN 978-82-471-2769-9 (printed version) ISBN 978-82-471-2763-6 (electronic version) ISSN 1503-8181.

“A thermo-electric-Mechanical study of the carbon anode and contact interface for Energy savings in the production of aluminium”.
Dag Herman Andersen 2011:157, ISBN 978-82-471-2859-6 (printed version) ISBN 978-82-471-2860-2 (electronic version) ISSN 1503-8181.

“Structural Capacity of Anchorage Ties in Masonry Veneer Walls Subjected to Earthquake”. The implications of Eurocode 8 and Eurocode 6 on a typical Norwegain veneer wall.
Ahmed Mohamed Yousry Hamed 2011:181, ISBN 978-82-471-2911-1 (printed version) ISBN 978-82-471-2912-8 (electronic ver.) ISSN 1503-8181.

“Work-hardening behaviour in age-hardenable Al-Zn-Mg(-Cu) alloys”.
Ida Westermann , 2011:247, ISBN 978-82-471-3056-8 (printed ver.) ISBN 978-82-471-3057-5 (electronic ver.) ISSN 1503-8181.

“Behaviour and modelling of selfpiercing riveted connections using aluminium rivets”.
Nguyen-Hieu Hoang, 2011:266, ISBN 978-82-471-3097-1 (printed ver.) ISBN 978-82-471-3099-5 (electronic ver.) ISSN 1503-8181.

“Fibre reinforced concrete”.
Sindre Sandbakk, 2011:297, ISBN 978-82-471-3167-1 (printed ver.) ISBN 978-82-471-3168-8 (electronic ver) ISSN 1503:8181.

“Dynamic behaviour of cablesupported bridges subjected to strong natural wind”.
Ole Andre Øiseth, 2011:315, ISBN 978-82-471-3209-8 (printed ver.) ISBN 978-82-471-3210-4 (electronic ver.) ISSN 1503-8181.

“Constitutive modeling of solargrade silicon materials”
Julien Cochard, 2011:307, ISBN 978-82-471-3189-3 (printed ver). ISBN 978-82-471-3190-9 (electronic ver.) ISSN 1503-8181.

“Constitutive behavior and fracture of shape memory alloys”
Jim Stian Olsen, 2012:57, ISBN 978-82-471-3382-8 (printed ver.) ISBN 978-82-471-3383-5 (electronic ver.) ISSN 1503-8181.

“Field measurements in mechanical testing using close-range photogrammetry and digital image analysis”
Egil Fagerholt, 2012:95, ISBN 978-82-471-3466-5 (printed ver.) ISBN 978-82-471-3467-2 (electronic ver.) ISSN 1503-8181.

“Towards a better under standing of the ultimate behaviour of lightweight aggregate concrete in compression and bending”,
Håvard Nedrelid, 2012:123, ISBN 978-82-471-3527-3 (printed ver.) ISBN 978-82-471-3528-0 (electronic ver.) ISSN 1503-8181.

“Numerical simulations of blood flow in the left side of the heart”
Sigrid Kaarstad Dahl, 2012:135, ISBN 978-82-471-3553-2 (printed ver.) ISBN 978-82-471-3555-6 (electronic ver.) ISSN 1503-8181.

“Moisture induced stresses in glulam”
Vanessa Angst-Nicollier, 2012:139, ISBN 978-82-471-3562-4 (printed ver.) ISBN 978-82-471-3563-1 (electronic ver.) ISSN 1503-8181.

“Biomechanical aspects of distraction osteogensis”
Valentina La Russa, 2012:250, ISBN 978-82-471-3807-6 (printed ver.) ISBN 978-82-471-3808-3 (electronic ver.) ISSN 1503-8181.

“Ductile fracture in dual-phase steel. Theoretical, experimental and numerical study”
Gaute Gruben, 2012:257, ISBN 978-82-471-3822-9 (printed ver.) ISBN 978-82-471-3823-6 (electronic ver.) ISSN 1503-8181.

“Damping in Timber Structures”
Nathalie Labonnote, 2012:263, ISBN 978-82-471-3836-6 (printed ver.) ISBN 978-82-471-3837-3 (electronic ver.) ISSN 1503-8181.

“Biomechanical modeling of fetal veins: The umbilical vein and ductus venosus bifurcation”
Paul Roger Leinan, 2012:299, ISBN 978-82-471-3915-8 (printed ver.) ISBN 978-82-471-3916-5 (electronic ver.) ISSN 1503-8181.

“Large-Deformation behaviour of thermoplastics at various stress states”
Anne Serine Ognedal, 2012:298, ISBN 978-82-471-3913-4 (printed ver.) ISBN 978-82-471-3914-1 (electronic ver.) ISSN 1503-8181.

“Hardening accelerator for fly ash blended cement”
Kien Dinh Hoang, 2012:366, ISBN 978-82-471-4063-5 (printed ver.) ISBN 978-82-471-4064-2 (electronic ver.) ISSN 1503-8181.

“From molecular structure to mechanical properties”
Jianyang Wu, 2013:186, ISBN 978-82-471-4485-5 (printed ver.) ISBN 978-82-471-4486-2 (electronic ver.) ISSN 1503-8181.

"Experimental and numerical study of hybrid concrete structures"
Linn Grepstad Nes, 2013:259, ISBN 978-82-471-4644-6 (printed ver.) ISBN 978-82-471-4645-3 (electronic ver.) ISSN 1503-8181.

"Mechanics of ultra-thin multi crystalline silicon wafers"
Saber Saffar, 2013:199, ISBN 978-82-471-4511-1 (printed ver.) ISBN 978-82-471-4513-5 (electronic ver). ISSN 1503-8181.

"Through process modelling of welded aluminium structures"
Anizahyati Alisibramulisi, 2013:325, ISBN 978-82-471-4788-7 (printed ver.) ISBN 978-82-471-4789-4 (electronic ver.) ISSN 1503-8181.

"Combined blast and fragment loading on steel plates"
Knut Gaarder Rakvåg, 2013:361, ISBN978-82-471-4872-3 (printed ver.) ISBN 978-82-4873-0 (electronic ver.). ISSN 1503-8181.

"Characterization and modelling of the anisotropic behaviour of high-strength aluminium alloy"
Marion Fourmeau, 2014:37, ISBN 978-82-326-0008-3 (printed ver.) ISBN 978-82-326-0009-0 (electronic ver.) ISSN 1503-8181.

"Behaviour of threated steel fasteners at elevated deformation rates"
Henning Fransplass, 2014:65, ISBN 978-82-326-0054-0 (printed ver.) ISBN 978-82-326-0055-7 (electronic ver.) ISSN 1503-8181.

"Sedimentation and Bleeding"
Ya Peng, 2014:89, ISBN 978-82-326-0102-8 (printed ver.) ISBN 978-82-326-0103-5 (electric ver.) ISSN 1503-8181.

"Impact against X65 offshore pipelines"
Martin Kristoffersen, 2014:362, ISBN 978-82-326-0636-8 (printed ver.) ISBN 978-82-326-0637-5 (electronic ver.) ISSN 1503-8181.

"Formability of aluminium alloy subjected to prestrain by rolling"
Dmitry Vysochinskiy, 2014:363,, ISBN 978-82-326-0638-2 (printed ver.) ISBN 978-82-326-0639-9 (electronic ver.) ISSN 1503-8181.

"Experimental and numerical study of Yielding, Work-Hardening and anisotropy in textured AA6xxx alloys using crystal plasticity models"
Mikhail Khadyko, 2015:28, ISBN 978-82-326-0724-2 (printed ver.) ISBN 978-82-326-0725-9 (electronic ver.) ISSN 1503-8181.

"Behaviour and Modelling of AA6xxx Aluminium Alloys Under a Wide Range of Temperatures and Strain Rates"
Vincent Vilamosa, 2015:63, ISBN 978-82-326-0786-0 (printed ver.) ISBN 978-82-326-0787-7 (electronic ver.) ISSN 1503-8181.

“A Probabilistic Approach in Failure Modelling of Aluminium High Pressure Die-Castings”
Octavian Knoll, 2015:137, ISBN 978-82-326-0930-7 (printed ver.) ISBN 978-82-326-0931-4 (electronic ver.) ISSN 1503-8181.

“Ice Abrasion on Marine Concrete Structures”
Egil Møen, 2015:189, ISBN 978-82-326-1034-1 (printed ver.) ISBN 978-82-326-1035-8 (electronic ver.) ISSN 1503-8181.

“Fibre Orientation in Steel-Fibre-Reinforced Concrete”
Giedrius Zirgulis, 2015:229, ISBN 978-82-326-1114-0 (printed ver.) ISBN 978-82-326-1115-7 (electronic ver.) ISSN 1503-8181.

“Effect of spatial variation and possible interference of localised corrosion on the residual capacity of a reinforced concrete beam”
Mohammad Mahdi Kioumarsi, 2015:282, ISBN 978-82-326-1220-8 (printed ver.) ISBN 978-82-1221-5 (electronic ver.) ISSN 1503-8181.

“The role of concrete resistivity in chloride-induced macro-cell corrosion”
Karla Horbostel, 2015:324, ISBN 978-82-326-1304-5 (printed ver.) ISBN 978-82-326-1305-2 (electonic ver.) ISSN 1503-8181.

“Flowable fibre-reinforced concrete for structural applications”
Elena Vidal Sarmiento, 2015-335, ISBN 978-82-326-1324-3 (printed ver.) ISBN 978-82-326-1325-0 (electronic ver.) ISSN 1503-8181.

“Development of chushed sand for concrete production with microproportioning”
Rolands Cepuritis, 2016:19, ISBN 978-82-326-1382-3 (printed ver.) ISBN 978-82-326-1383-0 (electronic ver.) ISSN 1503-8181.

“Withdrawal properties of threaded rods embedded in glued-laminated timer elements”
Haris Stamatopoulos, 2016:48, ISBN 978-82-326-1436-3 (printed ver.) ISBN 978-82-326-1437-0 (electronic ver.) ISSN 1503-8181.

“An Experimental and numerical study of thermoplastics at large deformation”
Marius Andersen, 2016:191, ISBN 978-82-326-1720-3 (printed ver.) ISBN 978-82-326-1721-0 (electronic ver.) ISSN 1503-8181.

“Modeling and Simulation of Ballistic Impact”
Jens Kristian Holmen, 2016:240, ISBN 978-82-326-1818-7 (printed ver). ISBN 978-82-326-1819-4 (electronic ver.) ISSN 1503-8181.

“Early age crack assessment of concrete structures”
Anja B. Estensen Klausen, 2016:256, ISBN 978-82-326-1850-7 (printed ver). ISBN 978-82-326-1851-4 (electronic ver.) ISSN 1503-8181.

"Uncertainty quantification and sensitivity analysis for cardiovascular models"
Vinzenz Gregor Eck, 2016:234, ISBN 978-82-326-1806-4 (printed ver.) ISBN 978-82-326-1807-1 (electronic ver.) ISSN 1503-8181.

"Dynamic behaviour of existing and new railway catenary systems under Norwegain conditions"
Petter Røe Nåvik, 2016:298, ISBN 978-82-326-1935-1 (printed ver.) ISBN 978-82-326-1934-4 (electronic ver.) ISSN 1503-8181.

"Mechanical behaviour of particle-filled elastomers at various temperatures"
Arne Ilseng, 2016-295, ISBN978-82-326-1928-3 (printed ver.) ISBN 978-82-326-1929-0 (electronic ver.) ISSN 1503-8181.

"Nanotechnology for Anti-Icing Application"
Zhiwei He, 2016:348, ISBN 978-82-326-2038-8 (printed ver.) ISBN 978-82-326-2019-5 (electronic ver.) ISSN 1503-8181.

"Conduction Mechanisms in Conductive Adhesives with Metal-Coated Polyer Spheres"
Sigurd Rolland Pettersen, 2016:349, ISBN 978-326-2040-1 (printed ver,) ISBN 978-82-326-2041-8 (electronic ver.) ISSN 1503-8181.

"The interaction between calcium lignosulfonate and cement"
Alessia Colombo, 2017:20, ISBN 978-82-326-2122-4 (printed ver.) ISBN 978-82-326-2123-1 (electronic ver.) ISSN 1503-8181.

"Behaviour and Modelling of Flexible Structures Subjected to Blast Loading"
Vegard Aune, 2017:101, ISBN 978-82-326-2274-0 (printed ver.) ISBN 978-82-326-2275-7 (electronic ver.) ISSN 1503-8181.

"Behaviour of steel connections under quasi-static and impact loading"
Erik Løhre Grimsmo, 2017:159, ISBN 978-82-326-2390-7 (printed ver.) ISBN 978-82-326-2391-4 (electronic ver.) ISSN 1503-8181.

"An experimental and numerical study of cortical bone at he macro and Nano-scale"
Masoud Ramenzanzadehkoldeh,, 2017:208, ISBN 978-82-326-2488-1 (printed ver.) ISBN 978-82-326-2489-8 (electronic ver.) ISSN 1503-8181.

"Optoelectrical Properties of a Novel Organic Semiconductor: 6,13-Dichloropentacene"
Mao Wang, 2017:130, ISBN 978-82-326-2332-7 (printed ver.) ISBN 978-82-326-2333-4) (electronic ver.) ISSN 1503-8181.

"Core-shell structured microgels and their behavior at oil and water interface"
Yi Gong, 2017:182, ISBN 978-82-326-2436-2 (printed. ver.) ISBN 978-82-326-2437-9 (electronic ver.) ISSN 1503-8181.

“Aspects of design of reinforced concrete structures using nonliear finite element analyses”
Morten Engen, 2017:149, ISBN 978-82-326-2370-9 (printed ver.) ISBN 978-82-326-2371-6 (electronic ver.) ISSN 1503-8181.

“Numerical studies on ductile failure of aluminium alloys”
Lars Edvard Dæhli, 2017:284, ISBN 978-82-326-2636-6 (printed ver.) ISBN 978-82-326-2637-3 (electronic ver.) ISSN 1503-8181.

“Modelling and Assessment of Hydrogen Embrittlement in Steels and Nickel Alloys”
Haiyang Yu, 2017:278, ISBN 978-82-326-2624-3 (printed. ver.) ISBN 978-82-326-2625-0 (electronic ver.) ISSN 1503-8181.

“Network arch timber bridges with light timber deck on transverse crossbeams”
Anna Weronika Ostrycharczyk, 2017:318, ISBN 978-82-326-2704-2 (printed ver.) ISBN 978-82-326-2705-9 (electronic ver.) ISSN 1503-8181.

“Splicing of Large Glued Laminated Timber Elements by Use of Long Threated Rods”
Martin Cepelka, 2017:320, ISBN 978-82-326-2708-0 (printed ver.) ISBN 978-82-326-2709-7 (electronic ver.) ISSN 1503-8181.

“Thermomechanical behaviour of semi-crystalline polymers: experiments, modelling and simulation”
Joakim Johnsen, 2017-317, ISBN 978-82-326-2702-8 (printed ver.) ISBN 978-82-326-2703-5 (electronic ver.) ISSN 1503-8181.

“Small-Scale Plasiticity under Hydrogen Environment”
Kai Zhao, 2017:356, ISBN 978-82-326-2782-0 (printed ver.) ISBN 978-82-326-2783-7 (electronic er.) ISSN 1503-8181.

“Risk and Reliability Based Calibration of Structural Design Codes”
Michele Baravalle, 2017:342, ISBN 978-82-326-2752-3 (printed ver,) ISBN 978-82-326-2753-0 (electronic ver.) ISSN 1503-8181.

“Dynamic behaviour of floating bridges exposed to wave excitation”
Knut Andreas Kvåle, 2017:365, ISBN 978-82-326-2800-1 (printed ver.) ISBN 978-82-326-2801-8 (electronic ver.) ISSN 1503-8181.

“Dolomite calcined clay composite cement – hydration and durability”
Alisa Lydia Machner, 2018:39, ISBN 978-82-326-2872-8 (printed ver.). ISBN 978-82-326-2873-5 (electronic ver.) ISSN 1503-8181.

“Modelling of the self-excited forces for bridge decks subjected to random motions: an experimental study”
Bartosz Siedziako, 2018:52, ISBN 978-82-326-2896-4 (printed ver.). ISBN 978-82-326-2897-1 (electronic ver.) ISSN 1503-8181.

“A probabilistic-based methodology for evaluation of timber facade constructions”
Klodian Gradeci, 2018:69, ISBN 978-82-326-2928-2 (printed ver.) ISBN 978-82-326-2929-9 (electronic ver.) ISSN 1503-8181.

“Behaviour and modelling of flow-drill screw connections”
Johan Kolstø Sønstabø, 2018:73, ISBN 978-82-326-2936-7 (printed ver.) ISBN 978-82-326-2937-4 (electronic ver.) ISSN 1503-8181.

“Full-scale investigation of the effects of wind turbulence characteristics on dynamic behavior of long-span cable-supported bridges in complex terrain”
Aksel Fenerci, 2018 100, ISBN 9978-82-326-2990-9 (printed ver.) ISBN 978-82-326-2991-6 (electronic ver.) ISSN 1503-8181.

“Modeling and simulation of the soft palate for improved understanding of the obstructive sleep apnea syndrome”
Hongliang Liu, , 2018:101, ISBN 978-82-326-2992-3 (printed ver.) ISBN 978-82-326-2993-0 (electronic ver.) ISSN 1503-8181.

“Long-term extreme response analysis of cable-supported bridges with floating pylons subjected to wind and wave loads”.
Yuwang Xu, 2018:229, ISBN 978-82-326-3248-0 (printed ver.) ISBN 978-82-326-3249-7 (electronic ver.) ISSN 1503-8181.